Non-Equilibrium Phenomena in Correlated Electron Systems and Photon Bose-Einstein Condensates

Dissertation
zur
Erlangung des Doktorgrades (Dr. rer. nat.)
der
Mathematisch-Naturwissenschaftlichen Fakultät
der
Rheinischen Friedrich-Wilhelms-Universität Bonn

vorgelegt von

Michael Turaev

Bonn 2025

Angefertigt mit Genehmigung der Mathematisch-Naturwissenschaftlichen Fakultät der Rheinischen Friedrich-Wilhelms-Universität Bonn

Gutachter/Betreuer: Prof. Dr. Johann Kroha
Gutachterin: Prof. Dr. Corinna Kollath

Tag der Promotion: 16.07.2025
Erscheinungsjahr: 2026

Abstract

This thesis explores non-equilibrium phenomena in quantum many-body systems, with a focus on correlated electron systems and photon Bose-Einstein condensates. The first part develops the theoretical foundation, beginning with the Lindblad master equation and the construction of non-equilibrium quantum field theory. The two-particle irreducible effective action formalism is introduced, from which the Kadanoff-Baym equations for real-time evolution and the Dyson equation for steady-states are derived. The theoretical groundwork continues with a treatment of strongly correlated electron systems, where non-equilibrium dynamical mean-field theory (DMFT), auxiliary particles, and the non-crossing approximation (NCA) are introduced. These techniques, together with the Lindblad and Kadanoff-Baym approaches, are used throughout the subsequent chapters.

The second part presents the main research projects of this thesis. The first two projects are concerned with the fate of the heavy fermion state under irradiation of light. To accurately incorporate light-matter interactions in this case, dipole transitions must be included. In the first project a periodically driven system is considered, where the light can be treated semiclassically. A Floquet DMFT+NCA framework is developed, revealing the mechanisms and conditions under which the heavy fermion state is most strongly suppressed. The second project analyzes a THz spectroscopy experiment performed on $CeCu_6$. In this case a semi-classical treatment of the light field is no longer sufficient, and a full two-time evolution of all the non-equilibrium Green functions is necessary. This approach reveals the microscopic mechanisms underlying the collapse and revival of the Kondo state observed in the experiment. The next project investigates a recent experiment regarding an observation of a non-Hermitian phase transition in EuO. The equilibrium properties of EuO are first analyzed, and then an exciton model is constructed that gives rise to the non-Hermitian phase transition, in good agreement with experimental observations. In the final project, a photon Bose-Einstein condensate in a dye-filled microcavity is studied. A stabilization mechanism, distinct from thermalization, is revealed which admits a condensate phase for orders of magnitude longer than the experimentally relevant timescales.

Publications

- [9] J. Li, M. Turaev, M. Matsubara, K. Kliemt, C. Krellner, S. Pal, M. Fiebig, and J. Kroha, “Discovery of a non-Hermitian phase transition in a bulk condensed-matter system”, `https://arxiv.org/abs/2412.16012`, (2024).
- [10] A. Abouelela*, M. Turaev*, R. Kramer, M. Janning, M. Kajan, S. Ray, and J. Kroha, “Stabilizing Open Photon Condensates by Ghost-Attractor Dynamics”, Phys. Rev. Lett. **135**, 053402 (2025). `https://doi.org/10.1103/hcsq-dwcg`. * These authors contributed equally to this work
- [103] F. Meirinhos, M. Turaev, M. Kajan, T. Bode, and J. Kroha, “Heavy-fermion collapse and delayed revival by pulsed light”, `https://arxiv.org/abs/2509.07117` (2025).
- M. Turaev, J. Kroha “Periodically Driven Heavy-Fermion systems”, in preparation.

Non-thesis related research:

- F. Neumann, M. Turaev, J. Kroha “Influence of Magnetic and Non-Magnetic Impurities on the surface of Topological Kondo Insulators”, in preparation.
- M. Lenk, Q. Li, M. Turaev, J, Kroha, “Orbitally-resolved lattice-coherence in heavy fermion systems”, in preparation.
- J. Schwingel, M. Turaev, J. Kroha, and S. Ray, “Expansion dynamics of strongly correlated lattice bosons: A self-consistent density-matrix approach”, Phys. Rev. A **112**, 043322 (2025). `https://doi.org/10.1103/bzvn-sp2h`.

Acknowledgments

The last few years here at the University of Bonn have been nothing short of incredible. Not only was I fortunate enough to work with people who are genuinely excited about physics and are always happy to discuss it, but I was also lucky to meet incredible people who have become lifelong friends, and much more. So, I would like to use this space to thank everyone who was part of this journey.

First and foremost, I would like to thank Hans, who was always there for me and always offered great advice, both academically and personally. I especially appreciate that you listened to all of my ideas throughout the years and somehow managed to find the few that made sense. I'm grateful for the opportunity to work on such a wide variety of topics, each filled with rich and fascinating physics. Your intuition and enthusiasm are inspiring, and I learned a massive amount from you.

Thank you to Francisco, for being a great office mate and someone I could always rely on. You showed me the importance of physical rigor, how to code properly, and that shortcuts never truly work. I would also like to thank Micha, for coming up with seemingly simple and innocent questions that turned out to be anything but that. These often led to days, weeks, and sometimes even months of the most fun discussions during my PhD.

I'm very grateful to Marvin for being able to intuitively clear up any clouds of doubt I had, making every topic so much brighter. And to Ulli, who was not only a great travel and tutoring mate, but also one of the most down to earth persons I have met.

A big thank you to Sayak, although our conversations got heated sometimes, you were always someone I could talk to about anything. I learned a lot from you, and thoroughly enjoyed all the fascinating dynamics that we explored together. I would also like to extend the thanks to the rest of the bosons crew, Aya and Roman, for always explaining things with all the details whenever I was lacking the background.

Many thanks to Fabiola, Moritz and Julian, for always listening and challenging everything I had to say. I thoroughly enjoyed working with all of you on your Master's projects. And to Li, thank you for always keeping a joyful atmosphere in the office. Your stories never failed to brighten up the mood.

I would like to thank all the other members of the group during my time here Haixin, Tim, Mohammed, Marcel, Johnathan, Lukas, Christopher, and Tommy. It was always a pleasure working and chatting with you.

A special thanks goes out to the experimentalists in Zurich, Manfred and Jingwen, who always listened to my ideas and took them seriously. Working with you was incredibly enjoyable, and I hope we get the chance to collaborate again in the future.

Last, but by no means the least, I would like to thank Carlotta, for all the love, patience and for making all aspects of my life better. If I had to fully write out everything that I'm thankful to you for, it would be much longer than a thesis. I would also like to thank my parents and my family for their constant support. And, of course, Ori, who was a great writing companion during the final stretch.

Contents

Introduction

Non-equilibrium is the natural state of all systems and arises across all areas of science. In physics, nearly ever experiment involves some degree of non-equilibrium behavior, whether through the application of an electric field to measure a current response or by heating a sample to probe its thermal properties. Despite this, great effort is put in to isolate systems as much as possible and minimize the influence of measurement techniques in order to extract equilibrium properties. Nevertheless, in technological applications, materials are rarely used for their static properties. Instead, their non-equilibrium behavior is often essential to their functionality, for example in engines, lasers, LEDs, superconductors, and others.

In recent years, non-equilibrium physics has emerged as a promising avenue for uncovering new physical phenomena. It has led to the discovery of exotic states of matter such as time crystals [1], prethermal phases [2], non-equilibrium superconductivity [3], and many others [4], several of which have no equilibrium analogue [5]. An illustration is provided in Figure 1, which shows various processes according to their “distance” from equilibrium and indicates the characteristic timescale associated with the corresponding effect. Notable examples highlighted include Floquet states, electronic relaxation dynamics, dynamical phase transitions, and the Franck-Condon mechanism, all of which will be addressed in this thesis.

An important experimental technique that motivates several of the theoretical analysis presented in this work is THz spectroscopy. This method enables the investigation of energy scales in the meV range, corresponding to dynamics on the order of picoseconds. It is particularly suitable for probing low energy excitations, which are characteristic of strongly correlated electron systems. An example of strongly correlated electron systems studied throughout this thesis are heavy fermion materials.

The mechanism behind the formation of heavy fermion systems is the Kondo effect, which was first identified in a different setting in the 1930s [6]. It was observed that a small concentration of transition metal impurities embedded in a metallic host leads to an increase in the resistivity at low temperatures. It took many years to understand this phenomenon and connect it to a many body effect involving the screening of localized magnetic moments by conduction electrons. The Kondo effect has since become a foundational example in the study of strongly correlated electron systems.

As one moves down the periodic table from transition metals to the lanthanide series, the partially filled $4f$-shells of rare earth elements provide a natural platform for the formation of localized magnetic moments. These local moments are typically situated on every lattice site, leading to a lattice of Kondo screening processes throughout the material. The resulting resonances hybridize with the conduction band, forming a narrow and heavy band near the Fermi level, leading to what is commonly referred to as a heavy Fermi liquid. The strong correlations inherent in these materials make them highly tunable by external parameters such as pressure, magnetic field, or doping. This tunability leads to rich and complex phase diagrams, where phases such as unconventional superconductivity, antiferromagnetism, charge density waves, and heavy Fermi liquids can all emerge, sometimes even coexisting within a

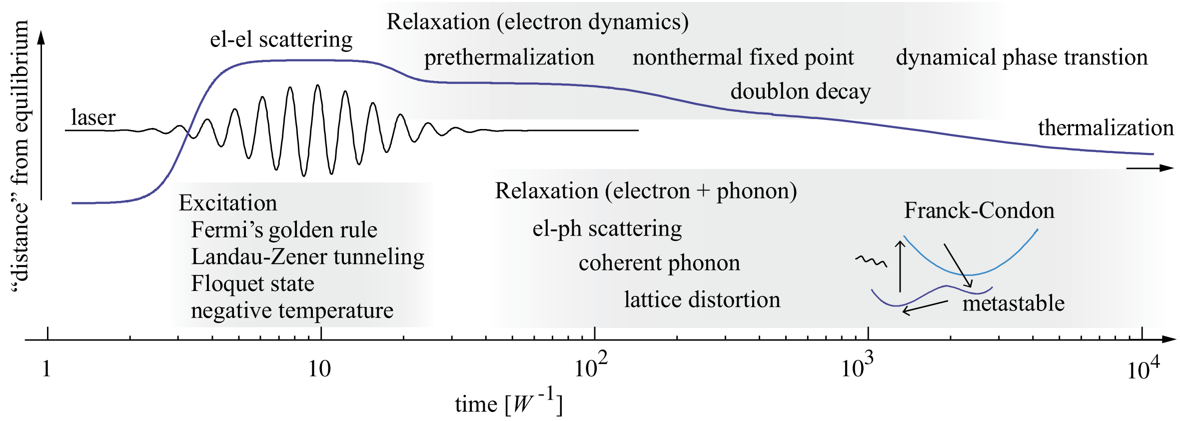

Figure 1: Schematic illustration of non-equilibrium processes following excitation from an external laser, organized by their “distance” from equilibrium and their characteristic timescales, taken from [8]. The diagram highlights various physical mechanism, among which Floquet states, electronic relaxation dynamics, dynamical phase transitions, and the Franck-Condon mechanism will be addressed in this thesis.

single compound [7].

Non-equilibrium conditions can even give rise to new types of phase transitions, known as non-Hermitian phase transitions. These transitions are not associated with a symmetry breaking in the thermodynamic sense but instead reflect a qualitative change in the dynamical properties of the system, mostly constituting to a transition from bi-exponential decay to damped oscillatory behavior. This emerges when the response matrix of the system changes from having two real eigenvalues to a pair of complex conjugate eigenvalues, which happens upon the crossing of an exceptional point. At the exceptional, the matrix becomes non-diagonalizable, and the eigenvectors associated with the dynamical modes of the system coalesce, meaning that the two modes effectively merge into one. Although non-Hermitian phase transitions have previously been explored in atomic gases and engineered devices, their realization in bulk materials remains largely unexplored due to the strong non-equilibrium conditions required. Using THz spectroscopy, the first experimental observation of such a transition in a condensed matter system was reported in EuO [9]. This thesis explores the microscopic mechanism underlying for this observation.

The final system studied in this thesis is a realization of a photon Bose-Einstein condensate in a driven, dissipative optical microcavity filled with a dye solution. Since photons are gauge bosons of the electromagnetic force, they do not have a fixed particle number, and thus cannot undergo the standard condensation mechanism. The inherently non-equilibrium setting of the experiment allows for a chemical potential as well as a fixed photon number on average to be achieved. This interplay of drive and loss results in a steady state that closely mimics equilibrium condensation in the photon number and molecule excitation. However, a study which incorporates fluctuations as well as condensate on equal footing is lacking. It is revealed that this system undergoes a stabilization mechanism known from nonlinear dynamics, via an unphysical fixed point that lies beyond the physical boundary [10]. Nonetheless this unphysical fixed point attracts the trajectories in phase space leading to a long lived metastable state with a fixed condensate number and thermal distribution for the photon number and molecule excitations in good agreement with the experimental observations.

In the following, an overview over the structure of this thesis and the contents of the chapters will be outlined. In Chapter 1 the theoretical foundation for non-equilibrium dynamics will be provided. It begins with an introduction to the Lindblad master equation and the cumulant expansion approach, providing a systematic framework for describing open quantum systems coupled to baths. This is followed by a construction of non-equilibrium quantum field theory on the Keldysh contour, including conserving approximations and the two-particle irreducible effective action. This chapter is intended as a concise introduction, and the reader is referred to the following books for further details [11–13].

In Chapter 2 the background on strongly correlated electron systems will be introduced, with a particular focus on Kondo physics and heavy fermion systems. These topics are well-established by now and are also heavily discussed in [14]. Key theoretical tools such as dynamical mean-field theory (DMFT) and the non-crossing approximation (NCA) are introduced. While primarily serving as an introductory chapter, it also includes some developments, such as entanglement entropy calculations as well as a new DMFT formulations.

In Chapter 3 periodically driven heavy fermion systems will be explored. It begins with an introduction to the Floquet theorem and its application to driven two-level systems. The formalism of Floquet Green functions is then developed within the Floquet-Keldysh field theory framework. This is applied both to the driven single-impurity Anderson model and also extended to the Anderson lattice model, revealing insights into the fate of the heavy fermion state under periodic driving.

In Chapter 4 the theoretical analysis of a THz spectroscopy experiment on $\mathrm{CeCu_6}$ will be presented, where the light field must be treated within the full framework of quantum field theory. A real two-time DMFT + NCA solver is introduced and how it is used to resolve both low energy many-body features and short-time dynamics. Therefore, an experimental comparison was able to be established and the many-body origin of the experimentally observed optical response was confirmed.

In Chapter 5 the study of the non-Hermitian phase transition observed in the ferromagnetic semiconductor EuO will be discussed. The chapter begins by analyzing the equilibrium properties of EuO, followed by a discussion of previous experimental results showing enhancement of the Curie temperature via photo-doping. The focus then turns to the theoretical description of the non-Hermitian phase transition, including its microscopic origin and connection the experimental observations.

In Chapter 6 the photon Bose-Einstein condensate realized in a driven-dissipative microcavity will be investigated. Emphasis will be placed on the role of explicit symmetry breaking terms in the formation and stabilization of the condensate. Their influence on a non-Hermitian phase transition observed in the system will be discussed. A new stabilization mechanism for the condensate in this system will be introduced and analyzed in detail.

Chapter 1

Non-Equilibrium Dynamics

To gain a deep understanding of non-equilibrium systems, it is essential to first define their counterpart, as non-equilibrium properties arise from the exclusion of this special case. Equilibrium systems are described by the Gibbs ensemble, which uniquely characterizes states using well-defined thermodynamic quantities such as temperature and chemical potential. These quantities are incorporated into the partition function as

$$Z = \sum_i e^{-\beta(E_i - \mu N_i)}, \tag{1.1}$$

where β is the inverse temperature, μ is the chemical potential, E_i denotes the energy of state i, and N_i is the corresponding particle number. When equilibrium dynamics are considered, the eigenstate of the initial state at time $t \to -\infty$ remains an eigenstate at time $t \to \infty$, differing only by a phase factor. This reflects the fact that equilibrium systems preserve their thermodynamic properties, throughout the time evolution.

Non-equilibrium systems, by contrast, encompass all scenarios where the Gibbs ensemble description is no longer valid, meaning that temperature and chemical potential are not well-defined quantities anymore. Such systems typically arise in the context of open systems where phenomena such as dissipation, or external driving forces are present. As a result, the time evolution becomes significantly more complicated, often giving rise to non-equilibrium steady states and dynamics that are fundamentally different from equilibrium.

This chapter introduces two approaches for studying non-equilibrium dynamics, primarily following [11–13, 15, 16]. The first approach is the Lindblad formalism, where the Lindblad master equation provides a framework for describing open quantum systems, capturing the effects of dissipation in a controlled way. Subsequently, the Keldysh formalism is used to construct a non-equilibrium quantum field theory that enables the analysis of correlated non-equilibrium processes and captures memory effects, which are not accessible within the Lindblad formalism. Particular emphasis will be placed on how to compute non-equilibrium steady states.

1.1 Lindblad Master Equation

The Lindblad formalism is used to describe the dynamics of a system of interest with few degrees of freedom, coupled to a large bath containing many degrees of freedom. The goal is to describe the dynamics of this scenario with a focus on the system rather than the bath. This is because, due to its size, the bath remains effectively unchanged by the system. On the other hand, the bath introduces non-unitary dynamics in the system. In the simplest formulation, this occurs as a gain or loss of particles in the system. The total Hamiltonian describing this

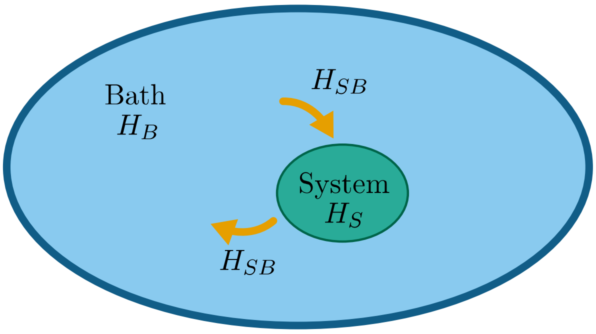

Figure 1.1: Illustration of a system, described by H_S, embedded in a large bath, described by H_B. The interaction between the system and the bath is given by H_{SB}.

scenario is divided into three parts, namely the system, the bath and the system bath coupling, $H = H_S + H_B + H_{SB}$, illustrated in Figure 1.1. The starting point is to treat the system-bath coupling, H_{SB}, as an interaction. This is most conveniently done in the interaction picture, where, the time evolution of the density matrix equation is governed by the von Neumann equation

$$\dot{\rho}^I(t) = -i\left[H^I_{SB}(t), \rho^I(t)\right], \tag{1.2}$$

where ρ is the density matrix, and the superscript I denotes the interaction picture. In anticipation of the Born approximation and to simplify counting the orders of the interaction, the system-bath coupling is defined to be $H^I_{SB}(t) = \alpha V(t)$ where $\alpha \ll 1$ is the coupling strength. By formally integrating Equation (1.2), the density matrix is given by

$$\rho^I(t) = \rho^I(0) - i\alpha \int_0^t dt' \left[V(t'), \rho^I(t')\right]. \tag{1.3}$$

Substituting the integrated form of the density matrix into the equation of motion gives

$$\dot{\rho}^I(t) = -i\alpha\left[V(t), \rho^I(0)\right] - \alpha^2 \int_0^t dt' \left[V(t), \left[V(t'), \rho^I(t')\right]\right]. \tag{1.4}$$

Since the focus is on the system rather than the bath, the goal is to derive an equation of motion for the reduced density matrix. The reduced density matrix is obtained by taking a partial trace over the bath degrees of freedom, $\rho_S(t) = \mathrm{tr}_B\{\rho\}$. Assuming that at the initial time $t = 0$, the system and the bath are uncorrelated, meaning that the density matrix can be factorized as $\rho(0) = \rho_S(0) \otimes \rho_B(0)$ [17]. Additionally, it is assumed that the initial bath expectation value of the interaction term vanishes, $\mathrm{tr}_B\{\rho_B(0)V(t)\} = 0$. Thus, only the second term in the equation of motion survives. However, to proceed further, several more assumptions are needed to be introduced. Firstly, as previously mentioned, the bath is assumed to remain unaffected by the system due to its large size. As a result, the time dependence of the density matrix mostly comes purely from the system, such that $\rho(t) = \rho_S(t)\rho_B$. Secondly, the timescales of the bath are assumed to be much shorter than those of the system. This means that the bath correlations decay rapidly, allowing the upper limit of the integral to be extended to infinity. This is the Markovian approximation, reflecting the absence of memory effects. Finally, only terms of $\mathcal{O}(\alpha^2)$ are kept, which is valid for weak system-bath coupling. This is the Born approximation to second order. Together, these assumptions are collectively known as the Born-Markov approximation, under which the equation of motion simplifies to

$$\dot{\rho}^I_S(t) = -\alpha^2\, \mathrm{tr}_B\left\{\int_0^\infty dt' \left[V(t), \left[V(t'), \rho^I_S(t')\rho_B\right]\right]\right\}. \tag{1.5}$$

For simplicity, the system-bath coupling is described by $V = \sum_i \left(a^\dagger b_i + b_i^\dagger a \right)$, where a is a system operator and b_i is a bath operator with many degrees of freedom i. The equation of motion becomes

$$\begin{aligned}\dot{\rho}_S^I(t) = -\alpha^2 \sum_{i,j} \int_0^\infty dt' \, \mathrm{tr}_B \Bigg\{ \Big[a^\dagger(t) b_i(t) + b_i^\dagger(t) a(t), \\ \Big[a^\dagger(t') b_j(t') + b_j^\dagger(t') a(t'), \rho_S^I(t') \rho_B \Big] \Big] \Bigg\}.\end{aligned} \tag{1.6}$$

Since the b operators only act on the bath, the expectation value with respect to the bath density matrix, ρ_B, can be explicitly taken. Expanding the commutators and grouping the bath terms together gives

$$\begin{aligned}\dot{\rho}_S^I(t) = -\alpha^2 \int_0^\infty dt' \Bigg[& \Big(a^\dagger(t) a(t') \rho_S^I(t') - a(t') \rho_S^I(t') a^\dagger(t) \Big) \sum_{i,j} \left\langle b_i(t) b_j^\dagger(t') \right\rangle_B \\ & - \Big(a^\dagger(t) \rho_S^I(t') a(t') - \rho_S^I(t') a(t') a^\dagger(t') \Big) \sum_{i,j} \left\langle b_j^\dagger(t') b_i(t) \right\rangle_B \\ & + \Big(a(t) a^\dagger(t') \rho_S^I(t') - a^\dagger(t') \rho_S^I(t') a(t) \Big) \sum_{i,j} \left\langle b_i^\dagger(t) b_j(t') \right\rangle_B \\ & - \Big(a(t) \rho_S^I(t') a^\dagger(t') - \rho_S^I(t') a^\dagger(t') a(t') \Big) \sum_{i,j} \left\langle b_j(t') b_i^\dagger(t) \right\rangle_B ,\end{aligned} \tag{1.7}$$

where $\langle b_i(t) b_j(t') \rangle_B = \langle b_i^\dagger(t) b_j^\dagger(t') \rangle_B = 0$. The timescales of the bath are assumed to be much shorter than those of the system, meaning they can be approximated as $\sum_{i,j} \langle b_i^\dagger(t) b_j(t') \rangle_B = \gamma^+ \delta(t - t')$ and $\sum_{i,j} \langle b_i(t) b_j^\dagger(t') \rangle_B = \gamma^- \delta(t - t')$. Substituting these expressions into the equations of motion and taking the integral gives the final result

$$\begin{aligned}\dot{\rho}_S^I(t) = \alpha^2 \Bigg(& \gamma^+ \left(a^\dagger(t) \rho_S^I(t) a(t) - \frac{1}{2} \left\{ a(t) a^\dagger(t), \rho_S^I(t) \right\} \right) \\ & + \gamma^- \left(a(t) \rho_S^I(t) a^\dagger(t) - \frac{1}{2} \left\{ a^\dagger(t) a(t), \rho_S^I(t) \right\} \right) \Bigg),\end{aligned} \tag{1.8}$$

where, for readability, a factor of 2 has been absorbed into the constants. Since the coupling constants γ^+ and γ^- originate from equilibrium bath correlators, the ratio of the two coupling constants is given by

$$\gamma^+ = \gamma^- e^{-\beta\delta}, \tag{1.9}$$

where δ is the energy of the bath mode, and β is the inverse temperature of the bath.

Going back to the Schrödinger picture, the master equations takes the standard Lindblad form

$$\dot{\rho}_S = -i[H_0, \rho_S] + \sum_i \gamma_i \left(L_i \rho_S L_i^\dagger - \frac{1}{2} \left\{ L_i^\dagger L_i, \rho_S \right\} \right), \tag{1.10}$$

where γ is the coupling constant, and L_i corresponds to the system operators coupled to the bath. These operators are usually referred to as jump or Lindblad operators. This master equation is trace-preserving, as $\partial_t \mathrm{tr}\{\rho_S(t)\} = 0$, which follows directly from the cyclic property of the trace. Furthermore, the time evolution is completely positive, provided that $\gamma_i > 0$. This can be seen by noting that the equation can be rewritten as $\rho(t) = e^{\mathcal{L}t}\rho(0)$, where $\mathcal{L}$, the Liouvillian, is a superoperator acting on the density matrix from both the left and the right. Since $\mathcal{L}$ is Hermitian, it preserves the positivity when starting from a physical initial condition $\rho(0)$.

1.1.1 Thermalization

Temperature is not a well defined quantity in non-equilibrium. However, since the bath remains in thermal equilibrium, the system is expected to thermalize and eventually reach the same temperature as the bath. To show this, the thermalization of a free band of fermions coupled to a heat bath is analyzed, given by the following Hamiltonian

$$H = \sum_{k,\sigma} \varepsilon_k^c c_{k\sigma}^\dagger c_{k\sigma} + \sum_{n,\alpha} \varepsilon_n^b b_{n\alpha}^\dagger b_{n\alpha} + V \sum_{k,\sigma,n,\alpha} \left(b_{n\alpha}^\dagger c_{k\sigma} + c_{k\sigma}^\dagger b_{n\alpha} \right), \tag{1.11}$$

where $c_{k\sigma}^\dagger$ and $b_{n\alpha}^\dagger$ are creation operators for the system and bath fermions, respectively, ε_k^c and ε_n^b are their respective dispersion relations, and V is the system-bath coupling strength. Following the Lindblad construction, the heat bath can be incorporated into the master equation using the following two Lindblad operators

$$\gamma_k^p L[c_{k\sigma}^\dagger], \; \gamma_k^r L[c_{k\sigma}]. \tag{1.12}$$

Physically, γ_k^p represents the gain of particles from the bath to the system, while γ_k^r represents the loss of particles from the system to the bath. These rates can be related to the Fermi distribution f by

$$\gamma_k^p \sim V^2 f(\varepsilon_k^b), \qquad \gamma_k^r \sim V^2(1 - f(\varepsilon_k^b)). \tag{1.13}$$

As expected, the emission rate is proportional to the number of fermions in the bath, while the absorption rate is proportional to the number of holes in the bath.

The goal is to determine whether the particle number of the system fermions reaches a thermal distribution. To do this, it is helpful to derive an equation of motion for the expectation value of an operator from the master equation of the density matrix. Starting from $d_t \langle O(t) \rangle = d_t \, \mathrm{tr}\{O(t)\rho\} = \mathrm{tr}\{O\dot{\rho}(t)\}$, the time evolution is then given by

$$\frac{d\langle O \rangle}{dt} = i \langle [O, H_0] \rangle + \sum_\alpha \gamma_\alpha \left(\left\langle L_\alpha^\dagger O L_\alpha \right\rangle - \frac{1}{2} \left\langle \left\{ L_\alpha^\dagger L_\alpha, O \right\} \right\rangle \right). \tag{1.14}$$

For the particle number $n_{k\sigma} = c_{k\sigma}^\dagger c_{k\sigma}$, the equation of motion becomes

$$\frac{dn_{k\sigma}}{dt} = \gamma_k^p - (\gamma_k^p + \gamma_k^r) n_{k\sigma}. \tag{1.15}$$

Solving this differential equation, the time-dependent solution for the particle number is

$$n_{k\sigma}(t) = \frac{\gamma_k^p}{\gamma_k^r + \gamma_k^p} + Ae^{-(\gamma_k^r + \gamma_k^p)t}, \tag{1.16}$$

where A is a constant determined by the initial conditions. In the steady state, defined by taking the limit $t \to \infty$ and by a vanishing time derivative, $dn_{k\sigma}/dt = 0$, the solution simplifies to

$$\gamma_k^p - (\gamma_k^p + \gamma_k^r)\bar{n}_{k\sigma} = 0 \Rightarrow \bar{n}_{k\sigma} = \frac{\gamma_k^p}{\gamma_k^p + \gamma_k^r} = f(\varepsilon_k^b), \tag{1.17}$$

where the bar represents the steady state value. This result demonstrates that the system evolves into a thermal equilibrium, governed by the Fermi distribution of the bath.

1.1.2 Cumulant expansion

When interacting systems are considered, the dynamics become significantly more complex. The density matrix scales exponentially with the system size, N, making direct numerical simulations infeasible. As a result, rather than tracking the full density matrix, the time evolution analysis is restricted to a few relevant expectation values. However, in interacting systems, the equation of motion for an expectation value of an operator typically generates terms which contain expectation values of higher-order operators. This hierarchy problem prevents a closed form solution, making it necessary to develop an approximate method. The cumulant expansion provides a systematic method for truncating the hierarchy by excluding higher-order cumulants, thereby yielding a manageable set of equations.

Cumulants are defined via derivatives of the logarithm of the moment-generating functional. For a classical stochastic variable x, it is given by

$$\ln \left\langle e^{Jx} \right\rangle = \left\langle e^{Jx} - 1 \right\rangle_C, \tag{1.18}$$

where the subscript C denotes the connected part of the expectation value, which corresponds to the cumulant, and J is a source term. Since quantum operators do not commute, this usual construction cannot be directly applied. Luckily, for canonically commuting operators the generating functional can be constructed by equipping the exponential function with an operator ordering [18]. This allows for the following property to be recovered

$$\mathcal{T} e^{x+y} = \mathcal{T} e^x e^y, \tag{1.19}$$

where $\mathcal{T}$ denotes the specific operator ordering used. Using this new definition for the exponential function, the cumulant generating functional can be constructed as

$$\ln Z = \ln \left\langle e^{Ja} \right\rangle \tag{1.20}$$

where a are the quantum operators of interest. The cumulants of a can now be obtained by taking derivatives of $\ln Z$ with respect to the sources J, evaluated at $J = 0$. An important feature of the cumulant expansion is that higher-order cumulants become progressively smaller when the system-bath coupling is small. This enables systematic truncation, resulting in a closed set of equations of motion that effectively capture the dynamics of the relevant quantities in the system. While the operator ordering plays a crucial role in defining the generating function, its specific choice is not essential. This will be the basis to construct a generating functional for a non-equilibrium quantum field theory.

1.2 Non-equilibrium Quantum Field Theory

Many physical systems, from driven quantum materials to open systems with strong system-bath coupling, exhibit behavior that cannot be captured by the Markov-Born approximation, making

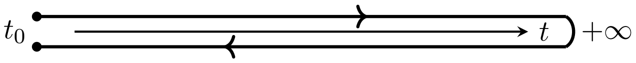

Figure 1.2: The Keldysh contour where the positive forward branch goes from t_0 to ∞, while the negative backwards branch goes from ∞ to t_0. The slight displacement of the branches above and below the real time axis is purely for illustrative purposes.

the Lindblad formalism inadequate. In such cases, a more rigorous framework is required. Non-equilibrium quantum field theory [19] provides a systematic approach to describe these complex dynamics, allowing for a treatment of non-Markovian effects, correlated many-body systems and non-equilibrium processes beyond dissipation.

1.2.1 Keldysh Contour

The construction of a quantum field theory begins with the von Neumann equation for the density matrix

$$\dot{\rho}(t) = -i\left[H(t), \rho(t)\right], \tag{1.21}$$

where $H(t)$ is the Hamiltonian of the system. The formal solution can be obtained to be

$$\rho(t) = U(t, t_0)\rho(t_0)U(t_0, t), \tag{1.22}$$

where U is the unitary time evolution operator, given by

$$U(t, t') = \mathcal{T} e^{-i\int_{t'}^{t} d\bar{t} H(\bar{t})}, \tag{1.23}$$

where $\mathcal{T}$ is the time ordering operator. The expectation value of an arbitrary operator O in the Heisenberg picture is given by

$$\langle O(t)\rangle = \langle U(t_0, t)O(t)U(t, t_0)\rangle . \tag{1.24}$$

This expression implies that the initial state at time t_0 is time evolved to a time t, at which the operator O is applied, after which time evolution reverses and goes back to t_0. Due to the unitary property of the time evolution operator, the resulting state at time t can be further time evolved to ∞ and back by inserting unities of the form $\mathbb{1} = U(\infty, t)U(t, \infty)$. This defines the Keldysh time contour $\mathcal{C}$, illustrated in Figure 1.2, which consists of two branches, a forward branch, which runs from t_0 to ∞, and the backward branch which goes from ∞ to t_0. The crucial point in construction the non-equilibrium partition function, $Z = \mathrm{tr}(\rho(t_0)) = 1$, is to take this time-evolution sequence literally within the time-slicing procedure. By doing so, the partition function can be expressed as [11]

$$Z = \int \mathcal{D}\left[\phi\right] \exp\left\{ i\int_{\mathcal{C}} dt \left[\phi^*(t) i\partial_t \phi(t) - H(\phi^*, \phi)\right]\right\}. \tag{1.25}$$

Decomposing the integral along the contour gives

$$Z = \int \mathcal{D}[\phi] \exp\left\{ i\int_{t_0}^{\infty} dt \left[\phi_+^*(t) i\partial_t \phi_+(t) - H(\phi_+^*, \phi_+)\right] - \left[\phi_-^*(t) i\partial_t \phi_-(t) - H(\phi_-^*, \phi_-)\right]\right\}, \tag{1.26}$$

where the subscript $+$ and $-$ denote the forward and backward branch, respectively. This can be compactly rewritten as

$$Z = \int \mathcal{D}[\phi] \exp\left\{ i \int_{t_0}^{\infty} dt dt' \phi^*(t) G_{\mathcal{C}}^{-1}(t,t') \phi(t') \right\}, \tag{1.27}$$

where $G_{\mathcal{C}}^{-1}$ is the inverse contour Green function, the components of which are given by

$$G_{\mathcal{C}}(t,t') = -i \left\langle \mathcal{T}_{\mathcal{C}} \left\{ \phi(t) \phi^\dagger(t') \right\} \right\rangle \tag{1.28}$$

$$= \begin{pmatrix} -i \left\langle \mathcal{T} \left\{ \phi_+(t) \phi_+^\dagger(t') \right\} \right\rangle & -i\zeta \left\langle \phi_-^\dagger(t') \phi_+(t) \right\rangle \\ -i \left\langle \phi_-(t) \phi_+^\dagger(t') \right\rangle & -i \left\langle \widetilde{\mathcal{T}} \left\{ \phi_-(t) \phi_-^\dagger(t') \right\} \right\rangle \end{pmatrix} = \begin{pmatrix} G^{\mathcal{T}}(t,t') & G^{<}(t,t') \\ G^{>}(t,t') & G^{\widetilde{\mathcal{T}}}(t,t') \end{pmatrix}, \tag{1.29}$$

where $\zeta = \pm 1$ for bosons and fermions respectively, and $\widetilde{\mathcal{T}}$ is the anti-time ordering operator. $\mathcal{T}_{\mathcal{C}}$ is the contour-time ordering operator defined by

$$\left\langle \mathcal{T}_{\mathcal{C}} \left\{ \phi(t) \phi^\dagger(t') \right\} \right\rangle = \theta_{\mathcal{C}}(t,t') \phi(t) \phi^\dagger(t') + \zeta \theta_C(t',t) \phi^\dagger(t') \phi(t), \tag{1.30}$$

where the contour Heaviside step function is given by

$$\theta_{\mathcal{C}}(t-t') = \begin{cases} \theta(t-t') & \text{if } t,t' \in \mathcal{C}^+, \\ \theta(t'-t) & \text{if } t,t' \in \mathcal{C}^-, \\ 1 & \text{if } t \in \mathcal{C}^-, t' \in \mathcal{C}^+, \\ 0 & \text{otherwise.} \end{cases} \tag{1.31}$$

Leading to the contour delta function being defined as

$$\delta_{\mathcal{C}}(t-t') = \partial_t \theta_{\mathcal{C}}(t-t') = \begin{cases} \delta(t-t') & \text{if } t,t' \in \mathcal{C}^+, \\ -\delta(t-t') & \text{if } t,t' \in \mathcal{C}^-, \\ 0 & \text{otherwise.} \end{cases} \tag{1.32}$$

To obtain physical intuition about the information encoded in each component, it is useful to examine their roles individually. The lesser Green function, $G^{<}(t,t')$, provides information about the occupation of states. In equilibrium, it is given by

$$G^{<}(t,t') = i e^{-i\omega(t-t')} n_F(\omega), \tag{1.33}$$

where ω is the energy of the single-particle state and $n_F(\omega) = (e^{\beta\omega} + 1)^{-1}$ is the Bose or Fermi distribution, depending on the statistics. The greater Green function, $G^{>}(t,t')$, provides information about the unoccupied states. In equilibrium, it is given by

$$G^{>}(t,t') = -i e^{-i\omega(t-t')} n_F(-\omega). \tag{1.34}$$

Together, these two Green functions encode information regarding both the spectrum and the occupation of the system. A defining feature of equilibrium is that these two Green functions obey the fluctuation-dissipation theorem in frequency space, given by

$$G^{<}(\omega) = -e^{-\beta\omega} G^{>}(\omega). \tag{1.35}$$

The time ordered Green function, $G^{\mathcal{T}}$, and the anti-time ordered Green function, $G^{\widetilde{\mathcal{T}}}$, can be expressed in terms of the lesser and greater Green functions as

$$G^{\mathcal{T}}(t,t') = \theta(t-t')G^{>}(t,t') + \theta(t'-t)G^{<}(t,t'), \tag{1.36}$$

$$G^{\widetilde{\mathcal{T}}}(t,t') = \theta(t'-t)G^{>}(t,t') + \theta(t'-t)G^{<}(t,t'). \tag{1.37}$$

This implies that only two independent Green functions need to be computed. In explicit time evolutions, the lesser and greater Green functions are typically favored, due to their simpler equations of motion, as will be seen in Section 1.2.4. From this point, the discussion is restricted to the fermionic case. For a detailed discussion of the bosonic case, see [11, 12, 15]. In steady-state calculations, a more convenient representation is often used, achieved by rotating[1] to the Keldysh basis

$$G_{\mathcal{C}}(t,t') = \begin{pmatrix} G^{R}(t,t') & G^{K}(t,t') \\ 0 & G^{A}(t,t') \end{pmatrix}, \tag{1.38}$$

where the retarded and advanced Green functions are defined as

$$G^{R}(t,t') = \theta(t-t')\left(G^{>}(t,t') - G^{<}(t,t')\right), \tag{1.39}$$

$$G^{A}(t,t') = -\theta(t'-t)\left(G^{>}(t,t') - G^{<}(t,t')\right). \tag{1.40}$$

As the occupation is defined by the Fermi function in equilibrium, the retarded Green function is commonly used in equilibrium calculations, as it contains the remaining information about the spectrum. The remaining component is the Keldysh Green function, defined as

$$G^{K}(t,t') = G^{>}(t,t') + G^{<}(t,t'), \tag{1.41}$$

which contains information about the occupation of the system.

1.2.2 Conserving Approximations

When interactions are added to a system, the resulting dynamics often become too complex to be solved exactly, necessitating the use of approximations. In general, physical systems obey certain conservation laws, such as momentum and energy conservation, as well as the continuity equation. While the interaction vertex may respect these conservation laws, approximate formalisms used to compute the full Green function of the system may result in a solution that does not fulfill them. The following construction, introduced by Kadanoff and Baym in [21], provides a framework for constructing approximations that ensure that the final result obeys these conservation laws. This framework can be applied to both equilibrium and non-equilibrium systems. Consider a generic interacting system described by the Hamiltonian

$$\begin{aligned} H = &\int d\vec{x}_1\, \psi^{\dagger}(\vec{x}_1,t)\left(\frac{(-i\vec{\nabla}_1)^2}{2m} + V(\vec{x}_1,t)\right)\psi(\vec{x}_1,t) \\ &+ \frac{1}{2}\int d\vec{x}_1 d\vec{x}_2 \psi^{\dagger}(\vec{x}_1,t)\psi^{\dagger}(\vec{x}_2,t)U(\vec{x}_1-\vec{x}_2)\psi(\vec{x}_1,t)\psi(\vec{x}_2,t). \end{aligned} \tag{1.42}$$

---

[1] Strictly speaking, this is not a true rotation, as the daggered and the non-daggered fields transform in a different way. However, it is conventionally agreed that the Green function is defined this way [11, 20]

The equation of motion for the time ordered Green function in the first time index can be expressed using the four-point function by

$$\begin{aligned}\left(i\frac{\partial}{\partial t_1} - \frac{(-i\vec{\nabla}_1)^2}{2m}\right)G(\vec{x}_1,t_1,\vec{x}_2,t_2) &= \delta(\vec{x}_1-\vec{x}_2)\delta(t_1-t_2)\\ &\quad - i\int d\vec{x}_3 \left\langle \mathcal{T}\psi^\dagger(\vec{x}_3,t_1^+)\psi(\vec{x}_1,t_1)\psi(\vec{x}_3,t_1)\psi^\dagger(\vec{x}_2,t_2)\right\rangle U(\vec{x}_3-\vec{x}_1),\end{aligned} \tag{1.43}$$

while for the second time index

$$\begin{aligned}\left(-i\frac{\partial}{\partial t_2} - \frac{(-i\vec{\nabla}_2)^2}{2m}\right)G(\vec{x}_1,t_1,\vec{x}_2,t_2) &= \delta(\vec{x}_1-\vec{x}_2)\delta(t_1-t_2)\\ &\quad - i\int d\vec{x}_3 \left\langle \mathcal{T}\psi(\vec{x}_1,t_1)\psi^\dagger(\vec{x}_3,t_1^+)\psi^\dagger(\vec{x}_2,t_1)\psi(\vec{x}_3,t_2)\right\rangle U(\vec{x}_3-\vec{x}_2).\end{aligned} \tag{1.44}$$

These two equations can be used to check whether the conservation laws are fulfilled within the approximation. The first case that is checked is the continuity equation, which requires the particle density and current. The particle density is defined as $n(\vec{x}_1,t_1) = -iG(\vec{x}_1,t_1,\vec{x}_2,t_2)\big|_{2\to 1^+}$ and the particle current is given by $\vec{j}(\vec{x}_1,t_1) = -\frac{1}{2m}\left(\vec{\nabla}_1 - \vec{\nabla}_2\right)G(\vec{x}_1,t_1,\vec{x}_2,t_2)\big|_{2\to 1^+}$. The continuity equation is then obtained by subtracting Equations (1.43) and (1.44), and taking the limit $2 \to 1^+$, yielding

$$\begin{aligned}\frac{\partial}{\partial t}n(\vec{x},t) + \vec{\nabla}\cdot\vec{j}(\vec{x},t) = 2i\cdot\int d\vec{x}'\,U(\vec{x}'-\vec{x})\Big[&\left\langle \mathcal{T}\psi^\dagger(\vec{x}',t^+)\psi(\vec{x},t)\psi(\vec{x}',t)\psi^\dagger(\vec{x},t^+)\right\rangle\\ &- \left\langle \mathcal{T}\psi(\vec{x},t)\psi^\dagger(\vec{x}',t^+)\psi^\dagger(\vec{x},t^+)\psi(\vec{x}',t)\right\rangle\Big].\end{aligned} \tag{1.45}$$

If the four-point function for a given approximation has the symmetry

$$\left\langle \mathcal{T}\psi^\dagger(\vec{x}',t^+)\psi(\vec{x},t)\psi(\vec{x}',t)\psi^\dagger(\vec{x},t^+)\right\rangle = \left\langle \mathcal{T}\psi(\vec{x},t)\psi^\dagger(\vec{x}',t^+)\psi^\dagger(\vec{x},t^+)\psi(\vec{x}',t)\right\rangle, \tag{1.46}$$

then the continuity equation is guaranteed to hold. Moreover, it can be shown that other conservation laws, such as momentum, angular momentum and energy conservation are also satisfied under this condition [12, 21].

Typically four-point functions tend to be quite challenging to compute directly. Therefore, it is common to reformulate the expression in terms of the self-energy, which only depends on two-point functions, however, doing so introduces an additional time integral. The condition on the four-point function can be rewritten as a condition on the self-energy [13]. By expressing the right-hand side of Equation (1.45) in terms of the self-energy, the condition becomes

$$\int dx_3\,\left(\Sigma(x_1,x_3)G(x_3,x_1) - G(x_1,x_3)\Sigma(x_3,x_1)\right), \tag{1.47}$$

where $x_i = (\vec{x}_i, t_i)$. Therefore the condition translates to the requirement that the self energy is invariant under interchange of its entry and exit points, $x_1 \leftrightarrow x_3$. In an exact theory, this condition is trivially fulfilled, because for every self-energy diagram there exists a corresponding mirror-imaged one. However, for approximate treatments this symmetry is not necessarily fulfilled. A self energy that satisfies this condition can be constructed by taking a functional derivative of a generating functional $\Phi[G]$

$$\Sigma(x_1,x_2) \sim \frac{\delta\Phi[G]}{\delta G(x_2,x_1)}. \tag{1.48}$$

This is because the derivative guarantees the generation of mirrored self-energy diagrams. Since Σ contains all one particle irreducible diagrams, the generating functional $\Phi[G]$ must contain all two particle irreducible (2PI) diagrams.

1.2.3 Two-Particle Irreducible Effective Action

To formalize the condition on the self energy given in Equation (1.48), a 2PI cumulant generating functional must be constructed. The first step in this processes is to include two-point sources in the moment generating functional

$$Z[R] = \int \mathcal{D}[\psi^*_\alpha, \psi_\alpha] \exp\left\{i\left[S[\psi^*_\alpha, \psi_\alpha] + R_{\alpha\beta}\psi^*_\alpha\psi_\beta\right]\right\}, \tag{1.49}$$

where α contains all quantum numbers, and repeated indices imply summation. With this definition, the second moment is given by the stationarity condition

$$G = \left.\frac{\delta \ln(Z)}{\delta R}\right|_{R\to 0}. \tag{1.50}$$

Since the goal is to construct an effective action that is independent of the source field R, a Legendre transformation is performed

$$\Gamma[G] = -i\ln(Z) + i\,\mathrm{tr}\,GR. \tag{1.51}$$

To gain insight into the structure of $\Gamma[G]$, it is useful to first consider the non-interacting case, where the $Z[R]$ can be explicitly calculated using the Gaussian integral

$$\begin{aligned} Z[R] &= \int \mathcal{D}[\psi^*_\alpha, \psi_\alpha] \exp\left\{i\left[\psi^*_\alpha(G_0^{-1}+R)_{\alpha\beta}\psi_\beta\right]\right\} & (1.52)\\ &= \det\left[G_0^{-1}+R\right] = \exp\left\{\mathrm{tr}\ln\left[G_0^{-1}+R\right]\right\}. & (1.53)\end{aligned}$$

The next step is to remove the R dependence by computing an expression for the 2-point function

$$G[R] = \frac{\delta \ln(Z)}{\delta R} = \frac{\delta}{\delta R}\mathrm{Tr}\ln\left(G_0^{-1}+R\right) = \left(G_0^{-1}+R\right)^{-1}. \tag{1.54}$$

This leads to the relation $GR = 1 - GG_0^{-1}$. Using these results, the Legendre transform can be performed, yielding

$$\Gamma[G] = i\,\mathrm{tr}\ln(G) - i\,\mathrm{tr}\big(G_0^{-1}G - 1\big). \tag{1.55}$$

When an interaction is introduced into the Hamiltonian, it will contribute an additional term in the 2PI effective action, which then takes the form

$$\Gamma[G] = i\,\mathrm{tr}\ln(G) - i\,\mathrm{tr}\big(G_0^{-1}G - 1\big) + \Phi[G], \tag{1.56}$$

where $\Phi[G]$ is the so-called Luttinger Ward functional, which contains all the 2PI diagrams. Thus, any equations of motion derived from $\Gamma[G]$ are necessarily conserving.

1.2.4 Kadanoff-Baym Equations of Motion

Now the equations of motion for the full 2-point function can be derived from the stationarity condition of the effective action

$$\frac{\delta\Gamma[G]}{\delta G_{\alpha\beta}} = 0, \tag{1.57}$$

which leads to the Dyson equation

$$iG^{-1}_{\beta\alpha} - i(G_0^{-1})_{\beta\alpha} + \frac{\delta\Phi[G]}{\delta G_{\alpha\beta}} = 0, \tag{1.58}$$

where the self-energy is defined through the functional derivative of the Luttinger-Ward functional as

$$\Sigma_{\beta\alpha} = -i\frac{\delta\Phi[G]}{\delta G_{\alpha\beta}}, \tag{1.59}$$

and automatically satisfies the conservation condition given in Equation (1.48). Since G_0^{-1} contains the explicit time derivative, it is convenient to multiply Equation (1.58) by G, resulting in

$$[G_0^{-1}\star G](t,t') = \delta_{\mathcal{C}}(t-t') + [\Sigma\star G](t,t'), \tag{1.60}$$

where $[a\star b](t,t') \equiv \int_{\mathcal{C}} d\bar{t}\, a(t,\bar{t})b(\bar{t},t')$. To derive equations of motion for the lesser and greater Green functions, it is useful to first consider a general product and decompose the time indices in the forward and backward branches of the contour

$$[a\star b](t,t') = \int_{-\infty}^{\infty} dt_1^+\, a(t,t_1^+)b(t_1^+,t') - \int_{-\infty}^{\infty} dt_1^-\, a(t,t_1^-)b(t_1^-,t'). \tag{1.61}$$

The lesser component is obtained by setting t and t' on their respective branches, as in $[a\star b]^<(t,t') \equiv [a\star b](t^+,t'^-)$. Substituting this into the expression gives

$$[a\star b]^<(t,t') = \int_{-\infty}^{\infty} dt_1^+\, a(t^+,t_1^+)b(t_1^+,t'^-) - \int_{-\infty}^{\infty} dt_1^-\, a(t^+,t_1^-)b(t_1^-,t'^-) \tag{1.62}$$

$$= \int_{-\infty}^{\infty} dt_1\, \Big[a^T(t,t_1)b^<(t_1,t') - a^<(t,t_1)b^{\widetilde{T}}(t_1,t')\Big]. \tag{1.63}$$

Using the definitions of the time ordered and the retarded components it can be seen that

$$a^T(t,t') = a^R(t,t') + a^<(t,t') = \theta(t-t')a^>(t,t') + \theta(t'-t)a^<(t,t'), \tag{1.64}$$

and similarly $a^{\widetilde{T}}(t,t') = a^<(t,t') + a^A(t,t')$. Therefore the general product becomes

$$[a\star b]^<(t,t') = \int_{-\infty}^{\infty} dt_1\, \big[\big(a^R(t,t_1) + a^<(t,t_1)\big)b^<(t_1,t') - a^<(t,t_1)\big(b^<(t_1,t') - b^A(t_1,t')\big)\big] \tag{1.65}$$

$$= \int_{-\infty}^{\infty} dt_1\, \big[a^R(t,t_1)b^<(t_1,t') + a^<(t,t_1)b^A(t_1,t')\big] \tag{1.66}$$

$$= [a^R\cdot b^< + a^<\cdot b^A](t,t'), \tag{1.67}$$

where $[a\cdot b](t,t') \equiv \int_{-\infty}^{\infty} d\bar{t}\, a(t,\bar{t})b(\bar{t},t')$. Substituting this result into the Dyson equation produces the equation of motion for the lesser Green function

$$[G_0^{-1}\cdot G]^<(t,t') = [\Sigma^R\cdot G^< + \Sigma^<\cdot G^A](t,t'). \tag{1.68}$$

Similarly, for the greater Green function, the equation of motion is given by

$$[G_0^{-1}\cdot G]^>(t,t') = [\Sigma^R\cdot G^> + \Sigma^>\cdot G^A](t,t'). \tag{1.69}$$

Steady-State Equations

When the interest is solely in steady states properties, whether in equilibrium or far from equilibrium, these equations can be significantly simplified. This simplification arises from the fact that, in the steady state, time-translational invariance holds. Meaning that the Green functions only depend on the time difference $t - t'$ and not on the absolute times explicitly. This property allows for a well-defined Fourier transformation into the frequency domain. The Dyson equation in Keldysh space, given in Equation (1.60), can be expressed in frequency space as

$$\begin{pmatrix} G^R(\omega) & G^K(\omega) \\ 0 & G^A(\omega) \end{pmatrix} = \begin{pmatrix} G_0^{R^{-1}}(\omega) - \Sigma^R(\omega) & G_0^{K^{-1}}(\omega) - \Sigma^K(\omega) \\ 0 & G_0^{A^{-1}}(\omega) - \Sigma^A(\omega) \end{pmatrix}^{-1} . \tag{1.70}$$

The retarded component is given by

$$G^R(\omega) = \left(G_0^{R^{-1}}(\omega) - \Sigma^R(\omega)\right)^{-1} , \tag{1.71}$$

and the Keldysh component is given by

$$G^K(\omega) = -\left(G_0^{R^{-1}}(\omega) - \Sigma^R(\omega)\right)^{-1} \left(G_0^{K^{-1}}(\omega) - \Sigma^K(\omega)\right) \left(G_0^{A^{-1}}(\omega) - \Sigma^A(\omega)\right)^{-1} \tag{1.72}$$

$$= G^R(\omega)\Sigma^K(\omega)G^A(\omega). \tag{1.73}$$

Here, $G_0^{K,-1}(\omega)$, which contains information about the initial occupation, has been omitted because in any steady state the initial conditions are irrelevant. The steady state equations for the greater and lesser Green functions can be shown to be

$$G^{\lessgtr}(\omega) = G^R(\omega)\Sigma^{\lessgtr}(\omega)G^A(\omega). \tag{1.74}$$

1.2.5 Bath Coupling

Once again, the thermalization of a free band of fermions coupled to a heat bath is analyzed. The goal is to compare the difference between the Lindblad thermalization shown in Section 1.1.1, and thermalization with quantum field theory techniques. The Hamiltonian is given by

$$H = \sum_{k,\sigma} \varepsilon_k^c c_{k\sigma}^\dagger c_{k\sigma} + \sum_{n,\alpha} \varepsilon_n^b b_{n\alpha}^\dagger b_{n\alpha} + V \sum_{k,\sigma,n,\alpha} \left(b_{n\alpha}^\dagger c_{k\sigma} + c_{k\sigma}^\dagger b_{n\alpha}\right) , \tag{1.75}$$

where $c_{k\sigma}^\dagger$ and $b_{n\alpha}^\dagger$ are creation operators for the system and bath fermions, respectively. Technically, this problem is trivial because the Hamiltonian is bilinear which can be solved exactly. Nonetheless, this example provides physical insight into how a system thermalizes.

The bath is assumed to be in equilibrium and not renormalized by the system, meaning that its lesser and greater Green functions in frequency space are given by

$$G_b^<(\omega) = 2\pi i f(\omega) A_b(\omega), \tag{1.76}$$

$$G_b^>(\omega) = -2\pi i(1 - f(\omega))A_b(\omega), \tag{1.77}$$

where $f(\omega)$ is the Fermi distribution and $A_b(\omega)$ is the spectral function of the bath. This implies that the Keldysh Green function of the bath is

$$G_b^K(\omega) = -2\pi i(1 - 2f(\omega))A_b(\omega) = -2\pi i \tanh\left(\frac{\beta\omega}{2}\right) A_b(\omega). \tag{1.78}$$

The self-energy[2] of the fermions is given by

$$\Sigma_c(\omega) = -i\pi V^2 \sum_{n,\alpha} G_{b_\alpha}(\omega, n) = -i\Gamma, \tag{1.79}$$

where $\Gamma(\omega) = \pi V^2 \sum_{n,\alpha} G_{b_\alpha}(\omega, n)$ is the hybridization strength, assumed to be a constant. Using Equation (1.73), the Keldysh Green function of the fermions is computed as

$$G_c^K(k,\omega) = \frac{-2\pi i\Gamma}{\left(\omega - \varepsilon_k^c\right)^2 + \Gamma^2} \tanh\left(\frac{\beta\omega}{2}\right). \tag{1.80}$$

In the limit of the bath coupling going to zero, the Keldysh Green function simplifies to

$$G_c^K(k,\omega) \overset{\Gamma\to 0}{=} -2\pi i \tanh\left(\frac{\beta\omega}{2}\right) \delta\left(\omega - \varepsilon_k^c\right) = -2\pi i \tanh\left(\frac{\beta\omega}{2}\right) A_f(k,\omega), \tag{1.81}$$

where $A_c(k,\omega)$ is the momentum dependent spectral function of the fermions, demonstrating that the system has fully thermalized to the temperature of the bath. This results in a thermal spectrum and, crucially, ensures that the fluctuation dissipation theorem holds in the system. This is in contrast to the Lindblad approach, which can only enforce a thermal density matrix, and due to the Markovian approximation, can not enforce a thermal spectrum. Therefore, if fluctuation-dissipation theorem as well as a thermal spectrum is required, as is the case when non-Markovian effects are important, this type of bath coupling becomes essential, and a Lindblad bath coupling is not sufficient.

---

[2] Since the Hamiltonian describes a free Hamiltonian this is technically not a ”true” self-energy. In this context, it is more accurately referred to as the hybridization function.

Chapter 2

Strongly-Correlated Electron Systems

Among the many fields within condensed matter physics, strongly correlated electron systems stand out as particularly intriguing and conceptually rich. In these systems, strong correlations are induced by the interaction between the electrons, which typically constitutes as the largest energy scale in the system. In contrast to many phenomena in physics, which can be described using single particle effects, the physics of strongly correlated systems is inherently many-body in nature.

Famously, the behavior of many-body systems cannot be understood by simply adding up the behavior of their individual constituents [22]. Moreover, due to the strong correlations, typical perturbative approaches tend to fail. Therefore, such systems are sitting in the valley of our understanding, making them particularly interesting to research. Although it is known that these systems display a large variety of interesting phases of matter, it still comes as a surprise, how rich the field actually is. Examples of which are high-T_C superconductors [23, 24], unconventional superconductors [25], heavy fermion systems [26], Moiré materials [27] and many more [28–30].

In this thesis, one of the main focuses are heavy fermion systems. To give an overview and provide a proper foundation of this subject, first the Kondo effect will be discussed. The effect occurs when a small number of magnetic impurities are embedded in a metal host. A typical model to describe this effect is the single impurity Anderson model. In the first part of this chapter, this model will be discussed in detail, and the auxiliary particle method will be used to provide a solution to the model. Afterwards, this scenario will be extended by introducing an impurity on every site, leading to the Anderson lattice model. For this model, the dynamical mean field theory has to be introduced and will then be used to provide a solution to the Anderson lattice model.

2.1 A Brief History of the Kondo Effect

When a metal is cooled from room temperature, its resistivity decreases due to a reduction in electron-phonon scattering as the phonons freeze out. This behavior continues until the resistivity reaches a constant value determined by residual scattering from impurities. This standard picture is covered in most textbooks [31]. Contrary to this typical behavior, an experiment in 1930 showed that the resistivity of several metals increases below $4K$ [32]. In 1934, further experiments measured the resistivity in gold [6], which demonstrated a resistivity minimum at a certain characteristic temperature T_K, as shown in Figure 2.1. It was clear

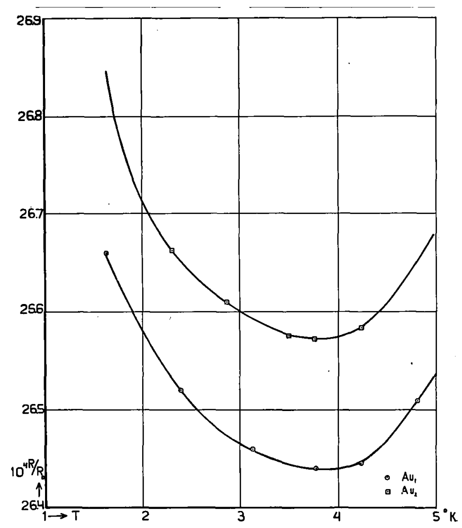

Figure 2.1: Resistance of impure gold wires between $1K$ and $5K$ taken from [6]. At high temperatures the usual phonon contribution $\sim T^5$ is observed, however at low temperatures the resistance rises again following a logarithmic dependence, leading to a resistivity minimum around $T \sim 4K$.

that the gold contained a small amount of impurities, specifically a small amount of transition metals which have a magnetic moment [33]. Later studies found that this unusual phenomenon also occurs in other noble metals [34], with the resistivity exhibiting a characteristic logarithmic dependence, $\rho \sim \ln T/T_K$. This phenomenon puzzled physicists for decades until the 1960s, when J. Kondo provided an explanation which involved spin-flip scattering of the conduction electrons and a single local magnetic moment [35]. Kondo proposed the following model

$$H_K = \sum_{k\sigma} \varepsilon_k c^\dagger_{k\sigma} c_{k\sigma} + J\vec{S} \cdot \vec{s}_0, \tag{2.1}$$

where $c^\dagger_{k\sigma}$ creates a conduction electron with momentum k and spin σ, $\varepsilon_k \in [-D, D]$ is the conduction electron dispersion with half-bandwidth D, and J is the anti-ferromagnetic coupling between the conduction electron spin and the local moment. $\vec{S}$ is the spin operator of the local moment, and the conduction electron spin operator is given by $\vec{s}_i = \sum_{\sigma,\sigma'} c^\dagger_{i\sigma} \vec{\sigma}_{\sigma,\sigma'} c_{i\sigma'}$, where $\vec{\sigma}$ is the vector of Pauli matrices. Using second order perturbation theory Kondo managed to obtain a logarithmic correction to the resistivity

$$\rho(T) = \rho_0 + aT^2 + bT^5 + c \ln T/T_K, \tag{2.2}$$

where ρ_0 is the residual resistivity, and a, b, c are fitting parameters. The T^2 term arises from Fermi liquid behavior, the T^5 term from phonon scattering and the last logarithmic term is the new additional term that arises from the spin-flip scattering mechanism. This advancement led to the effect being named after Kondo, and the characteristic temperature at which this phenomenon occurs, T_K, became known as the Kondo temperature.[1] However, the logarithmic term introduced a new problem, as it suggests that the resistivity diverges as $T \to 0$. Since this result comes from a perturbative approach, it signals a breakdown of perturbation theory, indicating that the ground state of the system cannot be accessed using perturbative methods. In 1970, P. W. Anderson introduced the concept of perturbative renormalization group, showing

---

[1] Originally, Kondo described this as a Fermi surface effect [36].

that the low temperature regime of the Kondo model is equivalent to the same model but with much larger couplings [37]. This suggests that, at low temperatures, the local moment interacts so strongly with the conduction electrons that a singlet is formed. This singlet acts as a potential scatterer, and the ground state becomes a Fermi liquid [38]. However, since this is still based on a perturbative approach, a complete solution is still required. In 1975, K. G. Wilson developed the numerical renormalization group [39] method, which provided a numerical exact solution to the model. Using this approach, he was able to confirm Anderson's predictions and that the ground state is a Fermi liquid, thus solving the Kondo problem.

2.2 Single Impurity Anderson Model

In 1961, Anderson proposed a model to study the formation of local moments in solids [40]. In 1966, following the success of the Kondo model, it was shown that the Kondo Hamiltonian is a low-energy projection of the Anderson model, where double occupancy is forbidden [41]. The Anderson model has since become more widely used due to it's straightforward extension to include orbital degeneracy, which is essential for discussing realistic materials. The simplest version of the Anderson impurity model describes a single magnetic impurity embedded in a sea of conduction electrons. The Hamiltonian is given by

$$H_{\mathrm{SIAM}} = \sum_{k\sigma} \varepsilon_k c^\dagger_{k\sigma} c_{k\sigma} + \varepsilon_d \sum_{\sigma} d^\dagger_\sigma d_\sigma + V \sum_{k\sigma} \left(c^\dagger_{k\sigma} d_\sigma + h.c. \right) + U n^d_\uparrow n^d_\downarrow, \tag{2.3}$$

where $c^\dagger_{k\sigma}$ creates a conduction electron with momentum k and spin σ, $\varepsilon_k \in [-D, D]$ is the conduction electron dispersion with half-bandwidth D, $d^\dagger_\sigma$ creates an impurity electron with spin σ, and ε_d is the impurity energy level. The particle number operator is $n^d_\sigma = d^\dagger_\sigma d_\sigma$, V describes the hybridization between the conduction electrons and the impurity, and U is the on-site Coulomb interaction between the localized impurity electrons.

The local moment regime of this model, illustrated in Figure 2.2, is when $\varepsilon_d < \varepsilon_F$, where ε_F is the Fermi energy, and when the Coulomb interaction is larger than the bandwidth $U \gtrsim D$. The large Coulomb interaction restricts double occupancy, favoring single occupancy and thus forming the local moment. However, there is always a finite amplitude for the local spin to fluctuate $c_\uparrow + d_\downarrow \rightleftharpoons c_\downarrow + d_\uparrow$. These spin flip terms are the ones that induce the Kondo effect. Due to the large interaction, the model becomes difficult to treat, particularly with quantum field methods, as the exclusion of double occupancy constitutes a nonholonomic constraint. In the following subsections, the auxiliary particle method will be introduced as an elegant way to treat the constraint.

2.2.1 Auxiliary Particles

One of the main challenges in solving the Hamiltonian in Equation (2.3) is the non-holonomic constraint $n^d \leq 1$, which arises from the strong Coulomb repulsing. This constraint generally prevents the straightforward construction of a path integral. Auxiliary particles methods provide a powerful framework for addressing such constraints. The key idea is to introduce a field operator corresponding to every possible occupation state of the impurity [42–44]. This leads to, see Figure 2.2a, the following definitions

$$\begin{aligned} b^\dagger \left|\mathrm{vac}\right\rangle &= \left|0\right\rangle, \\ f^\dagger_\sigma \left|\mathrm{vac}\right\rangle &= \left|\sigma\right\rangle, \\ a^\dagger \left|\mathrm{vac}\right\rangle &= \left|\uparrow\downarrow\right\rangle, \end{aligned} \tag{2.4}$$

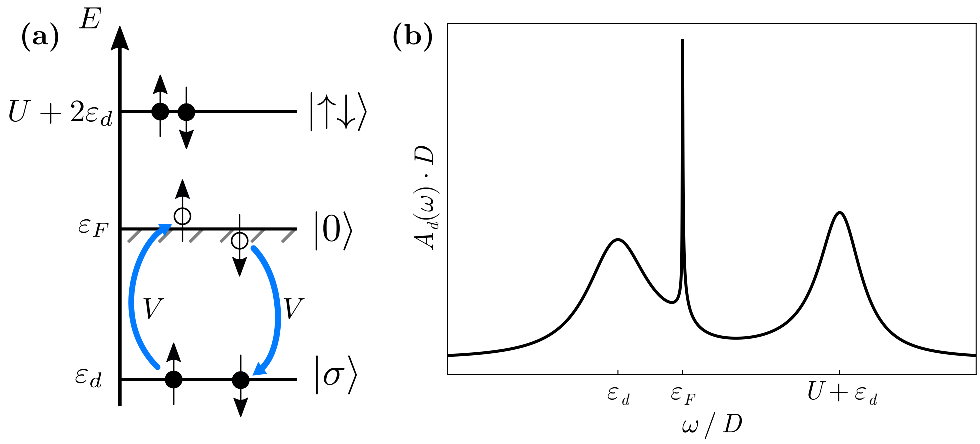

Figure 2.2: **(a)** Impurity level scheme for the single impurity Anderson model in the local moment regime, where $\varepsilon_d < \varepsilon_F$ and the onsite repulsion U is large. Spin-flip processes which are second-order in V are illustrated. These involve transitions between the impurity and conduction electrons and lead to the Kondo effect. **(b)** Impurity spectral function $A_d(\omega)$ show the characteristic three peak structure. The left and right peaks correspond to transitions involving the singly occupied impurity state and doubly occupied impurity state, respectively. The sharp central peak is the Kondo peak arising from the resonant spin-flip scattering.

where $b^\dagger$ and $a^\dagger$ are bosonic creation operators corresponding to the empty and doubly occupied state, respectively. $f_\sigma^\dagger$ is a fermionic creation operator corresponding to the singly occupied state. The impurity can be in at most one of the states introduced by the auxiliary particles. Therefore, the system must be restricted to this physical subsector, which is achieved by enforcing the following holonomic constraint

$$Q = \sum_\sigma f_\sigma^\dagger f_\sigma + b^\dagger b + a^\dagger a = 1. \tag{2.5}$$

The constraint ensures that a product state of these four basis states is not allowed, however, a superposition is. By examining the mapping of the d-operators on the auxiliary particle states, a faithful representation is achieved when

$$d_\sigma^\dagger = b f_\sigma^\dagger + \sigma a^\dagger f_{-\sigma}. \tag{2.6}$$

Using this representation, the Hamiltonian given in Equation (2.3), can now be rewritten in terms of the auxiliary particle operators as

$$H = \sum_{k\sigma} \varepsilon_k c_{k\sigma}^\dagger c_{k\sigma} + \varepsilon_d \sum_\sigma f_\sigma^\dagger f_\sigma + (U + 2\varepsilon_d)\, a^\dagger a + V \sum_{k\sigma} \left(c_{k\sigma}^\dagger (b^\dagger f_\sigma + \sigma f_{-\sigma}^\dagger a) + h.c. \right). \tag{2.7}$$

The original quartic term is now a bilinear term in Equation (2.7), while the hybridization term, which was originally bilinear, has become the new interaction term. Typically, the hybridization strength is a small parameter, allowing for a well-defined perturbative approach. This means that now quantum field theory techniques can be applied to solve the problem. As mentioned earlier, in the local moment regime, the interaction strength is large and double occupation is suppressed. This allows all terms proportional to a to be discarded, simplifying the constraint to

$$Q = \sum_\sigma f_\sigma^\dagger f_\sigma + b^\dagger b = 1, \tag{2.8}$$

and leading to the so-called infinite-U Hamiltonian

$$H = \sum_{k\sigma} \varepsilon_k c^\dagger_{k\sigma} c_{k\sigma} + \varepsilon_d \sum_\sigma f^\dagger_\sigma f_\sigma + V \sum_{k\sigma} \left(c^\dagger_{k\sigma} b^\dagger f_\sigma + h.c. \right). \tag{2.9}$$

2.2.2 Auxiliary Particle Mean-Field Theory

Before proceeding to a more careful treatment, it is instructive to first perform a mean-field analysis, as this can provide valuable insight into the problem. In the auxiliary particle framework, b represents the charge dynamics, while f describes the spin dynamics. Due to the constraint, b quantifies the deviation from a singly occupied impurity, making it a natural choice for a mean-field parameter. To start, it is necessary to construct the path integral, where the constraint given by Equation (2.8) is properly encoded. The partition function is restricted to the physical subsector as follows

$$Z_{Q=1} = \mathrm{tr}\left[e^{-\beta H} \delta_{Q-1} \right] = \int_{-i\pi/\beta}^{i\pi/\beta} \frac{d(i\beta\lambda)}{2\pi i} \,\mathrm{tr}\left[e^{-\beta H_\lambda} \right], \tag{2.10}$$

where $Z_{Q=1}$ is the physical partition function, and the integral representation of the delta function was used. The variable λ acts as a chemical potential. H_λ contains the infinite-U Hamiltonian given in Equation (2.9) with an additional term

$$H_\lambda = H + \lambda\,(Q-1) = H + \lambda \left(b^\dagger b + \sum_\sigma f^\dagger_\sigma f_\sigma - 1 \right). \tag{2.11}$$

Due to the local conservation of Q, the system exhibits a local $U(1)$ gauge symmetry. According to Elitzur's theorem [45], only gauge-invariant theories can have a non-zero saddle-point solution. The gauge degree of freedom can be absorbed into λ through the transformations

$$f_\sigma \to e^{i\phi(\tau)} f_\sigma, \quad b \to e^{i\phi(\tau)} b, \qquad \lambda \to \lambda(\tau) = \lambda - i\dot{\phi}(\tau), \tag{2.12}$$

effectively promoting λ to a dynamical field. This also modifies the associated action as

$$S \to S + i \int d\tau \dot{\phi}(\tau). \tag{2.13}$$

However, this does not introduce any modifications because the change in the phase is an integer multiple of 2π, resulting in an overall factor of $e^{2\pi n i} = 1$ in the path integral. Finally, the gauge-invariant partition function takes the form

$$\begin{aligned} Z = \int \mathcal{D}[c, f, b, \lambda] \exp\Bigg\{ \int d\tau \Bigg\{ & \sum_{k\sigma} c^\dagger_{k\sigma}(\tau) \left(\partial_\tau - \varepsilon_{k\sigma}\right) c_{k\sigma}(\tau) \\ & + \sum_\sigma f^\dagger_\sigma(\tau) \left(\partial_\tau - \varepsilon_d - \lambda(\tau)\right) f_\sigma(t) \\ & + b^\dagger(t) \left(\partial_\tau - \lambda(\tau)\right) b(t) \\ & - \sum_{k\sigma} \left(V c^\dagger_{k\sigma}(\tau) b^\dagger(\tau) f_\sigma(\tau) + h.c. \right) + \lambda(\tau) \Bigg\} \Bigg\}. \end{aligned} \tag{2.14}$$

Using the radial gauge [46] the phase can be chosen such that the mean field is given by

$$b(\tau) = b^*(\tau) = b \in \mathbb{R}, \qquad \lambda(\tau) = \lambda \in \mathbb{R}. \tag{2.15}$$

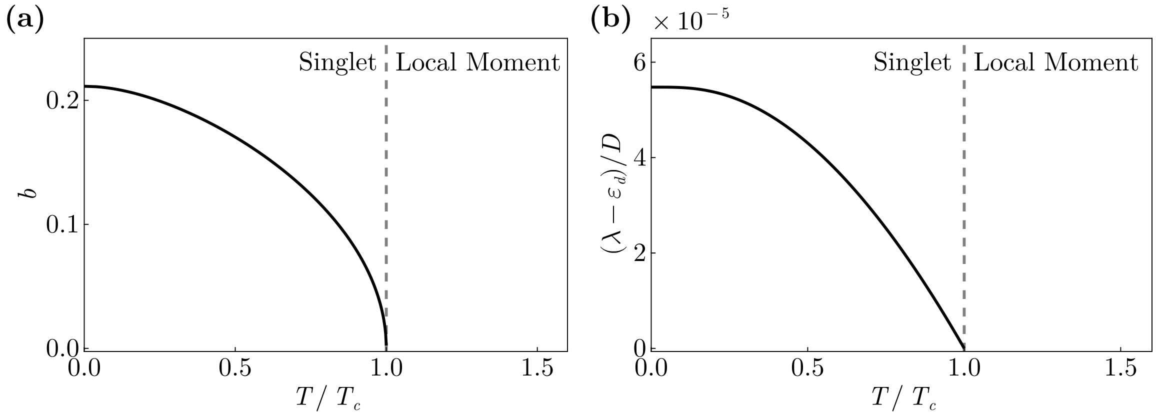

Figure 2.3: Self-consistent auxiliary particle mean-field solutions of Equations (2.21) and (2.22). **(a)** Temperature dependence of the bosonic field b, which remains 0 in the local moment regime and acquires a finite value at a critical temperature T_c, indicating a second-order phase transition from the local moment regime to the singlet formation. **(b)** Temperature dependence of the gauge field λ, which similarly remains zero in the local moment regime and becomes finite at T_c. The parameters used are $\varepsilon_d = -0.6D$ and $\Delta = 0.2D$, with a flat conduction density of states.

The partition function becomes[2]

$$Z = \int \mathcal{D}[c, f] \exp\{-S\}, \tag{2.16}$$

where the action is given by

$$S = \int d\tau \left\{ \lambda(b^2 - 1) + \sum_{k\sigma} \begin{pmatrix} c^\dagger_{k\sigma} & f^\dagger_\sigma \end{pmatrix} G^{-1}_{k\sigma}(\tau,\tau) \begin{pmatrix} c_{k\sigma} \\ f_\sigma \end{pmatrix} \right\}, \tag{2.17}$$

where

$$G^{-1}_{k\sigma}(\tau,\tau) = \partial_\tau \mathbb{1} - h = \begin{pmatrix} \partial_\tau - \varepsilon_{k\sigma} & -Vb \\ -Vb & \partial_\tau - \varepsilon_d - \lambda \end{pmatrix}. \tag{2.18}$$

It is now possible to integrate out c and f to obtain

$$S_{eff} = \mathrm{tr}\left\{\ln\left(-iG^{-1}_{k\sigma}(\tau,\tau)\right)\right\} + \beta\lambda(b^2 - 1). \tag{2.19}$$

The saddle-point equations are obtained by setting the first derivative of the effective action to zero

$$\frac{\delta S_{eff}}{\delta b} = 0 \quad \text{and} \quad \frac{\delta S_{eff}}{\delta \lambda} = 0. \tag{2.20}$$

This leads to the following saddle-point equations

$$\frac{\delta S_{eff}}{\delta b} = 2\beta\lambda b - \mathrm{tr}\left\{ G_{k\sigma} \frac{\delta G^{-1}_{k\sigma}}{\delta b} \right\} \Rightarrow 2\lambda b - 2\sum_{k\sigma} \left\langle f^\dagger_\sigma c_{k\sigma} \right\rangle = 0, \tag{2.21}$$

---

[2] For details on the change of measure, see example 17.3 in [47].

and

$$\frac{\delta S_{eff}}{\delta \lambda} = \beta(b^2 - 1) - \mathrm{tr}\left\{ G_{k\sigma} \frac{\delta G_{k\sigma}^{-1}}{\delta \lambda} \right\} \Rightarrow b^2 + \sum_{\sigma} \left\langle f_{\sigma}^{\dagger} f_{\sigma} \right\rangle = 1. \tag{2.22}$$

These equations form a set of relations that must be solved self-consistently. As indicated by Equation (2.22), the constraint is only enforced on average.

The temperature dependent solutions are presented in Figure 2.3. At low temperatures, there is a finite value for both b and λ indicating the Kondo regime, with a Kondo temperature given by $T_K \sim \lambda$ [14]. As the temperature increases, the values decrease and the mean-field theory predicts a second-order phase transition between local moments and singlet formation, in contrast to the expected crossover. This can be explained by the increase in thermal fluctuations which violate the constraint.

2.3 Non-Crossing Approximation

This section introduces a method that guarantees the enforcement of the local constraint. Similar to the previous section, the partition function must first be restricted to the physical subsector. Afterwards, the procedure for computing physical expectation values is developed. Furthermore, since the constraint commutes with the Hamiltonian, a conserving approximation is required to ensure that the conservation laws are maintained. By construction, this guarantees that all diagrams satisfy the constraint, preventing the occurrence of fluctuations that would violate it, as seen in the previous section. In later sections, this method will also be used in the discussion of heavy fermion systems.

2.3.1 Projection and Expectation Values

The partition function is restricted to the $Q = 1$ subsector via the introduction of a delta function, similar to Equation (2.10)

$$\begin{aligned} Z_{Q=1} &= \int \mathcal{D}[c, f, b]\, e^{-S} \delta(Q - 1) && (2.23) \\ &= \int_{-\pi}^{\pi} \frac{d\lambda}{2\pi} e^{i\lambda} Z_G(\lambda), && (2.24) \end{aligned}$$

where $Z_{Q=1}$ is the physical partition function and Z_G is the grand-canonical partition function. The term $i\lambda$ acts similar to a chemical potential, with the key difference being that, in this case, integration over all possible values of λ is required. Introducing the fugacity as $\zeta = e^{-i\lambda}$, the λ integral can be rewritten as an integral over the unit circle in the complex plane

$$Z_{Q=1} = -i \oint_{|\zeta|=1} \frac{d\zeta}{2\pi} \zeta^{-2} Z_G(\lambda(\zeta)) = \lim_{\zeta \to 0} \partial_\zeta Z_G(\lambda(\zeta)), \tag{2.25}$$

where, in the second equality, Cauchy's theorem for a second order pole is applied. Since the constraint Q commutes with the Hamiltonian, $Z_G(\lambda(\zeta))$ can be expressed as a sum over the canonical partition functions $Z_C(Q)$ for each Q subspace[3] as

$$Z_G(\lambda(\zeta)) = \sum_{Q=0}^{\infty} Z_C(Q) \zeta^Q. \tag{2.26}$$

---

[3] To maintain the intuition that $i\lambda$ acts as a chemical potential, a change of variables can be performed to express the limit in terms of λ as $\lim_{i\lambda \to \infty}$. This provides a physical interpretation that any subsector which is not $Q = 1$ is exponentially suppressed.

This allows the ζ derivative in Equation (2.25) to be evaluated, resulting in

$$Z_{Q=1} = \lim_{\zeta\to 0} \zeta^{-1} \langle Q\rangle_G \, Z_G(\lambda(\zeta)). \tag{2.27}$$

Now, the computation of the expectation value of an operator O in the physical subsector is developed. Following similar steps as before, the expectation value is given by

$$\begin{aligned} \langle O\rangle_C &= \frac{\mathrm{Tr}\left\{Oe^{-\beta H}\right\}_{Q=1}}{Z_{Q=1}} = \lim_{\zeta\to 0} \frac{\sum_{Q=0}^{\infty} \mathrm{Tr}\left\{Oe^{-\beta H}\right\}_Q Q\zeta^{Q-1}}{Z_{Q=1}} &(2.28)\\ &= \lim_{\zeta\to 0} \frac{\langle OQ\rangle_G \, Z_G(\lambda)\zeta^{-1}}{Z_{Q=1}} &(2.29)\\ &= \lim_{\zeta\to 0} \frac{\langle OQ\rangle_G}{\langle Q\rangle_G}. &(2.30)\end{aligned}$$

Here $\langle ...\rangle_C$ and $\langle ...\rangle_G$ denote the canonical and grand-canonical expectation values, respectively. In the last line, Equation (2.27) is used in a slightly rewritten form

$$\lim_{\zeta\to 0} \frac{Z_{Q=1}}{\langle Q\rangle_G} = \lim_{\zeta\to 0} Z_G(\lambda)\zeta^{-1}. \tag{2.31}$$

All physical operators of interest are bilinear in the auxiliary particle representation, meaning they annihilate the $Q = 0$ subspace. Consequently, for all intents and purposes, Equation (2.30) simplifies to

$$\langle O\rangle_C = \lim_{\zeta\to 0} \frac{\langle O\rangle_G}{\langle Q\rangle_G}. \tag{2.32}$$

To summarize, it has been shown that any physical operator in the physical subsector can be computed by projecting from the grand-canonical regime, where the constraint is not explicitly enforced, and Wick's theorem is applicable. Moreover, as will become evident in the subsequent sections, this projection simplifies certain expressions, making the analysis more manageable.

2.3.2 The Luttinger-Ward Functional and Self-Energies

The first order Luttinger-Ward diagram for the infinite-U single impurity Anderson model, is illustrated in Figure 2.4, and is given by

$$\Phi[G] = -V^2 \int_{\mathcal{C}} dt\, dt' \sum_{\sigma} G_{c_\sigma}(t,t') G_b(t,t') G_{f_\sigma}(t',t). \tag{2.33}$$

Due to the absence of crossing propagators, considering only these types of diagrams is typically called a non-crossing approximation (NCA).

In anticipation of the projection, it is useful to examine the ζ-scaling of the different types of Green functions introduced in Section 1.2. Let A represent a general auxiliary particle operator. The lesser Green function scales as

$$G^{<}(t,t') = i\left\langle A^{\dagger}(t')A(t)\right\rangle \sim \mathcal{O}(\zeta), \tag{2.34}$$

as it will annihilate the $Q = 0$ subspace. In contrast, the greater Green function scales as

$$G^{>}(t,t') = -i\left\langle A(t)A^{\dagger}(t')\right\rangle \sim \mathcal{O}(1), \tag{2.35}$$

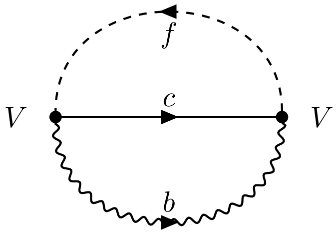

Figure 2.4: Luttinger-Ward functional for the single impurity Anderson model in auxiliary particle representation given in Equation (2.3). The solid line represents the conduction electron propagator, the dashed line represents the fermionic f propagator, and the wavy line represents the bosonic b propagator.

as it does not annihilate the $Q = 0$ subspace. Since quantities of order $\mathcal{O}(1)$ cannot depend on quantities of order $\mathcal{O}(\zeta)$, these two Green functions must decouple in some way when the projection is taken into account [48]. This decoupling reveals a delicate correspondence between auxiliary particle methods and non-equilibrium methods, where, in a similar spirit, the occupation information and the spectral information are decoupled. In principle, this does not pose any issues, and calculations can proceed without incorporating non-equilibrium techniques, see [49, 50]. However, as will become clear in the upcoming sections, tackling this problem using the non-equilibrium framework introduces simplifications, resulting in substantial numerical efficiencies.

Since the introduction of auxiliary particles makes the hybridization become the new interaction term, the conduction electrons now obtain a grand-canonical self-energy. This can be obtained via a functional derivative of the Luttinger-Ward functional, given by

$$\Sigma_{c_\sigma}(t,t') = -i\frac{\delta\Phi[G]}{\delta G_{c_\sigma}(t',t)} = iV^2 G_{f_\sigma}(t,t')G_b(t',t). \tag{2.36}$$

The right hand side contains two auxiliary particle propagators, meaning that the grand-canonical self-energy is at least of order $\mathcal{O}(\zeta)$, and therefore vanishes in the limit $\zeta \to 0$. As a result, the propagators of the conduction electrons, which since they are physical particles are of order $\mathcal{O}(1)$, can be treated as free propagators for all following diagrams. However, although the physical conduction electrons do not acquire a self-energy, they are still renormalized through the hybridization with the impurity. This is given by the T-matrix equation [51]

$$G_{c_\sigma} = G^0_{c_\sigma} + G^0_{c_\sigma} * T_\sigma * G^0_{c_\sigma}, \tag{2.37}$$

where $T_\sigma = V^2 G_{d_\sigma}$ and G_{d_σ} is the physical impurity Green function obtained from the self-consistent NCA loop, defined as

$$G_{d_\sigma}(t,t') = \lim_{\zeta\to 0}\frac{-i\left\langle \mathcal{T}_{\mathcal{C}} b(t)\, f^\dagger_\sigma(t) f_\sigma(t') b^\dagger(t')\right\rangle}{\langle Q\rangle} = \lim_{\zeta\to 0}\frac{iG_{f_\sigma}(t,t')G_b(t',t)}{\langle Q\rangle}. \tag{2.38}$$

The self-energies for the auxiliary particles, b and f, are also obtained from functional derivatives of the Luttinger-Ward functional and are given by

$$\Sigma_{f_\sigma}(t,t') = -i\frac{\delta\Phi[G]}{\delta G_{f_\sigma}(t',t)} = iV^2 G^0_{c_\sigma}(t,t')G_b(t,t'), \tag{2.39}$$

$$\Sigma_b(t,t') = i\frac{\delta\Phi[G]}{\delta G_b(t',t)} = -iV^2\sum_\sigma G_{f_\sigma}(t,t')G^0_{c_\sigma}(t',t). \tag{2.40}$$

To analyze their ζ scaling, the Langreth's rules are used to obtain the lesser and greater components, given by

$$\Sigma^{\lessgtr}_{f_\sigma}(t,t') = iV^2 G^{0\lessgtr}_{c_\sigma}(t,t') G^{\lessgtr}_{b}(t,t'), \tag{2.41}$$

$$\Sigma^{\lessgtr}_{b}(t,t') = -iV^2 \sum_{\sigma} G^{\lessgtr}_{f_\sigma}(t,t') G^{0\gtrless}_{c_\sigma}(t',t). \tag{2.42}$$

Since, the conduction electron Green functions scale as $\mathcal{O}(1)$, the scaling of the self-energies matches that of the corresponding auxiliary Green function, Equations (2.34) and (2.35). As a result, these self-energies must be taken into account in the grand-canonical calculations, and the auxiliary particles become renormalized in a self-consistent manner.

So far, the construction has been presented for the general non-equilibrium case, the continuation of which will be discussed separately in Chapter 4. The focus now shifts to the steady state, which is the primary setting in this thesis, with equilibrium included as a special case. Due to time translational invariance in the steady state, all Green functions and self-energies depend only on the relative time $\tau = t - t'$. Consequently, the d-electron Green function and the self-energies are now given by

$$G_{d_\sigma}(\tau) = \frac{iG_{f_\sigma}(\tau) G_b(-\tau)}{\langle Q \rangle}, \tag{2.43}$$

$$\Sigma^{\lessgtr}_{f_\sigma}(\tau) = iV^2 G^{0\lessgtr}_{c_\sigma}(\tau) G^{\lessgtr}_{b}(\tau), \tag{2.44}$$

$$\Sigma^{\lessgtr}_{b}(\tau) = -iV^2 \sum_{\sigma} G^{\lessgtr}_{f_\sigma}(\tau) G^{0\gtrless}_{c_\sigma}(-\tau). \tag{2.45}$$

To close the self-consistency loop, the next step is to compute the Green functions. A key advantage of the steady-state formulation is that all quantities can now be expressed in the frequency domain using Fourier transforms. This greatly simplifies the Dyson equation, as all the time integrals reduce to simple multiplication in frequency space. Additionally, due to the ζ-scaling of the lesser Green function, the projection provides a useful relation between the greater and the retarded Green functions, given by

$$G^R(\tau) = \theta(\tau)\left(G^>(\tau) - G^<(\tau)\right) \overset{\zeta\to 0}{\Rightarrow} G^R(\tau) = \theta(\tau) G^>(\tau). \tag{2.46}$$

Alternatively, the relation can also be written as

$$G^R(\tau) - G^A(\tau) = G^>(\tau) - G^<(\tau) \overset{\zeta\to 0}{\Rightarrow} 2i\,\mathrm{Im}\,G^R(\tau) = G^>(\tau). \tag{2.47}$$

Therefore, the Dyson Equation (1.58) for the retarded Green function can now be used

$$G^R_{b,f_\sigma}(\omega) = \left(\omega - \epsilon_{b,f} - \Sigma^R_{b,f_\sigma}(\omega)\right)^{-1}, \tag{2.48}$$

where $G^R_{b,f_\sigma}(\omega)$ and $\Sigma^R_{b,f_\sigma}(\omega)$ are the retarded Green function and self-energy respectively for f and b respectively, $\epsilon_f = \varepsilon_f$, and $\epsilon_b = 0$. The relations given in Equations (2.46) and (2.47) also apply to Σ^R and $\Sigma^>$. Finally, the lesser Green function can be related to the retarded and advanced Green function via Equation (1.74) as

$$G^<_{b,f_\sigma}(\omega) = G^R_{b,f_\sigma}(\omega) \Sigma^<_{b,f_\sigma}(\omega) G^A_{b,f_\sigma}(\omega). \tag{2.49}$$

Now, a complete set of self-consistent equations has been formulated, partially in time and partially in frequency space. These equations can be solved efficiently by performing numerical

Fourier transforms, see Chapter A, between the two bases as necessary.[4] Upon closer inspection of Equation (2.49) and the self-energies expressions given in Equations (2.44) and (2.45), it becomes clear that these equations are scale invariant. Meaning that a multiplication of both $G^<$ and $\Sigma^<$ by a constant would still satisfy these equations, which can lead to numerical instabilities. To address this, a normalization is introduced by dividing $G^<$ by Q, which is given by

$$Q = i \int \frac{d\omega}{2\pi} \left(G_b^<(\omega) - \sum_\sigma G_{f_\sigma}^<(\omega) \right) . \tag{2.50}$$

This normalization not only mitigates the scale invariance but also ensures that $Q = 1$, satisfying the physical constraint.

Self-Consistent NCA Loop

In principle, all the necessary tools are now available to construct the self-consistent loop. It is worth noting that the starting point of the sequence of steps in this iterative procedure is not important. However, the choice of the quantity used to monitor convergence can significantly impact numerical stability. Due to Kondo signatures, the Green functions tend to exhibit sharp features, making it challenging to converge to a fixed point. In contrast, the self-energies are generally smooth functions, making them the preferred choice for determining convergence. Therefore, the NCA loop is given by

0. Start with an initial guess for $\Sigma_{b/f}^{\lessgtr}(\tau)$.
1. Compute $\Sigma_{b/f}^R(\omega)$ using Equation (2.46) and then Fourier transforming.
2. Compute $G_{b/f}^R(\omega)$ using Equation (2.48).
3. Compute $G_{b/f}^>(\omega)$ using Equation (2.46).
4. Compute $G_{b/f}^<(\omega)$ using Equation (2.49) and divide by Q given in Equation (2.50).
5. Compute the updated expressions for $\Sigma_{b/f}^{\lessgtr}(\tau)$ by applying Fourier transforms and using Equations (2.44) and (2.45).
6. Repeat steps 1 through 5 until convergence is reached.

2.3.3 Results

The equilibrium spectral functions of the impurity and the local conduction electrons, computed from the self-consistent NCA loop and Equation (2.37), are presented in Figure 2.5. The impurity electron spectral function $A_d(\omega)$, shown in Figure 2.5a, exhibits the characteristic features of the infinite-U Anderson model. It displays a single particle peak at a renormalized energy level ε_d^* and a sharp Kondo resonance near $\omega = 0$. The renormalized local conduction electron spectral function $A_c(\omega)$, shown in Figure 2.5b, features a dip structure at the same positions

---

[4] The use of fast fourier transforms (FFTs) provides an extremely efficient method for performing these Fourier transformations. While standard FFTs require equidistant grids, an algorithm for computing Fourier transforms on exponential grids that utilizes FFTs has been developed during this thesis, demonstrated in Chapter A. The exponential grid is particularly well-suited for the Kondo problem, enabling accurate and efficient numerical calculations.

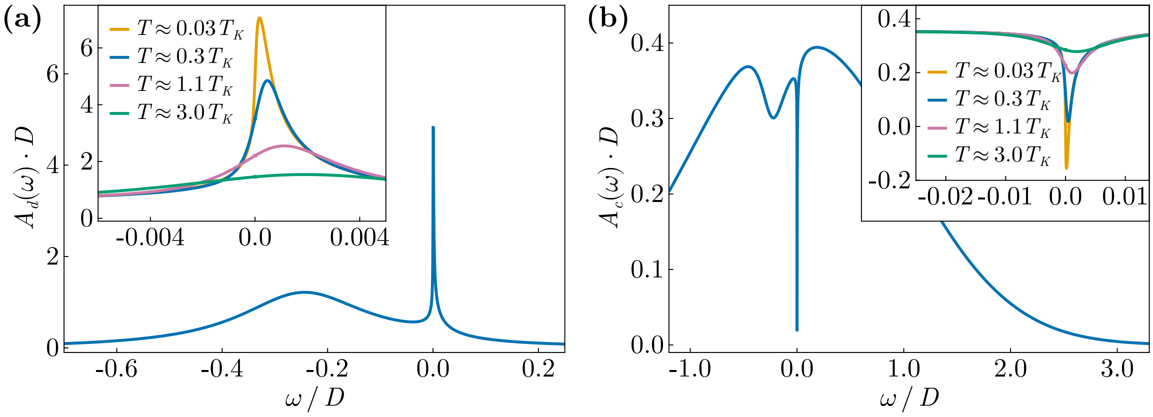

Figure 2.5: Spectral functions for the single impurity Anderson model obtained via NCA. **(a)** the d-electron spectral function shows the Kondo peak close to $\omega = 0$ and the single particle peak on the left. **(b)** The renormalized local conduction electron spectral function showing a dip structure at the same peak positions as $A_d(\omega)$. The parameters used are $\varepsilon_d = -0.25D$, $V = \sqrt{0.05}D$, leading to $T_K \approx 10^{-3}D$, where D is the standard deviation of the Gaussian free conduction electron density of states.

as the peaks in $A_d(\omega)$, reflecting the build-up of Kondo coherence. Since this construction corresponds to the infinite-U limit, the double occupancy peak is shifted to infinity, resulting in an impurity spectral function that is not normalized to 1. However, the normalization can be related to the single-particle occupancy through

$$\int d\omega A_{d_\sigma}(\omega) = 1 - n_{f_{-\sigma}}, \tag{2.51}$$

which holds to within 0.05% in the presented figures. As the temperature decreases, the Kondo peak becomes sharper, reflecting the enhanced coherence of the Kondo state. However, at temperatures an order of magnitude below the Kondo temperature, NCA begins to overestimate the height of the Kondo peak. This overestimation leads to a violation of the sum rule [52]

$$A_d(\omega = 0) = \frac{1}{\pi^2 V^2 A_c^0(0)}, \tag{2.52}$$

where $A_c^0(0)$ is the free conduction electron density of states. This results in an unphysical behavior in the spectral function of the local conduction electrons. This is illustrated in the inset in Figure 2.5b, where a negative spectral density emerges at low temperatures. From this point onward, the analysis is restricted to temperatures where this does not occur. For further details about the low-temperature behavior of NCA, the reader is referred to [14, 49].

Despite these limitations, NCA qualitatively captures the Kondo effect below the characteristic Kondo temperature and demonstrates qualitative agreement with exact results [53]. Additionally, the numerical implementation is simple, highly efficient, and capable of achieving a high degree of convergence even at low temperatures. NCA is also easily extendable to include crystal field excitations and more complex couplings, which can be challenging for exact methods. As a final, and perhaps most relevant remark, NCA provides a natural framework for tackling non-equilibrium Kondo problems, an area where exact methods have seen limited development.

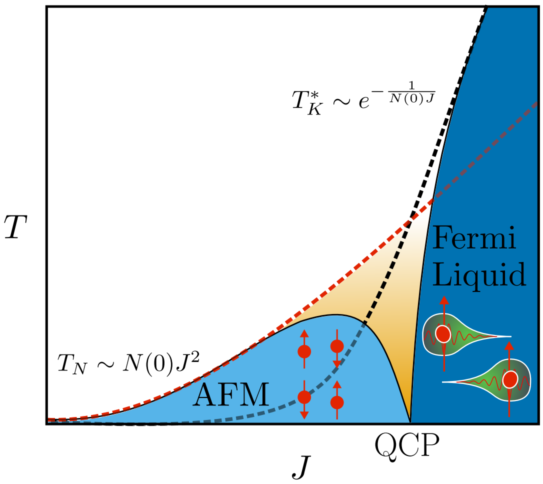

Figure 2.6: Doniach's phase diagram of heavy-fermion systems, illustrating the transition between the antiferromagnetic (AFM) phase and the heavy Fermi liquid phase, where the Kondo coupling J serves as the control parameter. The Néel temperature scales as $T_N \sim N(0)J^2$, where $N(0)$ is the density of states at the Fermi level, while the Kondo temperature scales as $T_K \sim e^{-\frac{1}{N(0)J}}$. At small J, T_K is exponentially small, allowing the AFM ordering to dominate. In contrast, at large J, the Kondo effect suppresses magnetic order, resulting in the formation of a heavy Fermi liquid. A quantum critical point (QCP), dominated by fluctuations, emerges when the two temperature scales become comparable, marking the boundary between the two regimes. The figure has been slightly modified from [47].

2.4 Heavy Fermion Systems

Until now, only the single-impurity problem has been discussed. While it already displays rich physics, in the context of this thesis it primarily serves as a foundation for understanding heavy-fermion systems. As the name suggests, heavy-fermion systems have quasiparticles with a large effective mass, which can be 100 to 1000 times larger than that of a free electron [47]. Typically, these materials feature a nearly half-filled f-shell, while the d-electrons constitute the conduction electrons. Due to the localized nature of the f-electrons, a flat band forms below the Fermi energy. In a sense, this can be viewed as a generalization of the single-impurity case, where instead of a single localized moment, each lattice site now hosts an impurity.[5] Despite the analogy, heavy fermion systems are far more complex than just a collection of single impurity problems. The presence of strong correlations and lattice coherence leads to more complicated many-body effects than observed in the single impurity case.

One of the most important effects in the lattice case is the competition between magnetic ordering and Kondo screening. This competition is captured by the Doniach phase diagram, shown in Figure 2.6, which compares the relevant energy scales associated with each scenario. On one hand, the conduction electrons can mediate a Ruderman-Kittel-Kasuya-Yosida (RKKY) interaction between the local magnetic moments, typically leading to an anti-ferromagnetic state below the Néel temperature T_N. On the other hand, the conduction electrons, via the Kondo effect, tend to screen the local magnetic moments, leading to the formation of a heavy fermion state. This occurs at a characteristic lattice Kondo temperature T_K^*. Notably, the

---

[5] Of course, referring to one of the main constituents of the system as an impurity seems uncalled for. However, to maintain a comparison to the single impurity Kondo effect, this, one might say, insulting language will be used throughout the thesis.

lattice Kondo temperature is typically larger than the single impurity Kondo temperature, $T_K^* > T_K$. This enhancement arises because both the conduction electrons and the delocalized impurity electrons contribute to screening of other local moments. This increases the effective local density of states experienced by each impurity site, leading to a higher Kondo temperature.

2.4.1 Auxiliary Particle Mean Field Theory

The Anderson lattice model (ALM) is a prototypical model used to describe heavy Fermion systems [54]. The Hamiltonian is given by

$$H_{\mathrm{ALM}} = -\sum_{i,j,\sigma} t^c_{ij} c^\dagger_{i\sigma} c_{j\sigma} + \varepsilon^d \sum_{i,\sigma} d^\dagger_{i\sigma} d_{i\sigma} + V \sum_{i,\sigma} \left(c^\dagger_{i\sigma} d_{i\sigma} + h.c. \right) + U \sum_i n^d_{i,\uparrow} n^d_{i,\downarrow}, \tag{2.53}$$

where $c^\dagger_{i\sigma}$ and $d^\dagger_{i\sigma}$ are the creation operators of the conduction and f-electrons, respectively. The hopping amplitudes is denoted by t^c_{ij} while ε_d denotes the energy level of the flat f-band, reflecting the localized nature of the f-electrons. The hybridization is given by V, and U denotes the on-site Coulomb repulsion.[6] To focus on the local moment regime, for which double occupancy of the f-electrons is forbidden and the infinite U-limit is justified, the f-electron operators are rewritten in terms of auxiliary particles

$$d_{i\sigma} = b^\dagger_i f_{i\sigma}, \qquad d^\dagger_{i\sigma} = f^\dagger_{i\sigma} b_i, \tag{2.54}$$

where $b^\dagger_i$ is a bosonic creation operator representing the empty state, and $f^\dagger_{i\sigma}$ is a fermionic creation operator representing the singly occupied state. Since the auxiliary particle representation is defined locally at each site i, and to ensure that each lattice site can host only one of these states, the following constraint is imposed

$$Q_i = b^\dagger_i b_i + \sum_\sigma f^\dagger_{i\sigma} f_{i\sigma} = 1. \tag{2.55}$$

By substituting the auxiliary particle operators into the Hamiltonian, the model becomes

$$\begin{aligned} H = &-\sum_{i,j,\sigma} t^c_{ij} c^\dagger_{i\sigma} c_{j\sigma} - \sum_{i,\sigma} \varepsilon_d f^\dagger_{i\sigma} b_i b^\dagger_j f_{j\sigma} + V \sum_{i,\sigma} \left(V c^\dagger_{i\sigma} b^\dagger_j f_{j\sigma} + h.c. \right) \\ &+ \sum_i \lambda_i \left(b^\dagger_i b_i + \sum_\sigma f^\dagger_{i\sigma} f_{i\sigma} - 1 \right). \end{aligned} \tag{2.56}$$

where the constraint field λ_i has been added to enforce the constraint, as in Section 2.2.2.

To gain qualitative insight into the system, it is instructive to perform a mean-field treatment, where the bosonic field b and the constraint field λ are treated as spatially uniform and static

$$b_i \to b, \qquad \lambda_i \to \lambda. \tag{2.57}$$

Assuming nearest-neighbor hopping for the conduction electrons, such that $t^c_{i,j} = t^c$ if i and j are neighboring sites and zero otherwise, the translational invariance of the system allows the Hamiltonian to be written in a diagonal form in k-space

$$H = \sum_{k\sigma} \begin{pmatrix} c^\dagger_{k\sigma} f^\dagger_{k\sigma} \end{pmatrix} \underbrace{\begin{pmatrix} \varepsilon_k & bV \\ bV & \varepsilon_d + \lambda \end{pmatrix}}_{h(k)} \begin{pmatrix} c_{k\sigma} \\ f_{k\sigma} \end{pmatrix}. \tag{2.58}$$

---

[6] The AFM Kondo coupling J used in Figure 2.6 can be related to these parameters using the Schrieffer-Wolff transformation, which gives $J = 2V^2 U / \left(\varepsilon_d \left(\varepsilon_d + U \right) \right)$ [41].

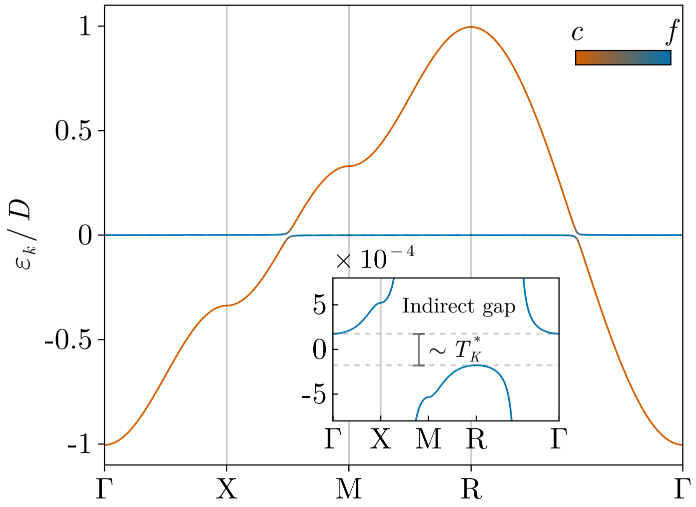

Figure 2.7: The eigenenergies of the Anderson lattice model, given in Equation (2.56), obtained using an auxiliary particle mean-field treatment at zero temperature. The density of states of the conduction electrons is taken to be cubic in 3 dimensions. The color gradient represents the $c-f$ character of the eigenstates. The parameters used are $\varepsilon_d = -0.25D$ and $V = \sqrt{0.02}D$ resulting in $b = 0.094$ and $\lambda = 0.0039D$, and leading to $T_K^* \approx 10^{-4}D$, where D is the bandwidth.

This allows for a straightforward computation of the eigenenergies, which yields

$$E_k^{\pm} = \frac{\varepsilon_k + \varepsilon_d + \lambda}{2} \pm \frac{1}{2}\sqrt{\left(\varepsilon_k - \varepsilon_d - \lambda\right)^2 + 4V^2b^2}. \tag{2.59}$$

The final mean-field equations are obtained in a similar way to how they were constructed in Section 2.2.2, resulting in

$$\lambda b - \sum_{k\sigma}\left\langle f_{k\sigma}^{\dagger} c_{k\sigma}\right\rangle = 0, \text{ and } \; b^2 + \sum_{\sigma}\left\langle f_{k\sigma}^{\dagger} f_{k\sigma}\right\rangle = 1. \tag{2.60}$$

The dispersion relation obtained by solving the self-consistent equations is shown in Figure 2.7. As anticipated from Equation (2.59), only two bands are present. Close to the Fermi energy, the bands flatten, and the density of states features a single peak, indicating the presence of heavy quasiparticles. This peak originally corresponds to the single-particle peak, near ε_d. However, due to the presence of λ, the band is shifted towards the Fermi energy, and its width is renormalized by the finite value of b, transforming this peak into the Kondo peak.

Since the indirect gap between the bands is proportional to the lattice Kondo temperature T_K^*, it can be extracted from the gap boundaries. The lower bound of the gap is given by

$$E_{k_D}^{-} = \frac{D + \varepsilon_d + \lambda}{2} - \frac{1}{2}\sqrt{\left(D - \varepsilon_d - \lambda\right)^2 + 4V^2b^2} \overset{\varepsilon_d + \lambda \ll D}{\approx} \varepsilon_d + \lambda - \frac{V^2b^2}{D}, \tag{2.61}$$

while the upper bound is given by

$$E_{k_{-D}}^{+} = \frac{-D + \varepsilon_d + \lambda}{2} + \frac{1}{2}\sqrt{\left(D + \varepsilon_d + \lambda\right)^2 + 4V^2b^2} \overset{\varepsilon_d + \lambda \ll D}{\approx} \varepsilon_d + \lambda + \frac{V^2b^2}{D}. \tag{2.62}$$

Thus, the lattice Kondo temperature is then given by

$$T_K \sim E_{k_{-D}}^{+} - E_{k_D}^{-} = \tfrac{2V^2b^2}{D} \sim N(0)V^2b^2. \tag{2.63}$$

This is in contrast to the single impurity case where the Kondo temperature is proportional to λ. Additionally, the Kondo weight can be determined since the height of the Kondo peak is inversely proportional to the hybridization width $\Gamma = \pi A_c(0)V^2$, see Equation (2.52), giving the Kondo weight to approximately be $W_K \sim T_K/\Gamma = b^2$.

Although the auxiliary particle mean field method qualitatively captures the formation of the heavy-band and the Kondo peak, it fails to account for the single-particle peak near ε_d which would remain. This limitation reduces its suitability for studying realistic materials. Furthermore, as before, this approach is restricted to zero temperature, necessitating a more detailed treatment of the problem.

2.5 Dynamical Mean Field Theory

Dynamical mean field theory (DMFT) has become one of the standard techniques used in the study of strongly correlated electrons. It has provided significant insights into phenomena such as metal-to-insulator transitions [55] and heavy fermion systems [56]. Moreover, its combination with density functional theory [57] has enabled quantitative ab-initio calculations, establishing it as a valuable tool in applied material science. The fundamental idea behind DMFT, is captured by the simple illustration given in Figure 2.8. Where a complex lattice problem with many interacting sites is mapped onto a single impurity problem coupled to a background field that represents the influence of the rest of the lattice. This is achieved at the cost of neglecting spatial correlations, meaning that the self-energy is assumed to be purely local. However, no assumptions are made regarding the dynamical components of the interaction, meaning that dynamical fluctuations are retained. This approximation works remarkably well for a wide range of strongly correlated materials, making DMFT a versatile tool.

While the single impurity problem itself is a nontrivial problem, it is far simpler to treat than the full lattice problem. Additionally, the assumptions made in DMFT allow for the lattice quantities to be renormalized using the results of the single impurity problem, which in turn updates the background field felt by the impurity, creating an iterative loop which can be solved self-consistently. For concreteness, the DMFT equations will only be derived for the Anderson lattice model, while the construction for the Hubbard model, along with a comprehensive review, can be found in [58]. After that, an alternative formulation of the DMFT equations for the Anderson lattice model will be presented. This approach reveals potential advantages for the construction of a DMFT formalism in the case when the system has a non-local hybridization.

2.5.1 Cavity Construction for the Anderson Lattice Model

One of the most standard way to derive the DMFT equations is the cavity construction procedure outlined in Figure 2.8. The procedure begins by separating the Anderson lattice Hamiltonian, given in Equation (2.53), into 3 parts $H_{ALM} = H^o + H^{mix} + H^{(o)}$, where

$$H^o = \varepsilon_d \sum_\sigma d^\dagger_{o\sigma} d_{o\sigma} + V \sum_\sigma \left(c^\dagger_{o\sigma} d_{o\sigma} + d^\dagger_{o\sigma} c_{o\sigma} \right) + U n^d_{o\uparrow} n^d_{o\downarrow}, \tag{2.64}$$

$$H^{mix} = - \sum_{i \neq o, \sigma} \left(t^c_{io}\, c^\dagger_{i\sigma} c_{o\sigma} + t^c_{oi}\, c^\dagger_{o\sigma} c_{i\sigma} \right), \tag{2.65}$$

$$H^{(o)} = - \sum_{(i,j) \neq o, \sigma} t^c_{ij} c^\dagger_{i\sigma} c_{j\sigma} + \varepsilon_d \sum_{i \neq o, \sigma} d^\dagger_{i\sigma} d_{i\sigma} + \sum_{i \neq o, \sigma} V \left(c^\dagger_{i\sigma} d_{i\sigma} + d^\dagger_{i\sigma} c_{i\sigma} \right) + \sum_{i \neq o} U n^d_{i\uparrow} n^d_{i\downarrow}. \tag{2.66}$$

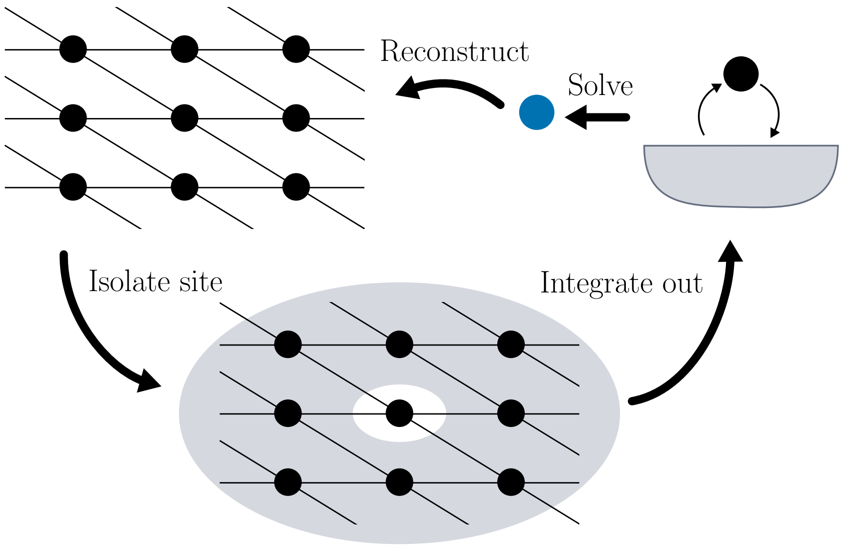

Figure 2.8: Illustration of the DMFT procedure. Starting with the lattice model, a single site is isolated, and its surrounding environment is integrated out, resulting in a single impurity problem embedded in a background field. The single impurity problem is then solved, and the lattice model is reconstructed by embedding the solved impurity onto every lattice site. This iterative process is repeated until convergence is reached.

Here, H^o describes the isolated site, which contains both a d-[7] and a conduction electron. H^{mix} represents the coupling between the isolated site and the rest of the system, governed by the conduction electron hopping terms. $H^{(o)}$ accounts for the remaining interacting lattice, excluding site o. With this decomposition, the partition function can then also be expressed as three parts

$$Z = \int \mathcal{D}[c^\dagger_{o\sigma}, c_{o\sigma}, d^\dagger_{o\sigma}, d_{o\sigma}]\, e^{-S^o} \int \prod_{i \neq o} \mathcal{D}[c^\dagger_{i\sigma}, c_{i\sigma}, d^\dagger_{i\sigma}, d_{i\sigma}]\, e^{-S^{(o)}} e^{-S^{mix}}, \tag{2.67}$$

where S^o, $S^{(o)}$ and S^{mix} are the actions corresponding to H^o,$H^{(o)}$ and H^{mix}, respectively.

The next step is to integrate out the degrees of freedom associated with the rest of the system. This is done by treating S^{mix} as a perturbative term and expanding the partition function as

$$\begin{aligned} Z = \int \mathcal{D}[c^\dagger_{o\sigma}, c_{o\sigma}, d^\dagger_{o\sigma}, d_{o\sigma}]\, e^{-S^o} Z^{(o)} \Bigg(1 - \int dt\ \left\langle \Delta S^{mix}(t) \right\rangle_{(o)} \\ + \frac{1}{2!} \int dt dt'\ \left\langle \Delta S^{mix}(t) \Delta S^{mix}(t') \right\rangle_{(o)} + ... \Bigg), \end{aligned} \tag{2.68}$$

where $\Delta S^{mix}(t) = \sum_{i \neq o} (t^c_{io}\, c^\dagger_{i\sigma} c_{o\sigma} + t^c_{oi}\, c^\dagger_{o\sigma} c_{i\sigma})$, $Z^{(o)}$ is the partition function of the remaining lattice, and $\langle ... \rangle_{(o)}$ corresponds to an expectation value with respect to $Z^{(o)}$. Up to this point, no approximations have been made. The first approximation is introduced here by truncating the cumulants to second order in t^c, which allows re-exponentiation while retaining only a quadratic term in the exponent. This approximation has important consequences. First, it

---

[7] This still corresponds to the f-electron discussed in the previous section. However, to distinguish it from the auxiliary particle f-operator, it will be referred to as a d-electron from now on.

removes spatial fluctuations of the interaction, resulting in a purely local self-energy such that $\Sigma_{i,j} = \delta_{i,j}\Sigma$.[8] Second, it implies that every lattice site is visited only once, meaning no closed loops can be formed on the lattice. Importantly, no approximations have been made on the dynamical effects of the interaction and thus remain preserved. The resulting effective action is equivalent to the action of the single impurity Anderson model, given by

$$\begin{aligned} S_{eff} = \int dt dt' \Bigg[&\sum_\sigma c^\dagger_{o\sigma}(t)\mathcal{G}_0^{c^{-1}}(t,t')c_{o\sigma}(t') + \sum_\sigma d^\dagger_{o\sigma}\left(i\partial_t + \varepsilon_d\right)d_{o\sigma} + Un^d_{o\uparrow}n^d_{o\downarrow} \\ &+ V\sum_\sigma \left(c^\dagger_{o\sigma}d_{o\sigma} + d^\dagger_{o\sigma}c_{o\sigma}\right)\Bigg], \end{aligned} \tag{2.69}$$

where the information regarding the surrounding lattice is encoded in the Weiss field $\mathcal{G}_0^{c^{-1}}(t,t')$ which is given by

$$\mathcal{G}_0^{c^{-1}}(t,t') = i\partial_t + \sum_{ij} t^c_{io}G^{c(o)}_{ij\sigma}(t,t')t^c_{oj}. \tag{2.70}$$

where $G^{c(o)}_{ij\sigma}(t,t')$ is the Green function for the conduction electrons in the lattice excluding site o, given by

$$G^{c(o)}_{ij\sigma}(t,t') = -\left\langle \mathcal{T}c_{i\sigma}(t)c^\dagger_{j\sigma}(t')\right\rangle_{(o)}. \tag{2.71}$$

To derive a relation for $G^{c(o)}_{ij\sigma}(t,t')$, it is instructive to treat the hopping to site o as a perturbation, and to restrict the analysis to the steady state. Then, with the DMFT assumptions

$$G^c_{ij} = G^{c(o)}_{ij} + \sum_{l,m} G^{c(o)}_{il}t^c_{lo}G^c_{loc}t_{om}G^{c(o)}_{mj} \tag{2.72}$$

$$= G^{c(o)}_{ij} + G^c_{i,0}G^{c^{-1}}_{loc}G^c_{0,j}, \tag{2.73}$$

where $G^c_{i,0} = \sum_l G^{c(o)}_{il}t^c_{lo}G^c_{loc}$. Now, all the required quantities can be computed using lattice Green functions, which is defined by

$$G_{ij} = \sum_k \frac{e^{ik(R_i - R_j)}}{\omega - \varepsilon_k - \Sigma(\omega)}. \tag{2.74}$$

Using this, and introducing $\zeta = \omega - \Sigma(\omega)$, the expression can be evaluated by going into k-space

$$\sum_{ij} t^c_{io}(G^c_{i,j} - G^c_{i,0}G^{c^{-1}}_{loc}G^c_{0,j})t^c_{oj} = \sum_k \frac{\varepsilon_k^2}{\zeta - \varepsilon_k} - \left(\sum_k \frac{\varepsilon_k}{\zeta - \varepsilon_k}\right)^2 \left(\sum_k \frac{1}{\zeta - \varepsilon_k}\right)^{-1} \tag{2.75}$$

$$= \zeta\left(-1 + \zeta\sum_k \frac{1}{\zeta - \varepsilon_k}\right) - \left(\left(\sum_k \frac{1}{\zeta - \varepsilon_k}\right)^{-1} - 2\zeta + \zeta^2\left(\sum_k \frac{1}{\zeta - \varepsilon_k}\right)\right) \tag{2.76}$$

$$= \zeta - G^{c^{-1}}_{loc}, \tag{2.77}$$

---

[8] This approximation becomes exact in the limit of infinite spatial dimensions, $d \to \infty$, which was the original motivation for the development of DMFT [58]. Since then, DMFT got a bad reputation for not being valid for lower dimensional systems, such as the 3D case considered here. However, DMFT provides excellent agreement with experimental observations when the most important effects from the interaction are local. For this reason, the discussion about spatial dimensions is omitted in this thesis.

where $\sum_k \varepsilon_k = 0$ was used. Therefore, substituting this into Equation (2.70) yields

$$\mathcal{G}_0^{-1}(\omega) = \Sigma(\omega) + G_{loc}^{-1}(\omega). \tag{2.78}$$

This equation could have almost been anticipated, because under the DMFT assumptions the local Green function of the lattice must coincide with the Green function of the solved impurity problem. This gives the equivalent relation

$$\mathcal{G} = \left(\mathcal{G}_0^{-1} - \Sigma\right)^{-1} \overset{\text{DMFT}}{=} G_{loc}. \tag{2.79}$$

To summarize, the original challenging many-body lattice problem has been mapped to an effective single impurity problem, where all the lattice effects are encoded in the Weiss field. This represents a significant simplification, as the single impurity problem is not only much better understood but also has a variety of well-established impurity solvers available, making it possible to compute the local self-energy efficiently.

The final step in the DMFT procedure is the reconstruction of the lattice Green function. Due to the two-band nature of the local model, this step is more intricate than usual. The local self-energy is given by

$$\Sigma(t,t') \overset{\text{DMFT}}{=} \begin{pmatrix} 0 & 0 \\ 0 & \Sigma_{loc}^{d}(t,t') \end{pmatrix}. \tag{2.80}$$

Which allows the lattice Green function to be expressed as

$$G_{lat}^{-1}(t,t',k) = \begin{pmatrix} (i\partial_t - \varepsilon_k)\,\delta(t-t') & V\delta(t-t') \\ V\delta(t-t') & (i\partial_t - \varepsilon_d)\,\delta(t-t') - \Sigma_{loc}^{d}(t,t') \end{pmatrix}. \tag{2.81}$$

At this point, all the relations necessary to construct a self-consistent loop are in place. However, the 2×2 structure of the lattice Green function would benefit from decomposing the DMFT equations into each component. Thus far, the formulation has been done in the Keldysh formalism. Since this thesis focuses on steady-state solutions, the analysis will now be restricted to the time-translationally invariant case. This restriction allows all quantities to be expressed in the Fourier basis, where G_{lat} is given by

$$G_{lat}(\omega,k) = \begin{pmatrix} G_{lat}^{c}(\omega,k) & G_{lat}^{cd}(\omega,k) \\ G_{lat}^{dc}(\omega,k) & G_{lat}^{d}(\omega,k) \end{pmatrix}. \tag{2.82}$$

For simplicity each component is evaluated separately. The diagonal components are given by

$$G_{lat}^{c}(\omega,k) = \left(\omega - \varepsilon_k - V\left(\omega - \varepsilon_d - \Sigma_{loc}^{d}(\omega)\right)^{-1} V\right)^{-1} \tag{2.83}$$

$$= \left(\omega - \varepsilon_k - V g^d V\right)^{-1}, \tag{2.84}$$

$$G_{lat}^{d}(\omega,k) = \left(\omega - \varepsilon_d - \Sigma_{loc}^{d}(\omega) - V\left(\omega - \varepsilon_k\right)^{-1} V\right)^{-1} \tag{2.85}$$

$$= \left({g^{d}}^{-1} - V\left(\omega - \varepsilon_k\right)^{-1} V\right)^{-1}, \tag{2.86}$$

where g^d is introduced as

$$g^d = \left(\omega - \varepsilon_d - \Sigma_{loc}^{d}(\omega)\right)^{-1}. \tag{2.87}$$

The off-diagonals components are given by

$$G^{cd}_{lat}(\omega,k) = -G^{c}_{lat}(\omega,k)Vg^{d} = (\omega-\varepsilon_k)^{-1}VG^{d}_{lat}(\omega,k), \tag{2.88}$$

$$G^{dc}_{lat}(\omega,k) = -g^{d}VG^{c}_{lat}(\omega,k) = G^{d}_{lat}(\omega,k)V(\omega-\varepsilon_k)^{-1}. \tag{2.89}$$

Now to obtain the local lattice Green function, the k-sum needs to be performed. Starting with the c component, which is given by

$$G^{c}_{loc}(\omega) = \sum_k G^{c}_{lat}(\omega,k) = \sum_k \left(\omega-\varepsilon_k - Vg^dV\right)^{-1}, \tag{2.90}$$

which can be evaluated as a density of states integral. Surprisingly, for the remaining terms, no additional k-sums are required. The d component is given by

$$G^{d}_{loc}(\omega) = \sum_k G^{d}_{lat}(\omega,k) = \sum_k \left(g^d + g^dV\left(\omega-\varepsilon_k - Vg^dV\right)^{-1}Vg^d\right) \tag{2.91}$$

$$= g^d + g^dVG^{c}_{loc}(\omega)Vg^d. \tag{2.92}$$

For the off diagonal terms the following expressions are obtained

$$G^{cd}_{loc}(\omega) = -G^{c}_{loc}(\omega)Vg^d, \tag{2.93}$$

$$G^{dc}_{loc}(\omega) = -g^dVG^{c}_{loc}(\omega). \tag{2.94}$$

The final step is to compute the inverse local Green function, defined as

$$G^{-1}_{loc}(\omega) = \begin{pmatrix} G^{-1,c}_{loc}(\omega) & G^{-1,cd}_{loc}(\omega) \\ G^{-1,dc}_{loc}(\omega) & G^{-1,d}_{loc}(\omega) \end{pmatrix}. \tag{2.95}$$

Once again, for simplicity, each component is evaluated separately. First the c component

$$G^{-1,c}_{loc}(\omega) = G^{c^{-1}}_{loc} + G^{c^{-1}}_{loc}G^{cd}_{loc}\left(G^{d}_{loc} - G^{dc}_{loc}G^{c^{-1}}_{loc}G^{cd}_{loc}\right)^{-1}G^{dc}_{loc}G^{c^{-1}}_{loc} \tag{2.96}$$

$$= G^{c^{-1}}_{loc} + Vg^dV, \tag{2.97}$$

and the d component

$$G^{-1,d}_{loc}(\omega) = \left(G^{d}_{loc} - G^{dc}_{loc}G^{c^{-1}}_{loc}G^{cd}_{loc}\right)^{-1} \tag{2.98}$$

$$= \left(G^{d}_{loc} - g^dVG^{c}_{loc}Vg^d\right)^{-1} = g^{d^{-1}}. \tag{2.99}$$

The off diagonals terms are given by

$$G^{-1,cd}_{loc}(\omega) = -G^{c^{-1}}_{loc}G^{cd}_{loc}G^{-1,d}_{loc}(\omega) = V, \tag{2.100}$$

$$G^{-1,dc}_{loc}(\omega) = -G^{-1,d}_{loc}(\omega)G^{dc}_{loc}G^{c^{-1}}_{loc} = V. \tag{2.101}$$

Combining all of the above relations together, the Weiss field can be expressed as

$$\mathcal{G}^{-1}_{0} = \begin{pmatrix} G^{c^{-1}}_{loc} + Vg^dV & V \\ V & g^{d^{-1}}_{0} \end{pmatrix}, \tag{2.102}$$

where $g^d_0 = (\omega-\varepsilon_d)^{-1}$. As expected, since only the conduction electrons can hop into the bath, they are the only ones that acquire a background Weiss field. In contrast, the d-electrons feel the bath indirectly through the hybridization with the local conduction electrons. Similarly, as seen in Equation (2.80), the interaction only affects the d- electrons directly, while the conduction electrons feel the interaction only through their hybridization with the local d-electrons.

Self-Consistent DMFT Loop

To summarize all the above steps, the self-consistent DMFT loop for the Anderson lattice model can be constructed in the following way

0. Start with an initial guess for the self-energy Σ^d and compute Vg^dV via Equation (2.87).
1. Compute the local lattice Green functions G^c_{loc} and G^d_{loc} using Equations (2.90) and (2.92).
2. Compute the conduction electron component of the Weiss function $\mathcal{G}^c_0$ using Equation (2.102).
3. Solve the impurity problem to obtain a new guess for Σ^d and compute Vg^dV.
4. Repeat steps 1 through 3 until convergence is reached.

NCA as an Impurity Solver for DMFT

Since NCA is also constructed as a self-consistency loop, its integration as an impurity solver in the DMFT is straightforward, as both loops can be combined into a single large loop and solved simultaneously. This approach not only simplifies the implementation but also generally enhances numerical stability and accelerates convergence. As an impurity solver, NCA provides the T-matrix $\mathcal{G}^d$ as a solution, so some additional manipulations are required for compatibility with the DMFT loop. If $\mathcal{G}^d$ is known, then using Equations (2.79) and (2.102), g^d can be directly obtained as

$$\mathcal{G}^d = \left(g^{d^{-1}} - V\mathcal{G}^c_0 V\right)^{-1} \Rightarrow g^d = \left(\mathcal{G}^{d^{-1}} + V\mathcal{G}^c_0 V\right)^{-1}, \tag{2.103}$$

where $\mathcal{G}^c_0 = \left(G^{c^{-1}}_{loc} + Vg^dV\right)^{-1}$. Thus, removing the need to explicitly compute Σ^d in the DMFT loop.

2.5.2 Cavity Construction via the Hybridization

The way that the impurity is isolated in the Anderson lattice Hamiltonian is not unique. This flexibility allows for the possibility of alternative DMFT constructions, which would lead to different equations that might be better suited for specific problems. Starting once again with the Anderson lattice Hamiltonian, the Hamiltonian is split into three parts as before, $H_{ALM} = H^o + H^{mix} + H^{(o)}$, but this time it is isolated via the hybridization as

$$H^o = \varepsilon_d \sum_\sigma d^\dagger_{o\sigma} d_{o\sigma} + U n^d_{o\uparrow} n^d_{o\downarrow}, \tag{2.104}$$

$$H^{mix} = \sum_{i\neq o,\sigma} \left(V_{i,o} c^\dagger_{i\sigma} d_{o\sigma} + V_{o,i} d^\dagger_{o\sigma} c_{i\sigma}\right), \tag{2.105}$$

$$H^{(o)} = -\sum_{(i,j)\neq o,\sigma} t^c_{ij} c^\dagger_{i\sigma} c_{j\sigma} + \varepsilon_d \sum_{i\neq o,\sigma} d^\dagger_{i\sigma} d_{i\sigma} + \sum_{i\neq o,\sigma} \left(V_{i,j}\, c^\dagger_{i\sigma} d_{j\sigma} + V_{ij}\, d^\dagger_{i\sigma} c_{j\sigma}\right) + \sum_{i\neq o} U n^d_{i\uparrow} n^d_{i\downarrow}, \tag{2.106}$$

where a non-local hybridization was used. Following the same steps as in the previous construction, the remaining sites are integrated out and then the effective action is obtained to be

$$S_{eff} = \int dt dt' \left[\sum_\sigma d^\dagger_{o\sigma}(t)\, \mathcal{G}^{-1}_0(t,t') d_{o\sigma}(t') + U n^d_{o\uparrow} n^d_{o\downarrow}\right], \tag{2.107}$$

where this time

$$\mathcal{G}_0^{-1}(t,t') = i\partial_t - \varepsilon_d - \sum_{i,j} V_{i,o}\tilde{G}^c_{ij\sigma}(t,t')V_{o,j}, \tag{2.108}$$

where

$$\tilde{G}^c = -\left\langle \mathcal{T} c_{i\sigma}(t) c^\dagger_{j\sigma}(t') \right\rangle_{(o)} \tag{2.109}$$

is the conduction electron Green function where the hybridization to site o is removed. This effective action is also equivalent to the effective action of the single impurity Anderson model, up to a Hubbard-Stratonovich transformation.

To compute $\tilde{G}^c$, the T-matrix equation is used to reintroduce the hybridization to site o to all orders

$$G^c_{ij} = \tilde{G}^c_{ij} + \sum_{l,m} \tilde{G}^c_{il} V_{l,o} G^d_{oo} V_{o,m} \tilde{G}^c_{mj}, \tag{2.110}$$

where it can be seen that G^d is the local T-matrix, that is obtained within NCA. It is more convenient to straight away compute the full local hybridization function $\Delta = \sum_{i,j} V_{i,o} G^c_{ij\sigma} V_{o,j}$, which can be computed on the lattice as

$$\Delta = \tilde{\Delta} + \tilde{\Delta} G^d_{oo} \tilde{\Delta} \;\Rightarrow\; \tilde{\Delta} = \Delta \left(1 + \Delta g^d\right)^{-1}, \tag{2.111}$$

where $g^d = \left(G^{d,-1}_{oo} + \tilde{\Delta}\right)^{-1}$. To compare with the approach in the previous section, the hybridization is set to be local, $V_{i,j} = V\delta_{i,j}$, and then a direct comparison shows that the two approaches are equivalent. This equivalence is reassuring, as it demonstrates that the results obtained for the same local hybridization scenario are consistent with the standard approach. Additionally, this method naturally allows for a non-local hybridization, which is challenging to implement in the standard approach. This makes this approach particularly valuable for studying systems where a non-local hybridization plays a crucial role, like in topological Kondo insulators and Weyl Kondo semi-metals.

2.5.3 Results

A significant simplification occurs when the free conduction electron density of states is chosen to be semicircular[9]

$$A^0_c(\omega) = \frac{2}{\pi D^2}\sqrt{D^2 - \omega^2}\,\Theta(|\omega| - D), \tag{2.112}$$

where D is the bandwidth. In this case, a simpler expression that relates the local Green function and the Weiss field holds

$$\mathcal{G}_0^{-1}(\omega) = \omega - \frac{D^2}{4} G_{loc}(\omega). \tag{2.113}$$

This relation eliminates the need for a k-sum entirely, resulting in a substantial numerical speed-up. The equilibrium local spectral functions of the d- and conduction electrons, computed from the self-consistent DMFT loop at a temperature below the Kondo lattice temperature, are

---

[9] This density of states naturally arises when the problem is formulated on a Bethe lattice in the limit where the coordination number $z \to \infty$. In this case, the DMFT approximations become exact.

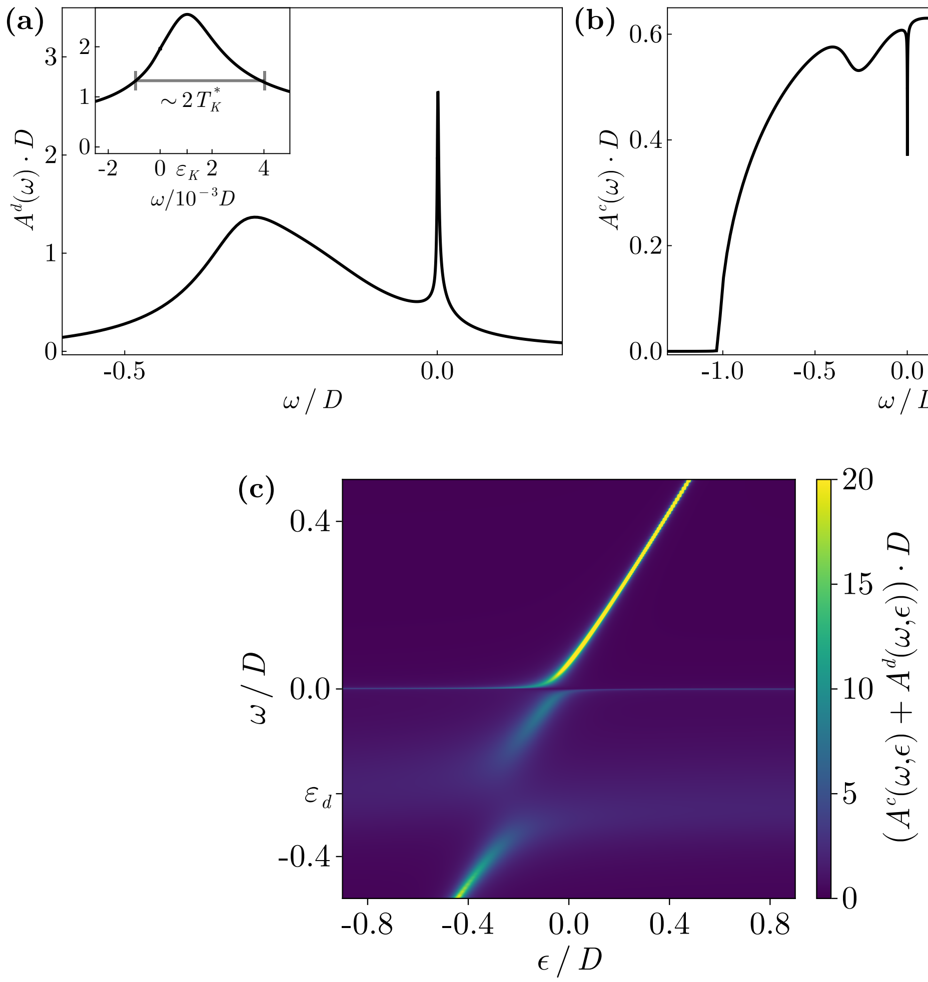

Figure 2.9: Spectral functions for the Anderson lattice model obtained from DMFT. **(a)** The local spectral function of the d-electrons displays a sharp Kondo peak. The inset demonstrates how the lattice Kondo temperature T_K^* is extracted. **(b)** The local conduction electron spectral function displays a characteristic Kondo dip near the Fermi level. **(c)** The trace of the lattice spectral function, where the interaction induced heavy band close to the Fermi level is visible. The lower values in the color gradient correspond to a d-character of the eigenstate, while higher values indicate a stronger c-character. The parameters used are $\beta = 1000/D$, $\varepsilon_d = -0.25D$, $V = \sqrt{0.027}D$ leading to a lattice Kondo temperature $T_K^* \approx 2\cdot 10^{-3}D$. The density of states of the conduction electrons was taken to be semi-circular, with the bandwidth D being taken as the unit.

shown in Figure 2.9a and 2.9b. In the local impurity spectral function, two distinct peaks are visible. The first broad peak located near ε_d corresponds to the single-particle excitation peak, and the second narrow peak near the Fermi level corresponds to the Kondo resonance peak. This two-peak structure is expected from the infinite U Anderson model. This is because, the third peak associated with double occupancy is shifted to infinity and is therefore not visible. As a result, the spectral function of the d-electrons is no longer normalized to one. However, the conduction electron spectral function still remains properly normalized. The lattice Kondo temperature T_K^* is not easily extracted from the model parameters, but it can be evaluated from the width of the Kondo peak, as shown in the inset of Figure 2.9a.

In the single impurity case, the Kondo peak corresponds to the screening of an isolated spin. In the lattice case the Kondo peak corresponds to the emergence of a coherent flat band, reflecting that the associated quasiparticles have a very large effective mass. This is clearly visible in the momentum-resolved lattice spectral function, shown in Figure 2.9c, where a heavy flat band forms around the Fermi level. This is accompanied by a depletion of spectral weight in the conduction electron density of states, reflecting the formation of the heavy quasiparticles. The presence of the single-particle peak highlights an improvement over the auxiliary particle mean-field approach, as the DMFT solution not only captures the Kondo physics but also retains the single-particle excitations. A rough comparison of the color scale of Figure 2.7 and Figure 2.9c shows good agreement and that the flat band has predominantly *d*-character.

2.6 Entanglement Entropy with Auxiliary Particles

One of the fundamental thermodynamic properties that can be readily measured experimentally is specific heat. However, theoretical calculations of the specific heat, especially within the framework of quantum field theory, can be quite challenging. This section demonstrates a neat approach that allows an easy computation of the entanglement entropy using auxiliary particles. The auxiliary particle creation operator, $A_m^\dagger$, is introduced such that it generates the state of interest with quantum number m from the vacuum. The reduced density matrix emerges when computing the projected lesser Green function at $\tau = 0$, given by

$$\lim_{\zeta\to 0} \frac{G_m^<(\tau=0)}{\langle Q\rangle} = \lim_{\zeta\to 0} \frac{i\,\mathrm{Tr}\left(\zeta^Q \rho A_m^\dagger A_m\right)}{\langle Q\rangle} = \lim_{\zeta\to 0} \frac{i\,\mathrm{Tr}\left(A_m \rho A_m^\dagger\right)_{Q=0}}{\langle Q\rangle} = i\rho_m^{Q=1}, \tag{2.114}$$

where $\rho_m^{Q=1}$ is the reduced density matrix. In the Anderson lattice model, given in Equation (2.53), $G_m^<(\tau=0)$ is a diagonal matrix, where each entry corresponds to the particle number of the corresponding auxiliary particle number n_m. This results in the reduced density matrix to be given by $\rho_m^{Q=1} = n_m$. With the knowledge of the reduced density matrix, the entanglement entropy can be extracted as

$$S = -\,\mathrm{Tr}(\rho \ln \rho) = -\sum_m n_m \ln n_m. \tag{2.115}$$

From the entanglement entropy, a specific heat analogue can be computed by taking a numerical derivative with respect to the temperature $C = \partial S/\partial T$. This requires only a single numerical derivative, making it significantly more efficient than earlier approaches that needed to compute a second derivative numerically [59].

As shown in Figure 2.10a, these quantities display several intriguing features. At high temperature, C increases as the temperature decreases, reaching a peak after which it starts to decrease. This behavior corresponds to the well-known Schottky anomaly [31], typically observed in two-level systems. In which a peak occurs in C at $T \sim 0.417\Delta$, where Δ is the energy difference between the two levels. At high temperatures, where the Kondo effect is not present, the model effectively reduces to a resonant level model and thus follows this behavior. Therefore, in this case, Δ corresponds to the renormalized single-particle energy ε_d^*. As the temperature approaches the lattice Kondo temperature T_K^*, C turns negative at a certain temperature. Notably, this coincides with the formation of a small Kondo peak in the spectral function, marking the onset of the Kondo effect. At this temperature, the localized impurity electrons become mobile and begin to contribute to the screening of other impurity sites, leading to an increase in entropy, and thus the negative C appears. At even lower temperatures, going down to the lowest temperature at which DMFT converges, the specific heat appears to plateau.

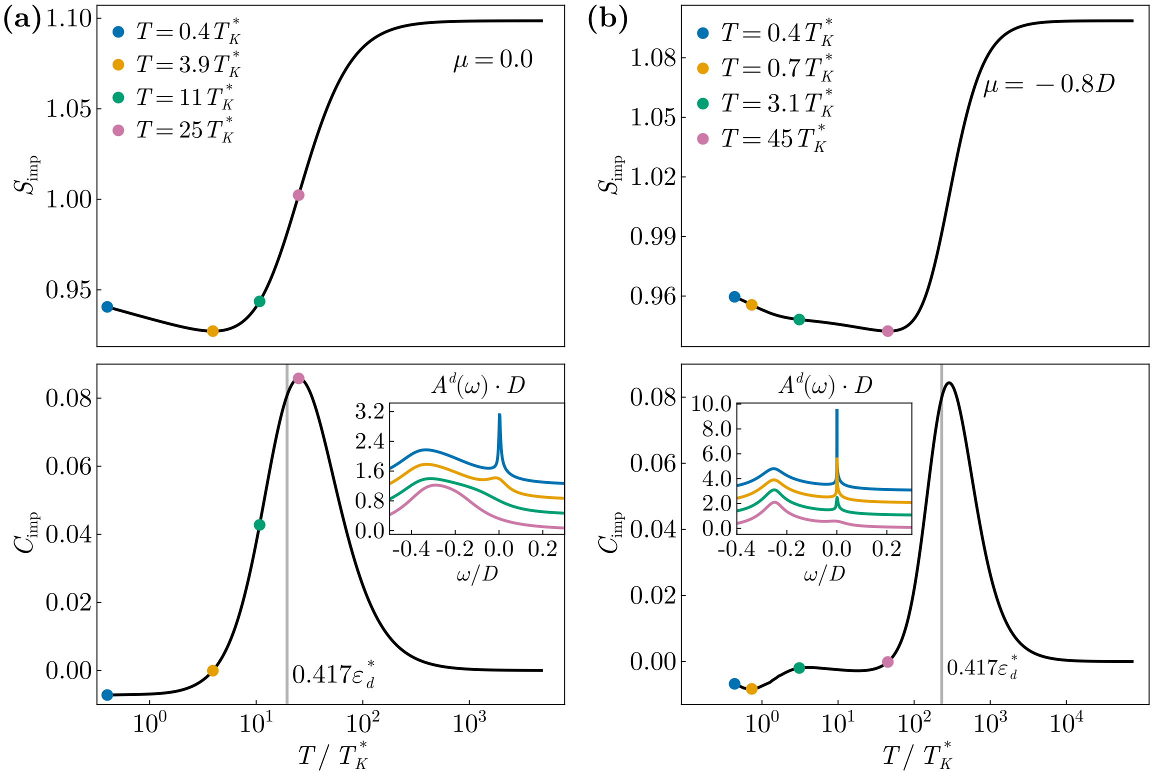

Figure 2.10: The entanglement entropy, computed from Equation (2.115), and the specific heat analogue for the Anderson lattice model, for two different chemical potentials, where a Gaussian density of states for the conduction electrons was taken. The gray line indicates the peak of the Schottky anomaly, occurring at $T \sim 0.417\varepsilon_d^*$. The point at which the specific heat becomes negative marks the onset of the Kondo effect. The insets show the impurity spectral function at the corresponding temperatures. The parameters used for all plots are $\varepsilon_d = -0.3D$, and $V^2 = 0.06D^2$ which results in a lattice Kondo temperature of $T_K^* \approx 7 \cdot 10^{-3}D$ in **(a)** $\mu = 0.0$ and $T_K^* \approx 4 \cdot 10^{-4}D$ in **(b)** $\mu = -0.8D$.

When the conduction electron filling is low, the lattice Kondo temperature T_K^* may become smaller than the single impurity Kondo temperature T_K. This can be explained by the low number of conduction electrons limiting the effective screening of all impurity sites. As a result, only a subset of impurities get screened initially, resulting in multiple single-impurity Kondo resonances. As the temperature decreases further, additional impurity electrons become mobile, progressively screening the remaining impurities. Ultimately, this leads to the formation of a heavy fermion state, albeit with $T_K^* < T_K$. This scenario is depicted in Figure 2.10b. where the specific heat first becomes negative nearly two orders of magnitude above T_K^*, marking the onset of the single impurity Kondo effect. When the temperature gets closer to T_K^* a second dip is observed, marking the transition to the lattice Kondo regime.

Chapter 3

Periodically Driven Heavy-Fermion Systems

In recent years, the study of periodically driven systems, commonly known as Floquet systems, has attracted significant attention [60, 61]. Due to the continuous periodic driving, Floquet states are inherently non-equilibrium and remain in a highly excited, non-thermal steady state, making them among the most pronounced examples of non-equilibrium systems. It has been demonstrated that time-periodic fields can induce new states of matter such as topological states [62, 63], time crystals [1], and other exotic phenomena [4, 5] that have no static analogs. This approach has gained widespread popularity due to the precise control it offers over quantum systems, to the extent that terms such as ”Floquet engineering” have become commonplace in the field [60, 61].

As demonstrated in Chapter 2, strongly correlated systems already exhibit intriguing and rich physics in equilibrium. Extending the study of these systems to non-equilibrium conditions opens new directions for exploring correlated systems where effects such as light-induced superconductivity [64, 65] and other emergent properties [66, 67] have been observed. Additionally, non-equilibrium effects have facilitated the development of novel measurement techniques that provide access to equilibrium properties that would otherwise be difficult to access [68, 69].

This chapter focuses on the effects of light irradiation on heavy-fermion systems. A typical model for such systems is the Anderson lattice model, where strongly repulsive, localized electrons in the $4f$-shell of rare-earth ions hybridize with a sea of conduction electrons. The Kondo effect induces a new flat band of heavy fermions near the Fermi energy. Due to dipole selection rules, applying a stationary light field induces a time-periodic hybridization between the conduction and the $4f$-electrons. On one hand, the Floquet theorem predicts that the periodic driving produces replicas of the Kondo resonance, centered around integer multiples of the driving frequency. On the other hand, when the driving frequency is comparable to the characteristic energy scales of the system, it can interfere with the formation of Kondo singlets, potentially leading to the destruction of the heavy-fermion state altogether.

In many previous studies, Floquet systems have been analyzed using the high-frequency Magnus expansion [70]. However, such methods are not applicable here, as they rely on a clear separation of time scales, which is absent when the driving frequency is comparable to the relevant energy scales of the system. Instead, the non-equilibrium quantum field theory techniques developed in Chapter 1, which do not impose any restrictions on the driving frequency, will be extended to the Floquet framework [8, 71, 72].

3.1 Floquet Theorem

The Floquet theorem provides a systematic approach for solving ordinary differential equations where the involved functions are periodic in time. This makes it widely applicable across many areas of physics. In the following, the focus is restricted to its application in quantum systems, where the dynamics are captured by the time dependent Schrödinger equation,

$$i\dot{\Phi}(t) = H(t)\Phi(t), \tag{3.1}$$

where $\Phi(t)$ is the state vector of the system, and $H(t)$ is the time-dependent Hamiltonian. To apply the Floquet theorem, the Hamiltonian is assumed to be periodic in time, $H(t+T) = H(t)$, with a period of T. The Floquet theorem[1] states that the solution of Equation (3.1) can be written in the form

$$\Phi_\alpha(t) = e^{-i\varepsilon_\alpha t} u_\alpha(t), \tag{3.2}$$

where ε_α are the Floquet quasi-energies [75], and $u_\alpha(t)$ is a periodic function with the same period T as the Hamiltonian, $u_\alpha(t+T) = u_\alpha(t)$. Since $u_\alpha(t)$ is periodic, it can be expanded in a discrete Fourier series as

$$u_\alpha(t) = \sum_m e^{-im\Omega t} u_\alpha^n, \tag{3.3}$$

where $\Omega = 2\pi/T$ is the driving frequency, and u_α^m represents the mth Floquet mode of the Floquet state. Substituting this expansion into Equation (3.1) and taking a Fourier transform yields

$$\sum_m (\varepsilon_\alpha + m\Omega)\, e^{-i(\varepsilon_\alpha + m\Omega)t} u_\alpha^m = \sum_{mn} e^{-im\Omega t} H_m e^{-i(\varepsilon_\alpha + n\Omega t)} u_\alpha^n, \tag{3.4}$$

where H_m is the Fourier component of the Hamiltonian, given by $H_m = \frac{1}{T}\int_{-T/2}^{T/2} dt H(t) e^{im\Omega t}$. Shifting $m \to m - n$ on the right hand side and defining the Floquet matrix form of the Hamiltonian as $H_{mn} = H_{m-n}$, the above equation can be rewritten as

$$\sum_n (H_{mn} - m\Omega\delta_{m,n})\, u_\alpha^n = \varepsilon_\alpha u_\alpha^m. \tag{3.5}$$

This result demonstrates a major simplification of the original differential equation. Instead of explicitly time-evolving the state with complex non-equilibrium dynamics, the problem reduces to solving a steady-state algebraic equation. An immediate consequence is that this formulation introduces an infinite number of Floquet modes that must be accounted for, making the equation appear less tractable. However, for practical applications, the Floquet modes can be truncated to a finite n_{max} (typically $n_{max} \sim 1/\Omega$), allowing for a straightforward numerical solution. It follows from Equation (3.5) that the quasienergy is conserved only up to integer multiples of the driving frequency Ω. As a result, the spectral function acquires additional poles at shifted energies $\varepsilon + n\Omega$ where $n \in \mathbb{N}$. These poles represent the emergence of Floquet sidebands, which correspond to processes where the system absorbs or emits quanta of the driving field.

---

[1] A proof of the theorem can be found in [73] and will not be covered here. One of the first applications of the Floquet theorem in a physics setting appears in [74].

Typically, it is useful to define a Floquet Hamiltonian as $\mathcal{H}_{mn} = H_{mn} - m\Omega\delta_{m,n}$, which in matrix form takes the structure

$$\mathcal{H} = \begin{pmatrix} \ddots & & & & & & \iddots \\ & H_0 + 2\Omega & H_1 & H_2 & H_3 & H_4 & \\ & H_{-1} & H_0 + \Omega & H_1 & H_2 & H_3 & \\ \cdots & H_{-2} & H_{-1} & H_0 & H_1 & H_2 & \cdots \\ & H_{-3} & H_{-2} & H_{-1} & H_0 - \Omega & H_1 & \\ & H_{-4} & H_{-3} & H_{-2} & H_{-1} & H_0 - 2\Omega & \\ \iddots & & & & & & \ddots \end{pmatrix} \tag{3.6}$$

Each element of the Floquet matrix H_{mn} corresponds to the probability amplitude of the transition from the mth Floquet mode to the nth one. The off-diagonal components represent excitations induced by the external driving field, while the diagonal components correspond to the probability of remaining in the same mode [71]. In the case of monochromatic driving, where the time dependence of the Hamiltonian is given by a single frequency component. In this case, only $H_{\pm 1}$ remain, and the Floquet Hamiltonian simplifies to a tridiagonal form, which is equivalent to a tight-binding model in quasienergy space rather than real space[2].

3.1.1 Periodically Driven Two-Level System

To illustrate the key ideas of Floquet systems, an example of a two-level atom coupled to a single photon mode is considered. The system is described by the Hamiltonian

$$H = \Omega a^\dagger a + g\left(\vec{e}\, a + \vec{e}^{\,*} a^\dagger\right) \cdot \vec{\sigma} + \Delta\sigma^z, \tag{3.7}$$

where $\vec{e}$ is the polarization vector of the light, and $\vec{\sigma}$ is a vector of Pauli matrices representing the atomic degrees of freedom. The coupling strength is given by g, and Δ represents the energy splitting of the two-level system. To explore the role of periodic driving, two specific polarization cases are considered, circularly polarized light with $\vec{e} = (1/\sqrt{2}, i/\sqrt{2}, 0)$ and linearly polarized light with $\vec{e} = (1, 0, 0)$. In the semi-classical limit, which is valid in the large photon number regime, the photon operator is replaced by its expectation value $a(t) \to \langle a \rangle e^{-i\Omega t} = \psi e^{i\varphi - i\Omega t}$, where ψ and φ are the condensate amplitude and phase respectively. Using this the Hamiltonians simplify, up to a constant term, to

$$H_{\mathrm{CP}} = A\cos(\Omega t - \varphi)\sigma^x + A\sin(\Omega t - \varphi)\sigma^y + \Delta\sigma^z, \tag{3.8}$$
$$H_{\mathrm{LP}} = A\cos(\Omega t - \varphi)\sigma^x + \Delta\sigma^z, \tag{3.9}$$

where $A = g\psi$ represents the effective coupling strength. This simple system already reveals key features of general Floquet systems. On the left-hand side of both Figure 3.1a and 3.1b, where the driving frequency is low, strong interference between different Floquet bands result in a zigzag-like structure. It can be seen that the linearly polarized driving induces larger gaps at the avoided crossings, signifying stronger hybridization between the Floquet modes. This demonstrates how different driving protocols provide a means of controlling and tuning

---

[2] It is worth noting that Bloch's theorem, which describes motion in a spatially periodic potential, developed in 1928 [76], is actually just a special case of Floquet's theorem, which was formulated much earlier in 1883 [77]. Despite its broader applicability to any system with periodic dependencies, physics literature has reserved the term "Floquet" for time-periodic systems.

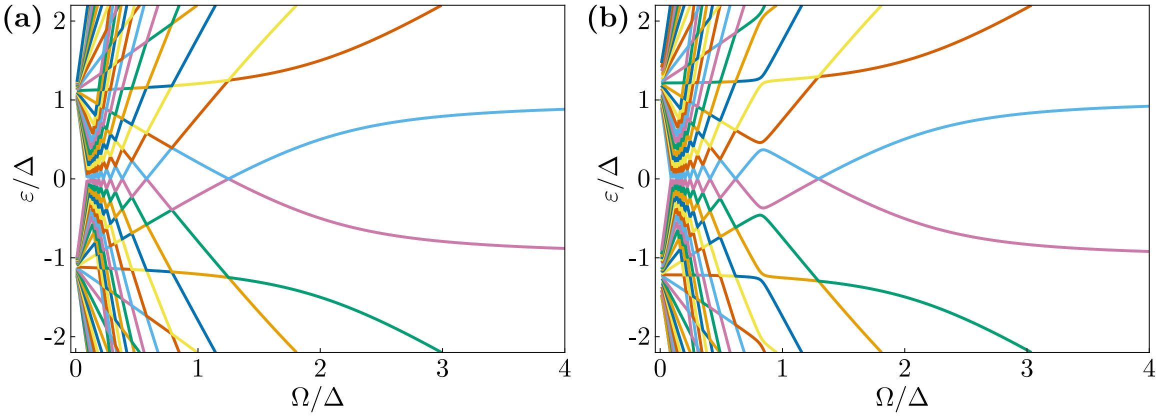

Figure 3.1: Quasi-energy spectrum of a periodically driven two-level system under **(a)** circularly polarized light, corresponding to Equation (3.8), and **(b)** linearly polarized light, corresponding to Equation (3.9), with $A/\Delta = 1$ in both cases. The Floquet matrix was truncated at $n_{max} = 25$.

quasi-energy spectra. As the driving frequency increases, an effective two-level system emerges. In the $\Omega \to \infty$ limit, both systems effectively reduce to

$$H = \Delta\sigma^z. \tag{3.10}$$

This occurs because the light field oscillates so fast that the two-level systems only experiences its time-averaged effect, which is zero. While the two-level system provides insight into the non-interacting case, a more general framework is required to treat strongly interacting systems. To this end, the Floquet Green function formalism will be introduced.

3.2 Floquet Green functions

In anticipation of treating interacting systems, it is useful to introduce the construction of Floquet Green functions [78]. However, the following framework is valid for any arbitrary function $G(t,t')$ that satisfies the periodicity condition $G(t+T,t'+T) = G(t,t')$. The first step is the introduction of Wigner coordinates, where the relative time and average time are defined as $t_r = t - t'$ and $t_a = (t+t')/2$, respectively. In these new coordinates, the periodicity is only imprinted on to the average time, leading to $G(t_r,t_a) = G(t_r,t_a+T)$. When defining the Fourier transform of $G(t_r,t_a)$, the relative time t_r has a continuous Fourier variable ω, while t_a is associated with a discrete Fourier index n. The Wigner representation of the function G is defined as [79]

$$G_n(\omega) = \int dt_r \frac{1}{T}\int_{-T/2}^{T/2} dt_a e^{i\omega t_r + in\Omega t_a} G(t,t'). \tag{3.11}$$

The variable ω has a similar correspondence to the energy in equilibrium, while the additional Floquet index n accounts for the energy exchange due to the periodic drive. The inverse transformation is given by

$$G(t,t') = \int \frac{d\omega}{2\pi} \sum_n e^{-i\omega t_r - in\Omega t_a} G_n(\omega). \tag{3.12}$$

Using the Wigner representation, the Floquet representation of G is defined as

$$G_{mn}(\omega) = G_{m-n}\left(\omega + \frac{m+n}{2}\Omega\right). \tag{3.13}$$

In this representation, the full frequency dependence is segmented into regions of size Ω, meaning that the frequency space is divided into repeating Floquet sectors. This naturally defines the Floquet Brillouin zone, given by $-\Omega/2 < \omega < \Omega/2$. After that, each frequency value ω is organized into a Floquet matrix indexed by m and n, where the indices represent the incoming and outgoing Floquet modes. A single direct transformation from the time representation to the Floquet representation is given by

$$G_{mn}(\omega) = \int dt_r \frac{1}{T}\int_{-T/2}^{T/2} dt_a e^{i(\omega+m\Omega)t} G(t,t') e^{-i(\omega+n\Omega)t'}. \tag{3.14}$$

The main advantage of the Floquet representation becomes evident when computing time integrals, specifically the ones that frequently appear in the Kadanoff-Baym equations. Consider the integral $c(t,t') = \int d\tau\, a(t,\tau)b(\tau,t')$, where both $a(t,\tau)$ and $b(\tau,t')$ are periodic in both of their time arguments with period T. Using the Wigner representation, the expression becomes

$$\int d\tau\, a(t,\tau)b(\tau,t') = \int \frac{d\nu}{2\pi} \sum_{p,q} e^{-i(\nu+\frac{p}{2}\Omega)t} a_p(\nu) b_q\left(\nu - \tfrac{p+q}{2}\Omega\right) e^{i(\nu-(\frac{p}{2}+q)\Omega)t'}. \tag{3.15}$$

Using Equation (3.14), the Floquet component satisfies

$$\begin{aligned} c_{mn}(\omega) &= \sum_p a_p\left(\omega + m\Omega - \tfrac{p}{2}\Omega\right) b_{m-n-p}\left(\omega + \tfrac{m-p+n}{2}\Omega\right) & (3.16)\\ &= \sum_p a_{m-p}\left(\omega + \tfrac{m+p}{2}\Omega\right) b_{p-n}\left(\omega + \tfrac{p+n}{2}\Omega\right) & (3.17)\\ &= \sum_p a_{mp}(\omega) b_{pn}(\omega). & (3.18)\end{aligned}$$

This result demonstrates that the time integral reduces to a matrix product in Floquet space. Time integrals of this form are the most computationally expensive part of the Kadanoff-Baym equations. The Floquet representation enables an efficient matrix-based approach which drastically reduces the numerical complexity compared to a full two-time evolution. Two other relevant time products which appear frequently are of the form $c(t,t') = a(t,t')b(t',t)$ and $c(t,t') = a(t,t')b(t,t')$. These are most conveniently computed in the Wigner representation, where they take the forms

$$c_n(\omega) = \int \frac{d\omega_2}{2\pi} \sum_{n_2} a_{n-n_2}(\omega+\omega_2) b_{n_2}(\omega_2), \text{ and } c_n(\omega) = \int \frac{d\omega_2}{2\pi} \sum_{n_2} a_{n-n_2}(\omega-\omega_2) b_{n_2}(\omega_2), \tag{3.19}$$

respectively. These expressions correspond to a cross-correlation and a convolution, both of which can be computed efficiently using FFT-based approaches.[3]

---

[3] Implementing the advancements discussed in Section 2.3 would result in an even more efficient formulation. However, the approach discussed there, was developed after the completion of this work. Therefore, the focus in this chapter will remain on the present approach, leaving optimizations as an outlook for the future.

Now that the formalism has been established, the Floquet Green function for a general periodically driven system can be obtained. Starting from

$$(i\partial_t - H(t))\, G(t,t') = \delta(t-t'), \tag{3.20}$$

applying the Floquet transformation and using Equation (3.18) leads to

$$G_{mn}(\omega) = (\omega - \mathcal{H})^{-1}_{mn} = \; m \qquad\qquad n\;. \tag{3.21}$$

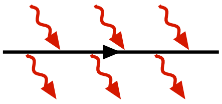

The associated Feynman diagram provides a physical interpretation of the Floquet Green function, i.e. it represents a propagator that starts in Floquet mode m, undergoing absorption and emission processes due to the periodic drive, before reaching the final Floquet mode n. While the Floquet representation is numerically efficient, the Wigner representation of the Green function is generally more useful for analyzing and discussing physical quantities. This is due to its more intuitive interpretation, where $G_n(\omega)$ describes the ω dependence of the nth oscillating mode of G with respect to the average time t_a.

3.3 Periodically Driven Anderson Lattice Model

The primary focus of this work is to understand how light irradiation affects the heavy fermion state, which requires a careful examination of light-matter interactions. In many studies of light-driven systems, the Peierls substitution is commonly employed [8, 80]. However, this approach only accounts for the nonlocal contribution of the vector potential, incorporating intraband processes while neglecting interband processes. Since the Kondo effect is primarily governed by conduction electrons near the Fermi level, modifications to the conduction spectral function due to intraband transitions play a negligible role. Instead, the key aspect to analyze is how the periodic driving influences the screening of the local impurities, which depend on interband properties. Therefore, a more rigorous treatment of light-matter interaction, where dipole transitions are explicitly included, is required. These considerations, detailed in [81, 82], lead to the following Hamiltonian

$$H = \Omega\, a^\dagger a + ig(a-a^\dagger)\sum_{i\sigma}(c^\dagger_{i\sigma}d_{i\sigma} + h.c.) - i\widetilde{g}(a-a^\dagger)d^\dagger_{i\sigma}d_{i\sigma} + H_{\mathrm{ALM}}, \tag{3.22}$$

where g and $\widetilde{g}$ is the light-matter coupling strength, $a^\dagger$ represents the creation operator of the photon mode with frequency Ω, $c^\dagger$ and $d^\dagger$ denote the conduction and impurity electrons creation operator, respectively. H_{ALM} is the Anderson lattice model Hamiltonian given in Equation (2.3). In this case, only a single photon mode is considered, and the transfer of momentum from the photons to the electrons is neglected. The light-matter coupling also introduces additional interaction terms for both the conduction and the impurity electrons, however, since the Coulomb interaction of the impurities is the largest energy scale in the system, these corrections will have a negligible effect and are therefore ignored.

To proceed, the semi-classical limit of the photon field is taken, similarly to Section 3.1.1, where the photon operator is replaced by its expectation value. This results in the following effective Hamiltonian

$$H = \sum_{k\sigma}\varepsilon_{k\sigma}c^\dagger_{k\sigma}c_{k\sigma} + \sum_{i\sigma}\varepsilon_d(t)d^\dagger_{i\sigma}d_{i\sigma} + \sum_{i\sigma}(V(t)c^\dagger_{i\sigma}d_{i\sigma} + h.c.) + Un^d_{i\downarrow}n^d_{i\uparrow}, \tag{3.23}$$

where the periodic driving is incorporated into the impurity energy level and hybridization as $\varepsilon_f(t) = \varepsilon_f^0 \left(1 + \Delta_\varepsilon \cos(\Omega t)\right)$, and $V(t) = V_0 \left(1 + \Delta_V \cos(\Omega t)\right)$, where Δ represents the driving strength. For simplicity, only a monochromatic drive is considered. A similar approach has been applied in the study of periodically driven quantum dots [83, 84], where however only the impurity energy level was modulated.

3.3.1 Heat Bath

Closed periodically driven systems without local conserved quantities tend to absorb the energy coming from the drive indefinitely, eventually reaching an infinite-temperature state [85, 86]. Such a state is completely featureless, erasing both the intrinsic properties of the system and any nontrivial effects induced by the drive. In the periodically driven single-impurity case, this problem is naturally mitigated, because the conduction electrons, which remain in equilibrium as they are not directly driven, act as a heat bath for the impurity. This ensures that the impurity thermalizes to the conduction electron temperature and the Kondo effect persist. However, in the lattice case, the conduction electrons are renormalized via the impurities and therefore are also affected by the periodic drive. This makes the system prone to uncontrollable heating. To prevent this, various stabilization mechanisms have been proposed, such as prethermalization, where the system relaxes into a long-lived metastable state [2], many-body localization, where disorder localizes the system in phase space, leading to non-ergodic dynamics [87], and coupling the system to an external bath, which dissipates excess energy and stabilizes the system [88].

In realistic light-driven materials, achieving a perfectly isolated environment where the drive couples only to the degrees of freedom of interest is nearly impossible. Instead, in the present case, the electronic bands relevant to the Kondo effect are necessarily coupled to background phonons and other electronic bands, which provide intrinsic dissipation channels that prevent heating. To incorporate this, a fermionic bath which couples to the conduction electrons via particle exchange is introduced. This leads to the final Hamiltonian for the periodically driven Anderson lattice model to be given by

$$\begin{aligned} H = &\sum_{n\alpha} \varepsilon_n^B B_{n\alpha}^\dagger B_{n\alpha} + \sum_{k\sigma} \varepsilon_{k\sigma} c_{k\sigma}^\dagger c_{k\sigma} + \sum_{i\sigma} \varepsilon_d(t) d_{i\sigma}^\dagger d_{i\sigma} + U n_{i\downarrow}^d n_{i\uparrow}^d \\ &+ \gamma \sum_{kn\sigma\alpha} \left(B_{n\alpha}^\dagger c_{k\sigma} + h.c. \right) + \sum_{i\sigma} (V(t) c_{i\sigma}^\dagger d_{i\sigma} + h.c.), \end{aligned} \tag{3.24}$$

where $B^\dagger$ corresponds to the bath creation operator, and γ is the bath coupling strength. As shown in Section 1.2.5, the bath effect can be incorporated as an additional self-energy contribution. In a non-interacting system, such bath coupling ensures thermalization even in the limit of vanishing bath coupling strength. However, in an interacting system, the self-energy coming from interactions will compete with the effects of the bath. Therefore, if the bath coupling is too weak, it will fail to cool the system down, while if the bath coupling is too strong, the Kondo effect will be washed out. Therefore, a careful tuning of the bath coupling strength is required. To further minimize the effects on the Kondo physics, the bath is coupled only to the conduction electrons and is chosen to be featureless.

3.3.2 Floquet Non-Crossing Approximation

In anticipation of constructing the DMFT formalism for the periodically driven case, the single impurity solver is first treated to incorporate periodic driving, leading to all the Green functions and self-energies becoming matrices in both Floquet and Keldysh space. Since the NCA in Section 2.3 was formulated in the non-equilibrium steady-state regime, its extension to the Floquet formalism is straightforward within this matrix structure. In the present case, the effects of the periodic driving affects two quantities, the impurity energy level, and the hybridization. The first of which leads to the following Floquet form of the Dyson equation for the retarded Green function

$$\left[G_b^{R\,-1}\right]_{mn}(\omega) = (\omega + n\Omega)\delta_{m,n} - (\Sigma_b^R)_{mn}(\omega), \tag{3.25}$$

$$\left[(G_{f\sigma}^R)^{-1}\right]_{mn}(\omega) = (\omega + n\Omega)\delta_{m,n} - (\varepsilon_d)_{m-n} - (\Sigma_{f\sigma}^R)_{mn}(\omega), \tag{3.26}$$

where the impurity energy level acquires a Floquet structure, given by

$$(\varepsilon_d)_{m-n} = \frac{1}{T}\int_{-T/2}^{T/2} dt\, e^{i(m-n)\Omega t}\varepsilon_d(t). \tag{3.27}$$

To show how the hybridization driving is incorporated into the self-energy expressions, it is useful to express them in the time domain

$$\Sigma_b(t,t') = -i\sum_\sigma V(t)G_{f\sigma}(t,t')g_{c\sigma}(t',t)V(t')^*, \tag{3.28}$$

$$\Sigma_{f\sigma}(t,t') = i\,V(t)G_b(t,t')g_{c\sigma}(t,t')V(t')^*. \tag{3.29}$$

Since the conduction electrons are not affected by the driving, it is convenient to define a modified conduction electron propagator that absorbs the periodic time dependence of the hybridization

$$\tilde{g}_{c\sigma}(t,t') = (1 + \Delta_v v(t))g_{c\sigma}(t,t')(1 + \Delta_v v(t')), \tag{3.30}$$

where the drive is incorporated in $v(t)$. With this definition, the self-energy expressions take the familiar form

$$\Sigma_b(t,t') = -i|V_0|^2\sum_\sigma G_{f\sigma}(t,t')\tilde{g}_{c\sigma}(t',t), \tag{3.31}$$

$$\Sigma_{f\sigma}(t,t') = i\,|V_0|^2 G_b(t,t')\tilde{g}_{c\sigma}(t,t'). \tag{3.32}$$

which are most conveniently evaluated in the Wigner representation

$$(\Sigma_b^{\lessgtr})_n(\omega) = -i|V|^2\sum_{\sigma l}\int\frac{d\omega'}{2\pi}(G_{f\sigma}^{\lessgtr})_{n-l}(\omega'+\omega)(g_{c\sigma}^{\gtrless})_l(\omega'), \tag{3.33}$$

$$(\Sigma_{f\sigma}^{\lessgtr})_n(\omega) = i|V|^2\sum_{l}\int\frac{d\omega'}{2\pi}(G_b^{\lessgtr})_{n-l}(\omega-\omega')(g_{c\sigma}^{\lessgtr})_l(\omega'). \tag{3.34}$$

To express $\tilde{g}_{c\sigma}(t,t')$ in the Wigner representation, Equation (3.30) can be rewritten as

$$\tilde{g}_{c\sigma}(t,t') = \int dt_1\int dt_2\tilde{v}(t,t_1)g_{c\sigma}(t_1,t_2)\tilde{v}(t_2,t'), \tag{3.35}$$

where $\tilde{v}(t,t_1) = (1 + \Delta_v v(t))\delta(t-t_1)$. Using Equation (3.18), this can be expressed as a matrix multiplication in the Floquet representation

$$\tilde{g}_{mn}^{c\sigma}(\omega) = \sum_{kl}\tilde{v}_{mk}(\omega)g_{kl}^{c\sigma}(\omega)\tilde{v}_{ln}(\omega), \tag{3.36}$$

where $\tilde{v}_{mn}(\omega) = \delta_{m,n} + \Delta_v v_{m-n}$. Meaning that the frequency dependence of $\tilde{g}^{c\sigma}_{mn}(\omega)$ comes entirely from the original conduction electron propagator, while the Floquet structure comes purely from the hybridization driving, as expected. Finally, this expression can be converted into the Wigner representation by using Equation (3.13). The last part needed for a full self-consistent set of equations is the lesser Green function, given in Floquet form by

$$G^<_{mn}(\omega) = \sum_{k,l} G^R_{mk}(\omega)\Sigma^<_{kl}(\omega)G^A_{ln}(\omega). \tag{3.37}$$

As in Section 2.3, the lesser components of Equations (3.34) and (3.37) exhibit a scale invariance, meaning that both equations remain satisfied when multiplied by a factor, which can lead to numerical instabilities. To mitigate this, the lesser components of the Green function is normalized, such that the time average of the constraint Q is set to one, where

$$Q_{n=0} = i\int \frac{d\omega}{2\pi}\left((G^<_b)_{n=0}(\omega) - \sum_\sigma (G^<_{f\sigma})_{n=0}(\omega)\right). \tag{3.38}$$

Since DMFT was constructed in the non-equilibrium steady-state, its extension to the Floquet formalism is straightforward. The self-consistency structure remains unchanged, as outlined in Section 2.5, with the primary difference being that all quantities, such as the local Green function, self-energy, and Weiss field now acquire a matrix structure in both Floquet and Keldysh space.

3.3.3 Results

The effects of the periodic driving are best studied via the time averaged impurity spectral function and occupation, which reveal the persistence or destruction of the Kondo peak and the emergence of non-equilibrium steady states. Therefore, the results correspond to the time averaged $n = 0$ Wigner representation of the relevant functions. To avoid flooding this section with plots, almost all of the results for the driven single impurity case are presented in Chapter B. The general trend for the single impurity case is the same as the heavy-fermion case, however, in general, the response in the heavy-fermion system is more sensitive to the drive.

Examples of periodically driven local impurity spectra for the lattice case along with their corresponding band structure are shown in Figure 3.2. Whether the impurity energy level or the hybridization is driven, Floquet replicas of the heavy band appear in both cases. Since the spectral function is normalized, as spectral weight is redistributed to the Floquet replicas, the main Kondo peak must decrease, however, this suppression does not indicate a breakdown of the Kondo effect. Rather, in addition to the usual spin-flip processes responsible for the Kondo effect, the system now allows for photon-assisted transitions, where electrons can absorb and emit photons while still contributing to the Kondo effect. This behavior is highlighted in the occupation function, shown in the insets of Figure 3.2a and Figure 3.2b. The first notable feature is its deviation from the Fermi distribution, indicating a non-thermal steady state. States below the Fermi level are depleted and states above it are populated. These dips and peaks occur at integer multiples of the driving frequency, indicating that excited states at $\omega = \Omega$ are populated from electrons at the Fermi level, while depletion at $\omega = -\Omega$ indicates that these electrons are promoted to the Fermi level. Despite this non-thermal structure, a crude effective temperature can be obtained by fitting a Fermi distribution to a small energy window around the Fermi level. Doing so shows that the system has been significantly heated by the driving, seen as by the effective temperature being larger than that of the undriven case. The heating is more severe in the hybridization driven case compared to driving the impurity

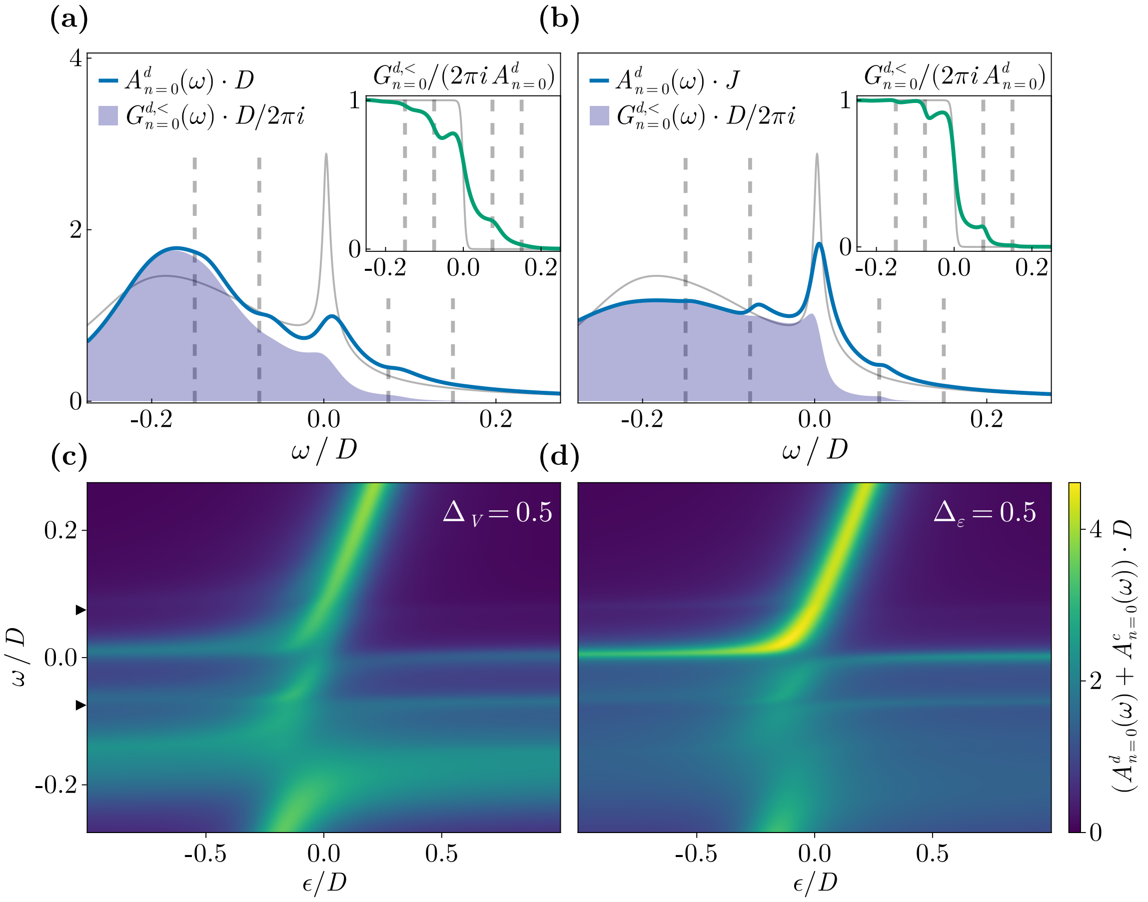

Figure 3.2: Time averaged local impurity spectral functions and band structure for the periodically driven Anderson lattice model with parameters $\varepsilon_d = -0.175D$, $V = \sqrt{0.025}D$, $\gamma = V/2$, $\beta = 300/D$, and $\Omega = 0.075D$, leading to a Kondo temperature in the undriven case of $T_K \approx 7\cdot 10^{-3}D$, where D is the bandwidth of the semi-circular density of states. The driving strengths are **(a)** and **(c)** $\Delta_V = 0.5$, and **(b)** and **(d)** $\Delta_\varepsilon = 0.5$. The solid blue line represents the spectral function, while the shaded region corresponds to the lesser Green function. The vertical lines indicate integer multiples of the driving frequency, marking the positions of the Floquet replicas. The gray line shows the spectral function in the absence of driving and the inset shows the occupation. The band structure is plotted as a function of ϵ which is the dispersion of the semi-circular density of states, given in Equation (2.112).

energy level, therefore leading to a larger suppression of the Kondo peak. An interpretation for this sensitivity to the hybridization driving is that the Kondo temperature T_K depends exponentially on V^2 and ε_d, making it much more sensitive to changes in the hybridization than to changes in the impurity level.

To study the effects of the driving frequency, a heatmap of the local impurity spectral function is shown in the left panel of Figure 3.3b as a function of ω and Ω. For small driving frequencies, the peak structure remains largely undisturbed. This is expected, as the small driving frequency regime acts as a small perturbation around the Kondo state, which remains robust. As Ω increases, the main Kondo peak, shown in Figure 3.3a diminishes and recovers again at large driving frequencies. This is because when the driving frequency is large, the rapid oscillations effectively average out, thus removing the periodic driving altogether. Once

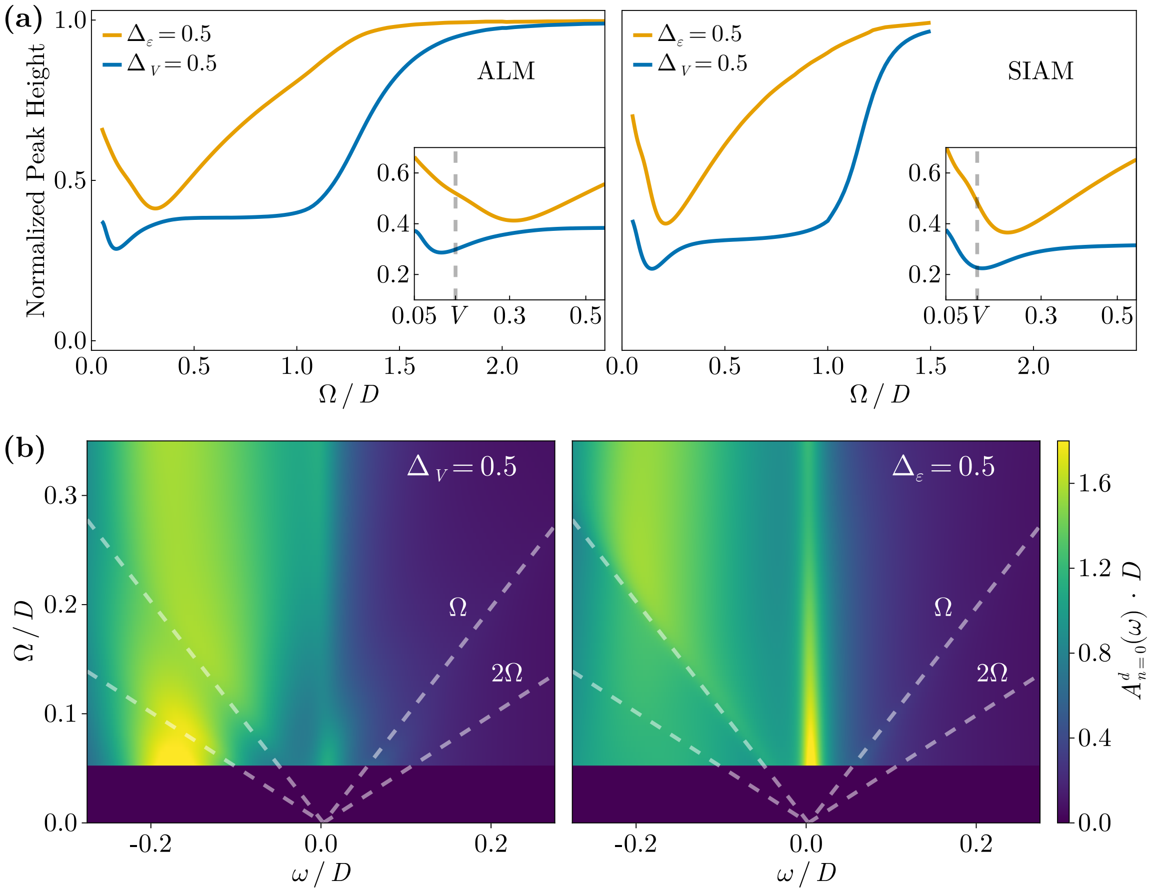

Figure 3.3: **(a)** Dependence of the normalized Kondo peak height on the driving frequency Ω/D, for both impurity energy level and hybridization driving for the Anderson lattice and single impurity Anderson model. The parameters are the same as in Figure 3.2. The inset shows the smaller driving frequencies, showing that the minimum occurs near $\Omega \approx V$. **(b)** Driving frequency dependence of the local impurity spectral function. Integer multiples of the driving frequency are given by a dashed line.

again it is seen that the influence of the hybridization driving has a much stronger effect on the Kondo suppression than the impurity energy level driving. In the hybridization driven case, the most pronounced suppression occurs when the driving frequency is comparable to the hybridization, $\Omega \approx V$. This happens because at this frequency, the photons assist in the virtual spin-flips, meaning that the system is equivalent to an effective Anderson model with an enhanced hybridization. This increased hybridization shifts the system towards the mixed valence regime, thus destroying the Kondo state. This effect is even better seen in the driven single impurity case, see right panel of Figure 3.3a, where the minimum is exactly at V. In the case of driving the impurity energy level, a minimum in the peak height is also observed, occurring at a driving frequency Ω larger than both V and ε_d, where no clearly relevant energy scale is present. Since the suppression appears to have a simple frequency dependence, it suggests that the suppression is caused by a single mechanism across the large frequency range. In contrast, with the hybridization driven case, which shows a secondary dip and a more complex structure. Therefore, this minimum is attributed to the competition of Kondo effect and heating induced by the drive. However, the precise location of the minimum remains an

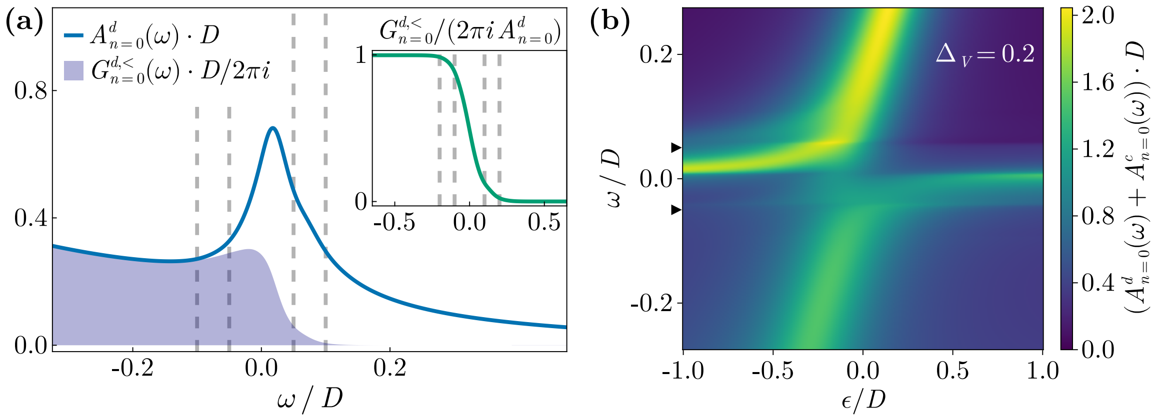

Figure 3.4: **(a)** Spectral function and **(b)** band structure of the periodically driven Anderson lattice model with $\varepsilon_d = -0.5D$, $V = \sqrt{0.1}D$, $\gamma = V/2$, $\beta = 50/D$, and $\Omega = 0.05D$, leading to a Kondo temperature $T_K \approx \Omega$.

open question.

The destruction of the heavy fermion state is best seen in the band structure. Due to the Floquet Brillouin zone, hundreds of Floquet modes are required to resolve the relevant frequency range, which has to be larger than the bandwidth, due to the convolution integrals. Specifically, for the chosen parameters in Figure 3.2, 121 Floquet modes were used to achieve a maximum frequency of $\omega_{max} = 3D$. Therefore, for these parameters driving the system at the Kondo temperature is too numerically demanding. To study the interference effects of the drive and the formation of the heavy fermion state, a parameter regime with a larger T_K is considered, allowing for $\Omega \approx T_K$ driving. One might expect that at these frequencies the heavy quasiparticles would be disrupted, instead, the system appears to be largely unaffected, suggesting that the heavy fermion state is very resilient to low-frequency drive. However, due to convergence limitations, reaching stronger driving strength was not possible. As a result, analyzing the sensitivity of the heavy fermion state to the drive and its eventual breakdown at large driving amplitudes is left as an outlook.

3.4 Summary and Outlook

In this work, the Floquet formalism was incorporated into the DMFT formalism, closely following [8, 71], with NCA as the impurity solver. This approach is applicable to any driving frequency, allowing for a broad analysis of non-equilibrium states. This formalism was used to analyze periodically driven heavy-fermion systems. To ensure a well-defined steady state, a cooling bath was included which allows the heat from the drive to be dissipated away. This is essential, as it is well known that Floquet driving can lead to uncontrolled heating.

A key aspect studied here was the role of light matter interaction, with a particular focus on both inter- and intra-band contribution. Considering interband contribution of the light matter coupling is crucial, because the Kondo effect is highly sensitive to modifications in the hybridization, which are not captured by the Peierls substitution. This consideration proved to be essential, as hybridization driving was found to have a significantly stronger impact on the heavy-fermion state compared to only driving the impurity energy level. This was attributed to the exponential dependence of the Kondo temperature on the square of the hybridization strength, whereas the dependence on the impurity energy level is linear in the exponent, highlighting the high sensitivity to hybridization driving.

The results showed that Floquet replicas of the Kondo peak generally appear under periodic driving, consistent with the Floquet theorem. However, a strong suppression of the Kondo peak occurs when the driving frequency is comparable to the hybridization, $\Omega \approx V$. In this regime, virtual photon-assisted spin-flip processes enhance the effective hybridization, shifting the system into a mixed valence regime, leading to a destruction of the heavy fermion state. Additionally, the heavy fermion state exhibited surprising resilience to driving frequencies close to T_K.

A potential direction for future work is to introduce periodic driving into the time dependent Kadanoff-Baym equations of motion, and solving them using a two-time stepper as developed in [89]. This approach would allow for a fully dynamical treatment of the system without relying on the semi-classical or steady-state assumptions required to apply the Floquet theorem. In particular, it would enable the study of transient dynamics and how the Floquet steady-state is reached.

An improvement in numerical stability can be achieved by implementing the NCA construction described in Section 2.3, which was developed after this work. Since it directly operates in the time domain, the convolution integrals of the self-energy, given in Equations (3.33) and (3.34), reduce to simple products in time space. This would reduce the computational cost and improve numerical stability, making it possible to reach even lower driving frequencies and stronger driving strengths.

Another outlook is the question of whether periodic driving can be used not only to suppress the Kondo effect but also to induce it. Here it was demonstrated how the Kondo regime transitions into the mixed valence regime, when the driving frequency and the hybridization are comparable. However, it remains as an interesting question whether a system which is not in the Kondo regime can be driven into the Kondo regime. This could provide new ways to dynamically realize Kondo physics in systems where no Kondo effect is present in equilibrium.

Finally, another promising direction is to consider circularly polarized light, which could induce topological effects in the heavy fermion system [80]. This could provide a mechanism for engineering Floquet-induced topological Kondo insulators.

Chapter 4

Time-Resolved Collapse and Revival of the Kondo State

Ce-based materials were the first materials in which the heavy-fermion state was discovered [26]. Among them, one of the most influential to the development of the field is $\mathrm{CeCu_6}$ [90, 91]. Upon doping with Au, $\mathrm{CeCu_6}$ transitions from a heavy Fermi liquid into a non-Fermi liquid regime, and can be further tuned into an antiferromagnetic (AFM) state [92, 93]. The substitution of Cu atoms by the larger Au atoms expands the lattice, which reduces the hybridization between the conduction electrons and the localized f-electrons. This causes the Kondo coupling J to decrease, and for the Ruderman-Kittel-Kasuya-Yosida (RKKY) interaction to increase. The interplay between these competing energy scales can be qualitatively understood within Doniach's phase diagram, see Figure 2.6, which illustrates how reducing J drives the system from a Kondo-screened heavy Fermi liquid into an RKKY dominated AFM phase. This transition goes through a quantum critical point (QCP), where critical fluctations give rise to non-Fermi liquid behavior.

While Doniach's phase diagram gives an intuitive picture based on the involved energy scales, the microscopic mechanism of the quantum phase transition is a subject of ongoing heavy debate [94–96]. Two pictures have gained the most attention. One is based on a spin-density wave (SDW) instability, which states that since the system is a Fermi liquid, despite the heavy mass of the quasiparticles, it can undergo a conventional magnetic phase transition [97]. The second picture suggests that magnetic ordering due to the RKKY interaction and the Kondo screening compete with one another. This would mean that as the phase transition is approached, the heavy quasiparticles disintegrate [95]. Both of these pictures have had noteable successes. The former SDW description has been successfully applied to materials such as $\mathrm{CeCu_2Si_2}$ [98] and $\mathrm{Ce_{1-x}La_xRu_2Si_2}$ [98]. While the latter Kondo breakdown scenario captures the behavior observed in $\mathrm{CeCu_{6-x}Au_x}$ [96] and $\mathrm{YbRh_2Si_2}$ [99]. The presence of Kondo correlations, magnetic ordering, and critical fluctuations makes it experimentally challenging to study the underlying physics as capturing the interplay of these phenomena requires advanced and highly sensitive techniques.

One candidate for such an experimental technique is THz time-domain spectroscopy. In such a setup, the material is excited by a pulse, and then the subsequent reflected pulse is measured. This method, induces minimal heating, and since THz radiation lies in the same energy range as the Kondo scale, allows for precise excitation of the Kondo quasiparticles. This makes it well-suited to capture long time dynamics associated with low-energy excitations such as those arising from Kondo physics. This technique was applied to $\mathrm{CeCu_{6-x}Au_x}$ to probe its behavior across the quantum phase transition in [68]. The initial response to the THz pulse

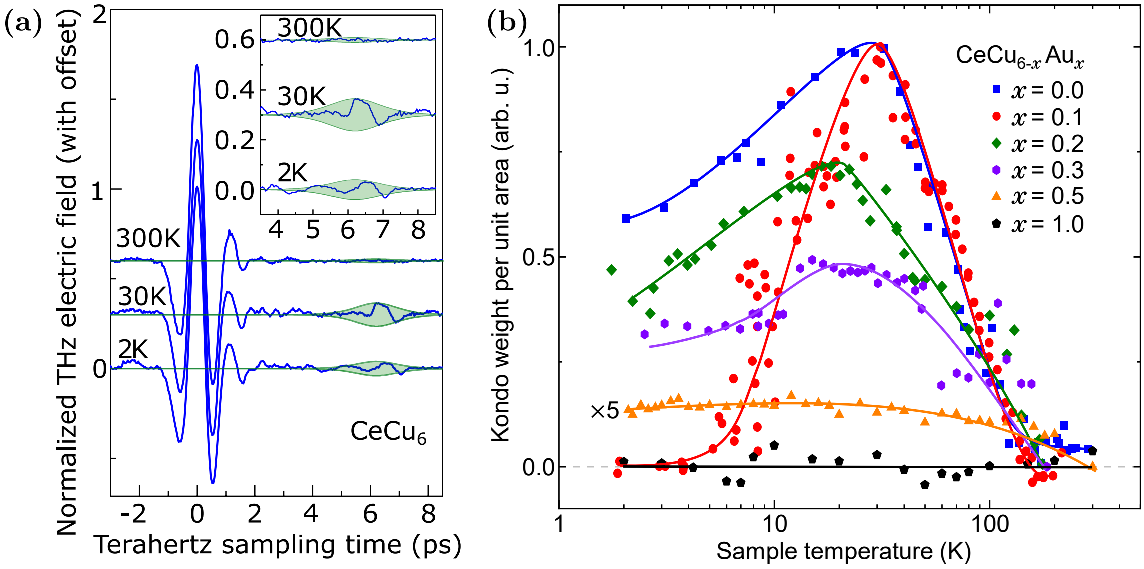

Figure 4.1: **(a)** Time-resolved THz reflectivity of CeCu$_6$ at different temperatures, showing the instantaneous reflection at short times and initial oscillations due to crystal field splitting, taken from [68]. The green shaded region shows the envelope of the delayed response. **(b)** Kondo weight computed from the area of the green shaded region as a function of temperature for CeCu$_{6-x}$Au$_x$ at several gold concentrations, taken from [100].

is a sharp reflectivity peak, corresponding to a direct reflection of the incident pulse. After this peak decays, a secondary, delayed pulse emerges. Using phenomenological rate equations, this delayed response was interpreted as a signature of Kondo coherence recovery. First the pump pulse disrupts the coherence of the heavy-fermion state, preventing excited electrons from relaxing back into the heavy band. These electrons remain in high-energy states until the pump pulse has passed and Kondo coherence is reestablished, at which point they can relax back. The resulting delayed optical signal thus reflects the reformation of the Kondo state and is directly proportional to the quasiparticle weight.

Further experiments considered a wider range of gold concentrations [100], allowing the construction of a Kondo weight diagram as a function of temperature for various concentrations, as shown in Figure 4.1. For $x = 0$, the quasiparticle weight continuously increases with decreasing temperature, consistent with the crossover behavior of the Kondo effect. Upon further decrease in temperature, the growth of the Kondo weight is suppressed but remains finite at the lowest measured temperature. This suppression is associated with the increasing proximity to the QCP. For $x = 0.1$, near the QCP, the Kondo weight initially grows similarly to the undoped case but ultimately collapses. Deep in the AFM regime, at $x = 1$, no Kondo response is observed for any temperature. This indicates that the influence of the RKKY interaction already begins at much higher temperatures than anticipated, namely, orders of magnitude above the Néel temperature [101]. Intermediate concentrations $0.1 \leq x \leq 0.5$, also show an initial increase in the Kondo weight, but never reach the same Kondo weight as in undoped case. At the lowest temperatures, the Kondo weight remains finite, however, since the Néel temperature lies below the lowest temperature [93], it is reasonable to assume that the Kondo weight would vanish at lower temperatures. Considering this, these experimental results provide a consistent picture with the interpretation that the competition of the RKKY and the Kondo interaction are of crucial importance to understand the behavior across the phase diagram.

This entire interpretation depends on the claim that the delayed signal originates from the Kondo response. While this explanation can explain all the observed behaviors, only a phenomenological model of rate equations has been used in [68] and other mechanisms, such as superradiance, reflections coming from the THz generation crystal, or other mechanism could in principle lead to similar delayed features [68]. Although the observed timescales are inconsistent with the competing interpretations, and none of them can explain the temperature dependence of the secondary pulse, a proper microscopic treatment is required to confirm the many-body origin of the signal. Theoretical modeling of this experiment is challenging. It demands a full non-equilibrium treatment of a strongly correlated heavy-fermion system undergoing a phase transition into an AFM state. Even in equilibrium, neither of these phases alone can, in general, be solved exactly. Since the goal is to establish whether a Kondo system can, in principle, produce a delayed optical response, the following analysis is restricted to the undoped compound, enabling the use of the methods developed in earlier chapters.

To resolve the non-equilibrium nature of the problem, the DMFT+NCA approach introduced in Chapter 2, will be used. However, unlike in Chapter 3, a semiclassical treatment of the light is no longer sufficient. This is because the THz pulse has a frequency close to the Kondo scale and to capture the measured reflectivity, the full renormalized photon pulse needs to be computed. Therefore, the light field needs to be treated in a full quantum treatment. This is accomplished by solving the light-matter coupled Anderson lattice model using the Kadanoff-Baym equations, incorporating a full two-time evolution for the Green functions [89]. The work presented in this chapter closely follows [102], which the reader is highly encouraged to refer to.

4.1 THz Pumped Anderson Lattice Model

The first step towards analyzing the optical response of a heavy-fermion system under irradation of a laser field is to incorporate light matter interactions into the Anderson lattice model. This is done analogously to the procedure in Section 3.3, resulting in the Hamiltonian

$$H = \omega_0 \, a^\dagger a - ig(a + a^\dagger) \sum_{i\sigma} (c^\dagger_{i\sigma} d_{i\sigma} + h.c.) + H_{\mathrm{ALM}}, \tag{4.1}$$

where $a^\dagger$ represents the creation operator of the photon mode with frequency ω_0, and g is the light-matter coupling strength. $c^\dagger$ and $d^\dagger$ denote the conduction and impurity electrons creation operator, respectively. The transfer of momentum from the photons to the electrons, as well as light-mediated intra-band contributions and interactions are neglected, which is justified in the THz regime. H_{ALM} is the standard Anderson lattice model Hamiltonian as defined in Equation (2.3). Only a single photon mode, corresponding to the one that couples directly to the heavy band, is considered. Since the photon frequency is close to the Kondo energy scale $\omega_0 \lesssim T_K$, there is no separation of time scales. As a result, a semiclassical approximation, like the one used in the previous section, is not applicable, and thus a full quantum field treatment is required. In a realistic setting, most of the energy from a pump pulse dissipates throughout the material, thereby minimizing heating. In the model, dissipation channels must be introduced explicitly. This is done by coupling to an additional fermionic bath, which represents additional electronic bands in the material, as discussed in Sections 1.2.5 and 3.3.1,[1]

---

[1] Another important dissipation channel involves the emission of photons into modes other than the pump mode a, which can be incorporated by a bosonic bath. This bath would enter as an interaction term into the Hamiltonian, contributing an extra self-energy term. As will be seen later, a steady-state solution in the absence of the pump is required for solving the time-dependent problem. In the steady-state, a bosonic bath alone cannot imprint a chemical potential onto the fermionic system, since it couples to the density, and therefore cannot fix

leading to the following additive term to the action

$$\int_{\mathcal{C}} dtdt' \sum_{i\sigma} d^{\dagger}_{i\sigma}(t) \left[\gamma^2 \Delta^d_{\text{bath}}(t,t')\right] d_{i\sigma}(t'). \tag{4.2}$$

4.1.1 Integro-Differential Formulation of DMFT+NCA

To capture the temporal response of the system to the external THz pump pulse, the DMFT formulation introduced in Section 2.5 must be kept in the time representation. In principle, the only modification to the construction is that the Fourier transform, which is applied after Equation (2.81), is no longer performed. Nevertheless, it is worthwhile to present the full equations in the Kadanoff-Baym integro-differential form.

In this setup, the local problem consists of the impurity d-electrons embedded in an effective bath, described by the Weiss field, which incorporates the lattice effects. Since only the conduction electrons have a hopping term, they are the only ones that acquire a Weiss field. Assuming a semi-circular density of states[2] for the conduction electrons, $A^0_c(\omega) = 2\sqrt{D^2-\omega^2}\,\Theta(|\omega|-D)/(\pi D^2)$, leads to the following equation of motion

$$i\partial_t \mathcal{G}^c(t,t') = \delta_{\mathcal{C}}(t,t') + \frac{D^2}{4}\left(G^c_{loc} \star \mathcal{G}^c\right)(t,t')\ , \tag{4.3}$$

where $\mathcal{G}^c$ and G^c_{loc} correspond to the Weiss and local conduction electron Green function, respectively, and D is the half-bandwidth. The spin indices are suppressed and the convolution is defined as $(a \star b)(t,t') \equiv \int_{\mathcal{C}} d\bar{t}\, a(t,\bar{t}) b(\bar{t},t')$, where $\mathcal{C}$ is the Keldysh contour. The equation of motion for the local conduction electron Green function can be obtained by acting with $\mathcal{G}^{-1}(t,t')$ on the T-matrix equation, obtaining

$$i\partial_t G^c_{loc}(t,t') = \delta_{\mathcal{C}}(t,t') + \left(\left(V^2 + \Xi(t,t')\right) \cdot G^d \star \mathcal{G}^c + \frac{D^2}{4} G^c_{loc} \star G^c_{loc}\right)(t,t'), \tag{4.4}$$

where $\Xi(t,t') = ig^2[G_a(t,t') + G_a(t',t)]$ encodes the photon contribution, and G^d is the local d-electron Green function. To obtain this, the impurity problem is solved using the auxiliary particle formalism, described in Section 2.2.1, by expressing the physical operator as $d^{\dagger}_{\sigma} = f^{\dagger}_{\sigma} b$. A conserving approximation is utilized by constructed the leading order Luttinger-Ward functional for the auxiliary particle system, which is given by

$$\Phi[G] = -\int_{\mathcal{C}} dt\, dt' \sum_{\sigma} \mathcal{G}^c_{\sigma}(t,t') G_b(t,t') G_{f_\sigma}(t',t)\left(V^2 + \Xi(t,t')\right). \tag{4.5}$$

It can be seen from Figure 4.2 that the Luttinger Ward contains both the standard NCA diagram as well as an additional diagram that incorporates the photon coupling. The equations of motion for the auxiliary particles take the standard Kadanoff-Baym form

$$(i\partial_t - \varepsilon_d) G_{f_\sigma}(t,t') = \delta_{\mathcal{C}}(t,t') + (\Sigma_{f_\sigma} \star G_{f_\sigma})(t,t') \tag{4.6}$$

$$i\partial_t G_b(t,t') = \delta_{\mathcal{C}}(t,t') + (\Sigma_b \star G_b)(t,t') \tag{4.7}$$

---

the particle number. Therefore, a fermionic bath, which does fix the particle number must also be introduced, see [102] for details. Since thermalization can be achieved by only considering a fermionic bath, this additional bosonic bath is not considered here.

[2] In non-equilibrium, the semi-circular density of states makes the problem numerically tractable. Without this choice, each individual k-mode would have to be time-evolved and at each time step a k-sum would have to be performed. In three dimensions, obtaining a reasonably smooth density of states would require at least 10^3 k-points, making the computation extremely demanding. Since Kondo physics is essentially only governed by the density of states at the Fermi energy, the precise shape of the density of states has no qualitative impact, thereby justifying this approximation.

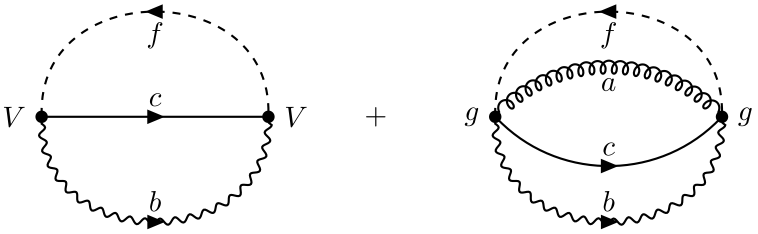

Figure 4.2: Luttinger-Ward functional for the single impurity Anderson model in auxiliary particle representation with the light-matter interactions introducing a second NCA diagram. The solid line represents the conduction electron propagator, the dashed line represents the fermionic f propagator, the wavy line represents the bosonic b propagator, and the curly line represents the photon a propagator.

where the self-energies are obtained by functional derivatives of the Luttinger-Ward functional as

$$\Sigma_{f_\sigma}(t,t') = i\left(V^2 + \Xi(t,t')\right)\mathcal{G}^0_{c_\sigma}(t,t')G_b(t,t'), \tag{4.8}$$

$$\Sigma_b(t,t') = -i\left(V^2 + \Xi(t,t')\right)\sum_\sigma G_{f_\sigma}(t,t')\mathcal{G}^0_{c_\sigma}(t',t). \tag{4.9}$$

When comparing this problem to the standard NCA, it can be seen that the hybridization is renormalized by the presence of the photon field, such $V^2 \to \left(V^2 + \Xi(t,t')\right)$. In the $\zeta \to 0$ limit, auxiliary particle Green functions obey $G^R(t,t') = \theta(t-t')G^>(t,t')$, see Equation (2.46), simplifying the equations of motions. Incorporating this, the equations of motion for the greater and lesser Green functions are given by

$$(i\partial_t - \epsilon_{f,b})G^>_{f,b}(t,t') = \int_{t'}^{t} d\bar{t}\,\Sigma^>_{f,b}(t,\bar{t})G^>_{f,b}(\bar{t},t'), \tag{4.10}$$

$$(i\partial_t - \epsilon_{f,b})G^<_{f,b}(t,t') = \int_{t_0}^{t} d\bar{t}\,\Sigma^>_{f,b}(t,\bar{t})G^<_{f,b}(\bar{t},t') - \int_{t_0}^{t'} d\bar{t}\,\Sigma^<_{f,b}(t,\bar{t})G^>_{f,b}(\bar{t},t'), \tag{4.11}$$

where $\epsilon_f = \varepsilon_f$ for the fermions and $\epsilon_b = 0$ for the bosons, representing the corresponding free part of the Hamiltonian. The advantage of using the greater and lesser Green functions becomes evident from their symmetries. As seen from their definitions in Equation (1.29), they satisfy the relation

$$G^{\lessgtr}(t,t')^\dagger = -G^{\lessgtr}(t',t). \tag{4.12}$$

This implies that after time evolving in the first time index, the time evolution of the second time index can be obtained by mirroring, according to the above equation. This significantly simplifies the two-time evolution scheme, where now only a single diagonal step in the two-time plane is required.

Due to the auxiliary particle projection, the self energies of both the conduction electron and the photon vanish in the $\zeta \to 0$ limit. Meaning that since the photons do not get a DMFT like treatment, the photon pulse remains free throughout the time evolution. The reflected pulse, which is the one that is relevant to the experimental observation, is obtained via a T-matrix equation that can be obtained from the Hamiltonian and computed at the end of the time evolution, given by

$$G_a(t,t') = G^0_a(t,t') + \left(G^0_a \star T_a \star G^0_a\right)(t,t'), \tag{4.13}$$

where

$$T_a(t,t') = -ig^2 \sum_\sigma \left(G_{d_\sigma}(t,t')\mathcal{G}^c_\sigma(t',t) + G_{d_\sigma}(t',t)\mathcal{G}^c_\sigma(t,t') \right) , \tag{4.14}$$

and G^0_a incorporates the THz pump pulse. This incoming pulse is best described by a Gaussian in the temporal and the spectral direction [102], thus giving the following greater and lesser functions

$$G^{0,>}_a(T,\tau) = -i \left(1 + \bar{n}_a \; e^{-\frac{\Omega_0^2}{2}(T-T_0)^2} \right) \; e^{-i\omega_0\tau} e^{-\frac{\Omega_0^2}{8}\tau^2}, \tag{4.15}$$

$$G^{0,<}_a(T,\tau) = -i\bar{n}_a \; e^{-\frac{\Omega_0^2}{2}(T-T_0)^2} \; e^{-i\omega_0\tau} e^{-\frac{\Omega_0^2}{8}\tau^2}, \tag{4.16}$$

where $T = (t+t')/2$ denoting the time average and $\tau = t - t'$ denoting the relative time are the Wigner coordinates. Here, T_0 is the time of the pulse maximum and ω_0, Ω_0 and $\bar{n}_a$ set the central frequency, frequency width, and peak photon number, respectively.

4.1.2 Results

The integro-differential Kadanoff-Baym equations, for the Weiss field, the local conduction electron Green function, as well as the auxiliary fermion and boson Green function, given in Equations (4.3), (4.4), (4.10) and (4.11), are solved using a two-time predictor corrector time-stepper developed in [89]. Typically, memory truncations are used to simplify problems of this type. However, such approximations are not applicable here. This is because, the low energy Kondo correlations require very large timescales given by $\tau_K \sim T_K^{-1} \sim 10^3 D^{-1}$. Therefore, memory truncations would artificially suppress Kondo physics and are therefore avoided altogether. This long timescale introduces additional challenges when the initial condition for the time evolution is constructed. Accurately representing the initial heavy-fermion state requires the system to retain a long memory even at early times. To ensure this, the system is first solved in a steady-state while coupled to the fermionic bath, using the DMFT procedure described in Section 2.5. The resulting Green functions are then Fourier transformed into the time domain and used to fill the solution for times $t < t_0 \ll T_0$, where t_0 corresponds to the start of the time evolution. This ensures that the time evolution begins from a fully formed Kondo state. To make the results more interpretable, the two-time Green functions are expressed in Wigner coordinates. They are then Fourier transformed with respect to τ but retain explicit dependence on T. This mixed representation allows for a comparison with equilibrium spectral functions, while still capturing the system's time evolution.

First, the response of the d-electrons to the pump pulse is analyzed in Figure 4.3, which shows the spectral and distribution functions at selected times. In panel Figure 4.3a, long before the pulse, the system remains in thermal equilibrium due to the coupling to the bath. At this point, there is no time evolution, and both the spectral function and the band structure display a well-defined heavy band, as a result of the initialization procedure discussed above. Since the pulse is Gaussian, the system begins to feel its influence before the peak is reached. At this stage, as shown in panel Figure 4.3b, the distribution function shows that high-energy states begin to be populated by the pulse, indicating Kondo decoherence due to heating. At the peak of the pulse, shown in panel Figure 4.3c, the system feels the full influence of the pulse, and is driven far from equilibrium. Moreover, this state is qualitatively different from the Kondo state. This is because the system effectively enters a mixed-valence-like regime, due to an increase of the hybridization strength, which effectively becomes $\Delta \sim V^2 + g^2\bar{n}_a$. This photon-assisted enhancement of the hybridization pushes the system out of the Kondo regime,

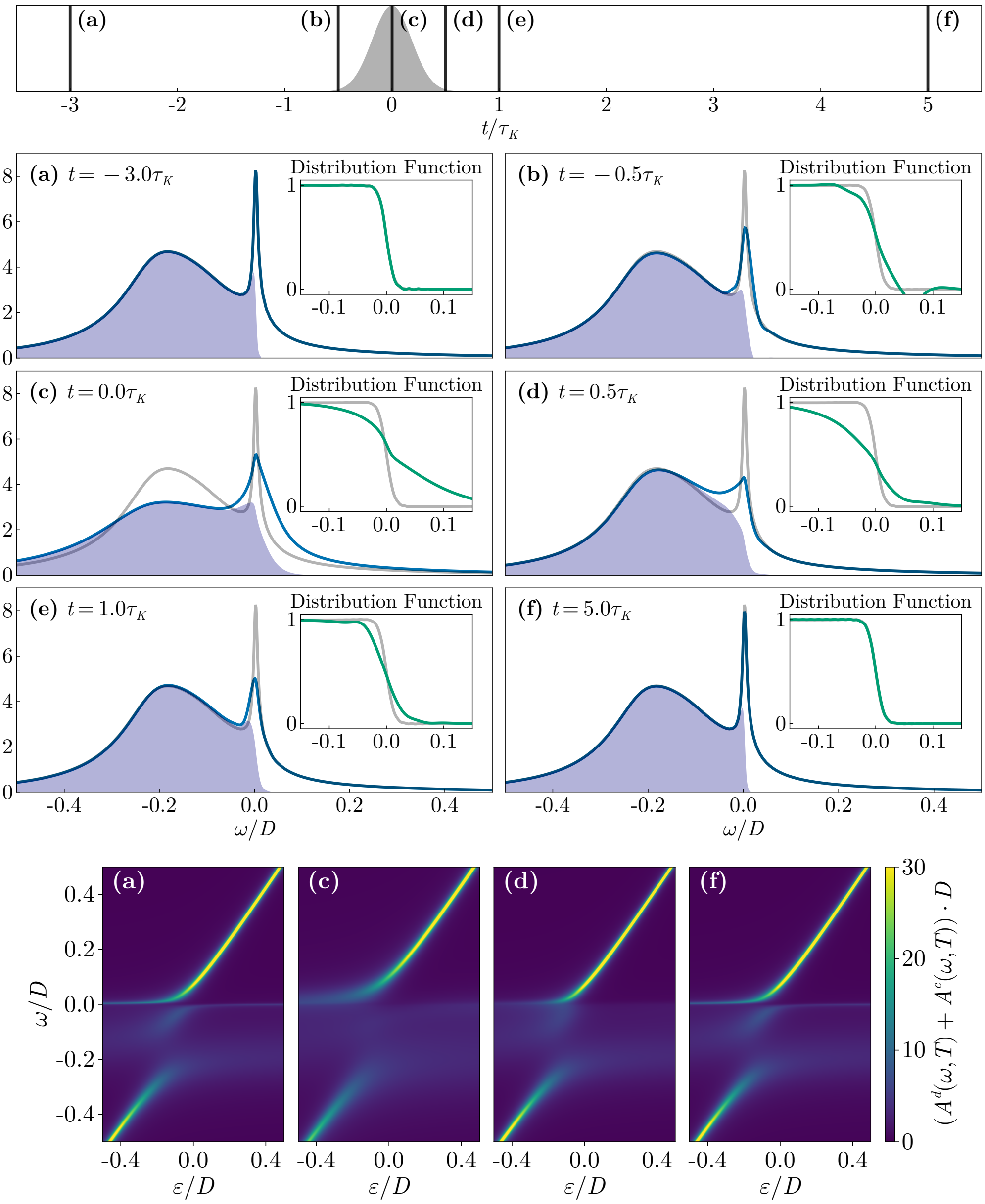

Figure 4.3: Time evolution of the d-electron spectral functions under the influence of the THz pump pulse [103]. The top panel shows the photon pulse profile and defines the timestamps corresponding to panels **(a-f)**. The middle panel shows the local spectral function, and the insets show the corresponding distribution function. The bottom panel shows the band structure. **(a)** Long before the pulse, the system is in the steady-state. **(b)** As the system begins to feel the photon pulse, the Kondo weight is depleted, and high-energy states become populated as seen in the distribution function. **(c)** At maximum pulse intensity, both the single-particle peak and the Kondo peak are strongly suppressed. The heavy band is washed out, indicating the destruction of the Kondo state. **(d)** Shortly after the pulse, the single-particle peak rapidly recovers, while the heavy band has not. **(e)** After the Kondo timescale τ_K, the Kondo peak begins to rebuild. **(f)** Long after the pulse, The heavy band has fully reformed, signaling the revival of the Kondo state. The fermionic parameters used are $\varepsilon_d = -0.175D$, $V = 0.15D$, and $\beta = 300/D$, while the photon pulse parameters are $\omega_0 = 0.0005D$, $\Omega_0 = 0.03D$, $\bar{n}_a = 10$, $g = 0.02D$, and $\gamma = 0.02D$, where D is the bandwidth.

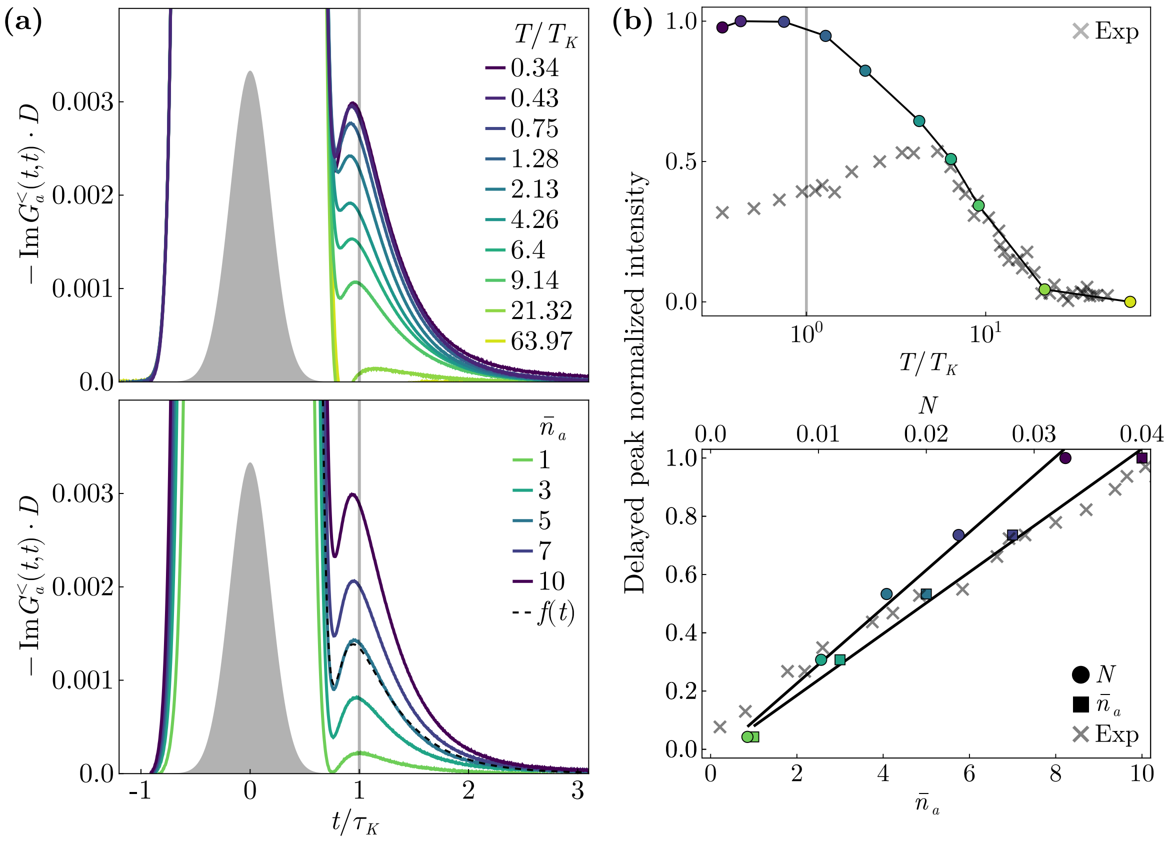

Figure 4.4: **(a)** Time trace of the renormalized photon pulse as a function of temperature and maximum incident pulse intensity. **(b)** The delayed peak normalized intensity as a function of temperature and the fraction of excited electrons N and maximum pulse intensity. The parameters used are the same as in Figure 4.3.

explaining the fast destruction of the Kondo state. The corresponding band structure also reflects this change, since both the heavy band, and the impurity level become washed out. After the pulse, high-energy features recover quickly, as shown in panel Figure 4.3d, the single particle peak recovers almost immediately. However, the Kondo peak requires a much longer time to recover. In panel Figure 4.3e, after approximately one Kondo timescale, the Kondo peak begins to reappear. However, the system still retains excess energy from the pulse, indicated by the hot distribution function, meaning that full Kondo coherence cannot yet be restored. Finally, at long times, shown in panel Figure 4.3f, corresponding to $T \sim 5\tau_K$, the system has fully thermalized and returned to the same Kondo state as before the pump pulse.

Having analyzed the response of the *d*-electrons, attention now shifts to the optical response. The influence of temperature and maximum incident pulse intensity on the renormalized photon pulse is shown in Figure 4.4. In all cases, at short times, a large peak is observed, corresponding to the direct reflection of the incoming Gaussian pulse. A secondary peak, appears at a time $\sim \tau_K$. This is between the timescales corresponding to Figure 4.3(d-e), where the single particle peak has already recovered, but the Kondo peak is still not fully there due to the excess energy that remains in the system. The system removes this energy by emission of photons, which leads to the observed secondary peak. To be able to compare with the experiment, this echo response needs to be isolated, which is done via the fittings shown in Figure 4.5. A direct fitting using a Gaussian for the initial pulse and a sech^2 for the delayed pulse, which is the expected

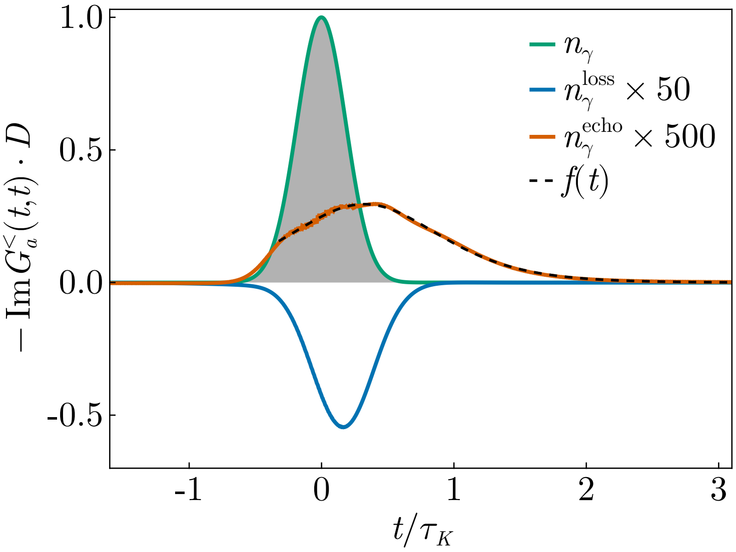

Figure 4.5: Fitting of a typical renormalized photon pulse, with the same parameters as the fitted curve in Figure 4.3. The dark blue curve shows the instantaneous response of the system, which follows a Gaussian shape. The energy loss to the fermionic heat bath also follows a Gaussian shape, indicated by the light blue curve. The red curve represents the remaining signal after subtracting the two previous contributions, displaying the relevant echo pulse. The fitting curve for this echo pulse is given by $f(t) = f_0 \operatorname{sech}\left(2\pi\frac{t-t_0}{\tau}\right)^2$, and results in a delay time $t_0 = 0.85\tau_K$ and width of $\tau = 1.01\tau_K$.

shape obtained from the rate equation, fails to reproduce the response. This is because, there is an additional dissipation channel coupled to the system, namely the fermionic bath. To account for this, an extra Gaussian term with a negative amplitude is included in the fitting procedure. This three-component fit accurately reproduces the shape of the renormalized photon pulse. Moreover, the width of the echo pulse extracted from the fit agrees with the Kondo timescale to within 1%, which agrees with the phenomenological rate equations in [68]. Notably, the height of the echo pulse is only 0.1% of the incoming pulse, reflecting that only a small fraction of the electrons emit photons, consistent with the experimental observations.

Now that the echo pulse has been isolated, the Kondo weight can be computed and analyzed as a function of the parameters. First, its dependence on pulse intensity, and the number of excited particles given by [89]

$$N \approx \max_T \int \frac{d\omega}{2\pi} \sum_\sigma \left[G^>_{c_\sigma}(T,\omega) + G^>_{f_\sigma}(T,\omega) \right], \tag{4.17}$$

is shown in Figure 4.4. Where it can be seen that the Kondo weight has a linear dependence on both of these parameters, strongly supporting the rate equations and ruling out superradiance arguments, where the intensity would scale as N^2 [104]. Next, the weight is plotted as a function of temperature and compared to the experimental data. At high temperatures, the Kondo weight displays a logarithmic increase, in agreement with the experimental observation. Deviations begin to kick in around $T \sim 5T_K$, which suggests that this is where influence from the proximity of the QCP are felt in the experiment. Since the work here does not include any influence from RKKY interactions, this decrease cannot be captured.

4.2 Summary and Outlook

In this chapter, the non-equilibrium response of a heavy-fermion system to a THz pulse has been analyzed within the framework of time-dependent non-equilibrium DMFT. To be able to do that, light-matter interactions which include local effects were added to the Anderson lattice model as was done in Chapter 3. However, unlike there, the frequency of the THz pulse is close to the Kondo temperature. This means that the photon field needs to be treated in a full quantum treatment. To capture the temporal response, the Kadanoff-Baym equations were solved using a two-time predictor-correct scheme [89]. The initial conditions were prepared by readying a steady-state solution and Fourier transforming it into time and using this as data for times much less than the pulse peak, $t \ll T_0$.

This analysis was able to reveal the microscopic mechanism under which the Kondo system undergoes fast destruction and slow reconstruction leading to a secondary pulse. The fast destruction is attributed to the photon-assisted enhancement of the hybridization, driving the system into a mixed-valence regime, which due to the associated high energies, is why the Kondo state is destroyed so fast. After the pulse, the single-particle peak recovers quickly, but the Kondo peak rebuilds on a much longer timescale. The energy injected into the system by the pulse escapes the system in two ways. One is by emission of the photons, which leads to the secondary peak, and the other is via heat transfer with the bath. By utilizing a fitting which incorporates these effects, the Kondo weight can be extracted. The shape and the width of the secondary pulse, which follows a sech^2 function, confirms that this pulse is not merely a simple reflection of the incident pulse, thus confirming its many-body origin. These results demonstrate that THz spectroscopy of heavy-fermion systems, through the measurement of the Kondo induced echo pulse, provides an experimental technique that can directly measure the Kondo quasiparticle weight.

The theoretical techniques discussed in this chapter can be extended to study materials other than $\text{CeCu}_{6-x}\text{Au}_x$. In fact, THz spectroscopy experiments have already been performed on YbRh_2Si_2, revealing fermionic critical slowing down near the quantum phase transition [105]. However, the real challenge lies in incorporating RKKY interactions into the framework to better understand the competition between Kondo screening and magnetic ordering. However, since this task is already extremely challenging in equilibrium, the thought of extending it to non-equilibrium is even more daunting. On a more positive note, these techniques are not restricted to heavy-fermion systems in any way, and can be applied more generally, especially when long time evolutions are required.

Chapter 5

Non-Hermitian Phase Transition in EuO

The field of ultrafast magnetization took off with the seminal work [106], where a magnetic response in nickel was observed in a pump-probe experiment on a picosecond timescale, as shown in Figure 5.1a and 5.1b. This response is orders of magnitude faster than conventional spin dynamics, such as spin wave or magnetization precession, which typically occur on timescales of hundreds of picoseconds, as illustrated in Figure 5.1c. The underlying mechanism for this fast demagnetization was attributed to the pump pulse exciting the electrons, thus driving the system into a highly non-equilibrium state. Through spin-flip scattering processes, facilitated by spin-orbit coupling and electron-phonon interactions, the magnetic coherence is lost, resulting in demagnetization [107]. These spin relaxation processes occur on femto- to picosecond timescales, explaining the ultrafast response of the material. Since then, ultrafast magnetization has been extensively investigated in a variety of materials, both theoretically [108–110] and experimentally [111, 112], leading to significant advancements in both fundamental physics and technology, particularly in spintronics [113]. Recent progress has further expanded the field, enabling the enhancement of the magnetic order [114]. This was achieved in a pump probe experiment on EuO, a ferromagnetic semiconductor in which the spin ordering is governed by the Ruderman–Kittel–Kasuya–Yosida (RKKY) interaction. The excitation of electrons due to the pump increases the RKKY coupling, thereby enhancing spin-ordering.

In general, pump-probe experiments naturally lead to a non-Hermitian response of the system due to the external driving, reflecting the far from equilibrium nature of the system. However, non-Hermitian physics has even gathered attention in equilibrium systems [115, 116]. It is conjectured that quantum systems are described by Hermitian Hamiltonians, ensuring real eigenvalue spectra. However, it was shown that non-Hermitian Hamiltonians which exhibit a parity ($\mathcal{P}$) and a time-reversal ($\mathcal{T}$) symmetries exhibit a purely real spectrum [117, 118]. When these symmetries break down, complex eigenvalues tend to appear, marking a so-called exceptional point[1] at which a non-Hermitian phase transition occurs. Unlike equilibrium phase transitions, characterized by changes in the ground state of the system, a non-Hermitian phase transition describes a fundamental change in the dynamical behavior of the system. Until now, experimental studies of non-Hermitian phase transitions have primarily focused on nanoscale atomic systems [121–123]. Recent pump-probe experiments on EuO, have revealed the first observation of a non-Hermitian phase transition in a bulk condensed matter system, which is the main focus of this chapter. Before analyzing the underlying mechanism responsible for

---

[1] Introduced in physics literature by [119]. In mathematical literature, this point is referred to as a degenerate node [120].

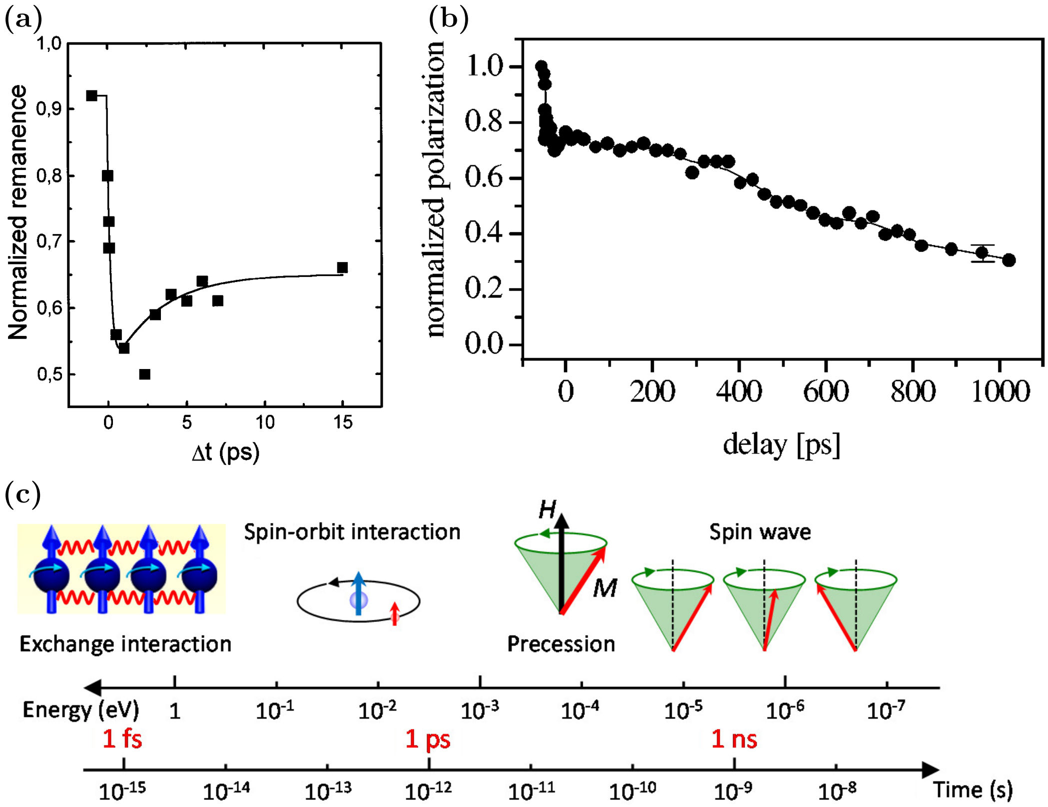

Figure 5.1: Ultrafast spin dynamics in thin films of Nickel measured by pump-probe experiments as a function of the delay time. **(a)** Normalized remanence, which is proportional to the magnetization change, of a 22nm film after excitation with a 60 fs pulse, taken from [106]. **(b)** Normalized spin polarization of the photoemitted electrons in 12Å films after excitation with a 170 fs pulse, modified from [124]. **(c)** Energy and the corresponding time scales associated with certain physical processes, modified from [125].

this transition, it is necessary to first examine the equilibrium properties of EuO and how photodoping affects them.

5.1 Electronic Structure and Magnetism in EuO

EuO is a well-studied material, with extensive research done in the 1960s-1970s [126, 127] and it continues to find applications nowadays in spintronics and theoretical studies [128–130]. EuO undergoes a ferromagnetic transition at a Curie temperature of $T_c = 69K$. As shown in Figure 5.2a, the ferromagnetic transition follows the Curie-Weiss law so well that EuO came to be regarded as a prototypical Heisenberg ferromagnet [131]. In addition, EuO undergoes a simultaneous insulator-to-metal transition at the same critical temperature, as illustrated in Figure 5.2b. In the paramagnetic phase, EuO is a semiconductor with a band gap of 1.2eV. Prior to the discovery of ferromagnetism in EuO, it was widely believed that ferromagnetic semiconductors are unlikely to exist. This is because, in a conventional Fermi liquid, the spins would be screened, resulting in a reduced coupling between the spins that prevents long range magnetic order. These experimental observations in EuO were the first to demonstrate that a ferromagnetic semiconductor can be realized. Another interesting property is that EuO exhibits one of the largest colossal magnetoresistance effects [132], in which the resistivity changes by

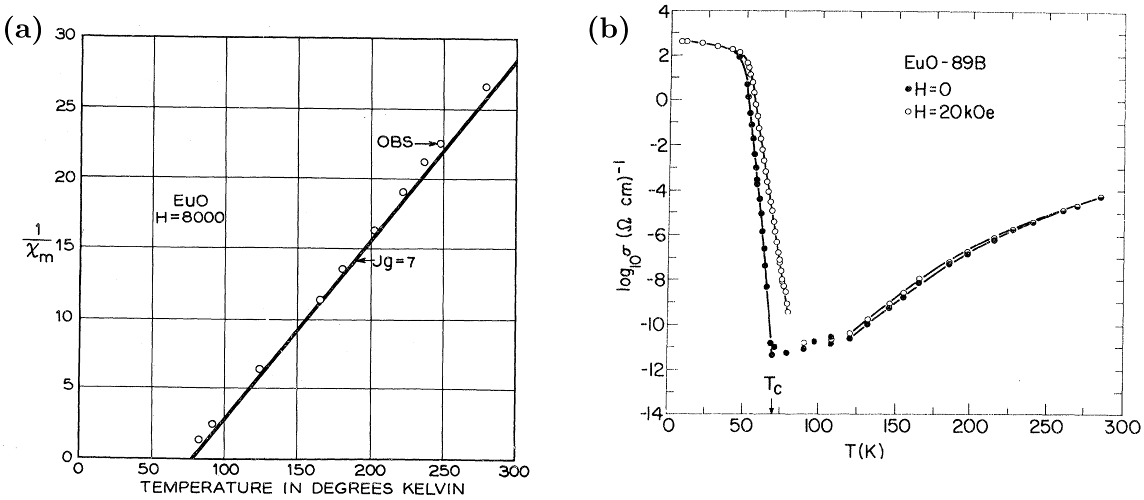

Figure 5.2: Experimental measurements of **(a)** inverse susceptibility [126] and **(b)** conductivity [133] vs temperature for EuO. It is seen that the insulator to metal transition and the ferromagnetic phase transition happen at the same temperature.

several orders of magnitude when an external magnetic field is applied. This is a consequence of the simultaneous insulator-to-metal and the ferromagnetic transitions. When an external magnetic field is applied, the sharp ferromagnetic transition becomes a crossover, effectively making the magnetic field the tuning parameter for the insulator-to-metal transition. Therefore, close to the Curie temperature, the electrical resistivity can change by orders of magnitude.

To understand how all of these properties arise, a microscopic description is needed. The electronic structure of EuO is determined by the valence configurations of europium and oxygen. Europium has an electronic structure of $[\mathrm{Xe}]6s^2 4f^7 5d^0$, while oxygen is characterized by $[\mathrm{He}]2s^2 2p^4$. When EuO is formed, europium donates two electrons from the $6s$ shell to fully occupy the oxygen $2p$ orbitals. EuO crystalizes in a rock salt formation, see Figure 5.3a. The conduction band is formed by hybridized $6s$ and $5d$ band, while the valence band is given by the half-occupied $4f$ band, which lies deep below the Fermi level.

Because of the highly localized nature of the spins in the $4f$ band, the direct exchange coupling alone cannot explain the large Curie temperature of EuO. To explain this, the virtual fluctuations between the $4f$ orbital and the $5d$ orbital need to be taken into account [134]. Due to the extended nature of the $5d$ orbital, these virtual excitons mediate interactions between the spins on different sites, as illustrated in Figure 5.3b. This mechanism enhances the exchange coupling between the spins and thus leads to the large T_C observed experimentally. Due to this, the Hamiltonian for EuO only contains a Heisenberg term

$$H_{\mathrm{EuO}} = -J \sum_{\langle i,j \rangle} \vec{S}_i \cdot \vec{S}_j, \tag{5.1}$$

where $\vec{S}$ corresponds to the spin operator of the half-filled $4f$ band, and J is the effective ferromagnetic coupling strength coming from both direct and exciton-mediated exchange interactions.

Synthesizing high-purity EuO is a challenging task, particularly in early studies where experimental measurements were significantly influenced by sample-dependent variations [136]. Due to this sensitivity, interest arose in whether it would be possible to tune these defects to achieve a higher T_C. One of the most common defects in EuO is the presence of oxygen

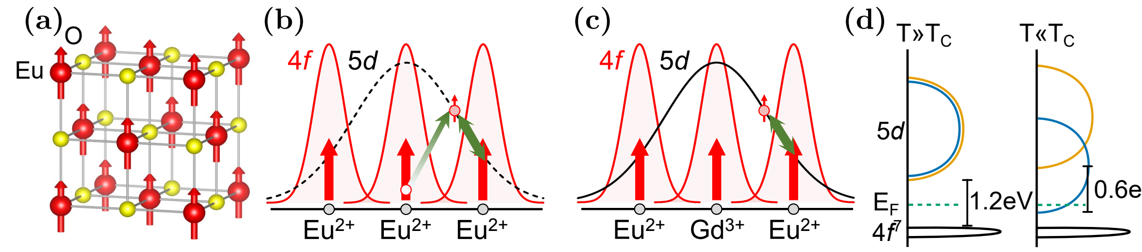

Figure 5.3: **(a)** Rock-salt structure of EuO. The red arrows indicate the spin-polarization of Eu, while O atoms are shown in yellow. **(b)** Illustration of the indirect exchange interaction mediated by virtual fluctuations between the localized $4f$ band and the extended conduction band, given by the dashed line. **(c)** Doping with Gd introduces additional charge carriers, enhancing exchange interactions between Eu spins. All the above figures are taken from [125]. **(d)** Schematic energy level diagram above and below the Curie temperature, showing the semiconducting gap of 1.2eV in the paramagnetic phase, and the Stoner splitting of 0.6eV [135] between the majority and minority band in the ferromagnetic phase.

vacancies, which introduce two electrons from the $6s$ orbital as charge carriers. This enhances the exchange coupling and can lead to an enhancement of T_C [137]. A more controlled approach to tuning T_C is through Gd doping [128, 138]. Since Gd is the next element in the periodic table after Eu, it has an additional electron in it's electronic configuration, given by $[\mathrm{Xe}]6s^2 4f^7 5d^1$. When an Eu atom is replaced with Gd, the additional $5d$ electron acts an extra charge carrier, as illustrated in Figure 5.3b. The key difference between these two types of doping lies in the nature of the donated electrons. While the $6s$ electrons introduced by oxygen vacancies do not carry a local magnetic moment, the $5d$ electrons introduced by Gd do, which can lead to significant differences in their effects on the electronic structure. This was explored in [139], where it was shown that in Gd-doped case, spectral weight at the Fermi level is dynamically generated via the Kondo effect, ultimately driving the system towards a metallic state. Thus, explaining the simultaneous insulator-to-metal and ferromagnetic transition. Furthermore, due to the ferromagnetic ordering, the conduction band is split, meaning that only the majority spin state shifts below the Fermi level, see Figure 5.3c. This also explains the nearly 100% spin polarization observed experimentally [135].

5.1.1 Ferromagnetic Mean Field Theory for EuO

Before addressing non-equilibrium effects, it is useful to first establish a mean-field description of the ferromagnetic transition in EuO. For this purpose, it is convenient to introduce a magnetic field to the Heisenberg model, given by

$$H = -J \sum_{\langle i,j \rangle} \vec{S}_i \cdot \vec{S}_j - B \sum_{i=1}^{N} S_i^z,$$

where B is the magnetic field, chosen to point along the z-axis, and N is the number of spins. In the mean-field approximation, each spin is assumed to experience an average background field, which allows the interaction term to be decomposed as

$$\vec{S}_i \cdot \vec{S}_j \to \vec{S}_i \cdot \left\langle \vec{S}_j \right\rangle = S_i^z \left\langle S^z \right\rangle .$$

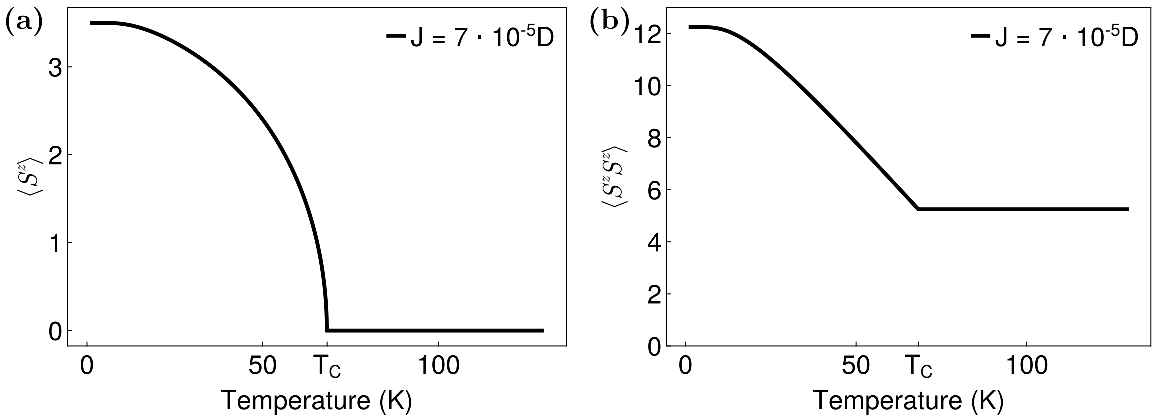

Figure 5.4: Mean-field results for EuO. **(a)** Temperature dependence of the magnetization $\langle S^z \rangle$, where the exchange interaction J was chosen such that $T_c \approx 69$K. **(b)** Temperature dependence of the the spin correlations $\langle S^z S^z \rangle$.

Since the focus is on the ferromagnetic case, it is assumed that the background field also points along the z-axis. Therefore, the mean field Hamiltonian is given by

$$H_{MF} = -(Jz \langle S^z \rangle + B) \sum_i S_i^z$$

where z is the number of nearest neighbors. The single spin partition function is given by

$$Z_i = \sum_{S_i^z=-S}^{S} e^{xS_i^z} = e^{-xS} \sum_{k=0}^{2S} (e^x)^k = \frac{\sinh(x(S+1/2))}{\sinh(x/2)}, \tag{5.2}$$

where $x = \beta(Jz\langle S^z \rangle + B)$. Since the Hamiltonian only depends on a single site, the total partition function is simply given by a product of partition functions for each individual site, leading to $Z = \prod_i Z_i$. Using this, the magnetization per site can be computed as

$$\langle S^z \rangle = \frac{1}{N} \frac{\partial \ln Z}{\partial B}\bigg|_{B\to 0} = \left(S + \frac{1}{2}\right) \coth\left(x\left(S + \frac{1}{2}\right)\right) - \frac{1}{2} \coth\left(\frac{x}{2}\right),$$

which can be related to the well known Brillouin function. Since x depends on $\langle S^z \rangle$, this results in a self-consistent nonlinear equation. Solving this gives the magnetization as a function of temperature, as shown in Figure 5.4, which also shows the spin correlations. In EuO, the local moment has $S = 7/2$, therefore to obtain a Curie temperature of $T_C \approx 69$K, the coupling strength needs to be chosen as $J = 7 \cdot 10^{-5} D \approx 0.56$meV, which agrees well with previous mean-field treatments as well as experimental measurements [140].

5.2 T_C Enhancement via Photodoping

Now that the microscopic properties of EuO and its doping mechanisms have been established in equilibrium, the focus now shifts to exploring how T_C can be enhanced on an ultrafast timescale through non-equilibrium processes. This was explored in a pump-probe experiment [114], where the pump pulse generates additional charge carriers via photodoping, thereby enhancing the exchange coupling. To probe the magnetic response, the second harmonic generation (SHG) technique was utilized, where reflected light is measured at twice the frequency of the incident light. The SHG signal is highly sensitive to selection rules coming from the crystal symmetry of the material and the light-matter interaction. As a result, SHG has become a well-established method for studying magnetic order in many materials [141]. In centrosymmetric materials, like EuO, SHG is normally forbidden [142]. However, magnetic order can break inversion symmetry, allowing a magnetically induced SHG (MSHG) signal to emerge. This makes MSHG a direct probe of the magnetic order. By expanding the susceptibility to incorporate the non-linear terms, it can be shown that intensity of the SHG signal follows $I^{MSHG} \propto (JM)^2$ [114], where M is the magnetization. Since the experiment is performed deep in the ferromagnetic regime, where M is fully saturated, variations in I^{MSHG} can be directly related to changes in the exchange coupling.

The static I^{MSHG} is shown as a function of the carrier density induced by Gd doping in Figure 5.5a. This is then compared to the corresponding T_C obtained in [138], showing good agreement and confirming that MSHG quantitatively measures the magnetic order. The relative change of the MSHG intensity after the sample is excited by a pump pulse, and the theoretical prediction of the change of the exchange coupling is shown in Figure 5.5b. These two quantities are directly comparable since $\Delta J/J = \Delta I^{MSHG}/(2I^{MSHG})$. The pump induces a change in the carrier density of approximately 10^{19} cm^{-3}, and the MSHG intensity is measured with a probe pulse shortly after the pump excitation, with a delay time of $\Delta t = 3$ps, demonstrating the ultrafast magnetic response. For Gd induced carrier densities $\lesssim 10^{18}$ cm^{-3}, the exchange coupling does not change. This is because, in this regime, the exchange coupling is dominated by photodoping, and the Gd doping acts as a small perturbation. However, as the Gd doping is increased, which also increases the carrier density, an enhancement of the exchange coupling is observed due to the combined effects of photodoping and Gd substitution. When the Gd concentration is too high, photodoping instead results in a reduction of the exchange coupling. This is because, at this point, the Gd concentration exceeds 10%, leading to significant modifications in the band structure. As a result, the increased energy mismatch between the bandgap and the pump energy reduces the efficiency of carrier excitations [114].

5.3 Non-Hermitian Phase Transition in EuO

In this section, the observation of a non-Hermitian phase transition in EuO is discussed. Such phase transitions have not been previously considered in bulk condensed-matter systems due to the highly specific non-equilibrium conditions required, which were considered to be too difficult to achieve experimentally. Before describing the experimental findings and their interpretation, it is instructive to first gain intuition by considering a simple example which illustrates such a phase transition.

One such example is the damped harmonic oscillator, whose dimensionless equation of motion is given by

$$\ddot{x} + \mu\dot{x} + x = 0, \tag{5.3}$$

where x describes the displacement and μ is the dimensionless damping. The non-Hermitian nature of this system is due to the presence of the dissipative term $\mu\dot{x}$. Introducing the velocity $v = \dot{x}$, the system can be rewritten as a set of two linear first-order differential equations, which can be written in a compact matrix form as

$$\begin{pmatrix} \dot{x} \\ \dot{v} \end{pmatrix} = \begin{pmatrix} 0 & 1 \\ -1 & -\mu \end{pmatrix} \begin{pmatrix} x \\ v \end{pmatrix}. \tag{5.4}$$

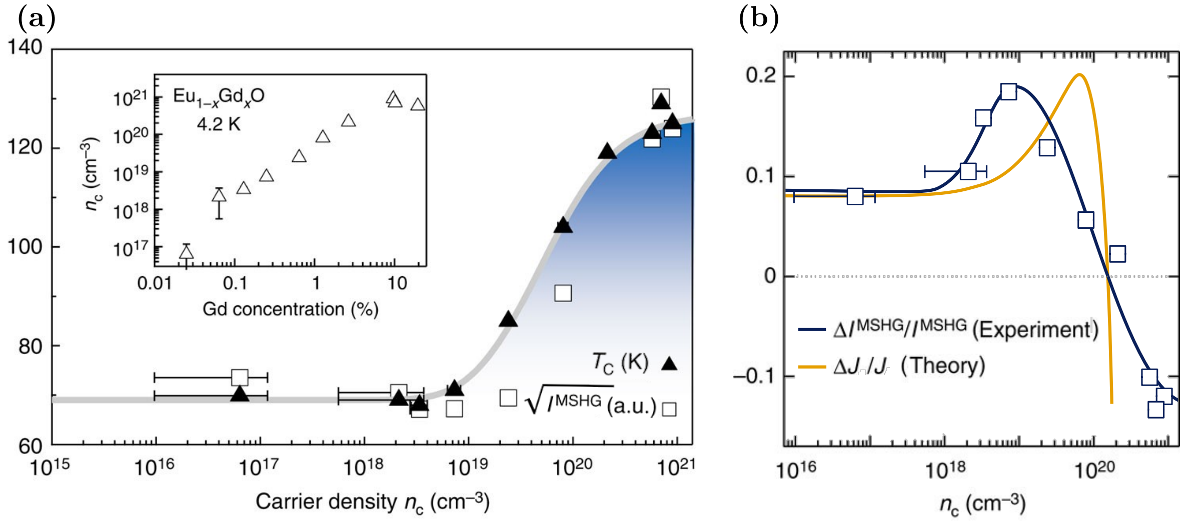

Figure 5.5: **(a)** Dependence of T_C (data from [138]), and the square root of the static I^{MSHG} on the carrier density n_c in Eu$_{1-x}$Gd$_x$O. The inset shows n_c as a function of Gd concentration. **(b)** Relative change of MSHG intensity, defined as $\Delta I^{MSHG}/I^{MSHG} = (I^{MSHG}(\Delta t) - I^{MSHG})/I^{MSHG}$, measured at $\Delta t = 3$ps and $T = 10K$, alongside the theoretical prediction for the relative change of the exchange coupling. Both are plotted as a function of the carrier density induced by Gd doping. Both images are adapted from [114].

This matrix is explicitly non-Hermitian, meaning that its eigenvalues can, in general, be complex. These eigenvalues dictate the dynamical behavior of the system, since the general solution for $x(t)$ is given by

$$x(t) = Ae^{\gamma_+ t} + Be^{\gamma_- t}, \quad \text{where} \quad \gamma_\pm = -\frac{\mu}{2} \pm \frac{1}{2}\sqrt{\mu^2 - 4}, \tag{5.5}$$

are the eigenvalues of the matrix in Equation (5.4). For $|\mu| < 2$, the eigenvalues form a complex conjugate pair, resulting in a damped oscillatory motion where the imaginary part corresponds to the oscillation frequency and the real part to the decay rate. In contrast, when $|\mu| > 2$, the eigenvalues are purely real, leading to a bi-exponential decay with two distinct decay rates. These two regimes represent fundamentally different types of dynamical behavior. To move from one regime to the other, the system must pass through what is known as an exceptional point. At the exceptional point, which occurs when $|\mu| = 2$, the eigenvalues become degenerate, and it can be easily verified that the solution takes on the form

$$x(t) = (A + Bt)e^{-\frac{\mu}{2}t}. \tag{5.6}$$

Moreover, at this point, the system can no longer be diagonalized, leading to a coalescence of the eigenvectors. Physically, this means that two distinct dynamical modes collapse into a single one. When exactly two modes coalesce, this is referred to as a second-order exceptional point, which are the most common ones studied. However, higher-order exceptional points, where more than two eigenvectors coalesce, have also been studied both theoretically and experimentally [143, 144]. An important aspect is that any non-Hermitian phase transition can be mapped onto this simple example or its higher order extensions. A key signature of the presence of an exceptional point is that, in its vicinity, the eigenvalues exhibit an n-root dependence on the tuning parameter, where n is the order of the exceptional point. In the case of the damped harmonic oscillator, this corresponds to a square-root behavior, which is clearly seen in Equation (5.5) and Figure 5.6.

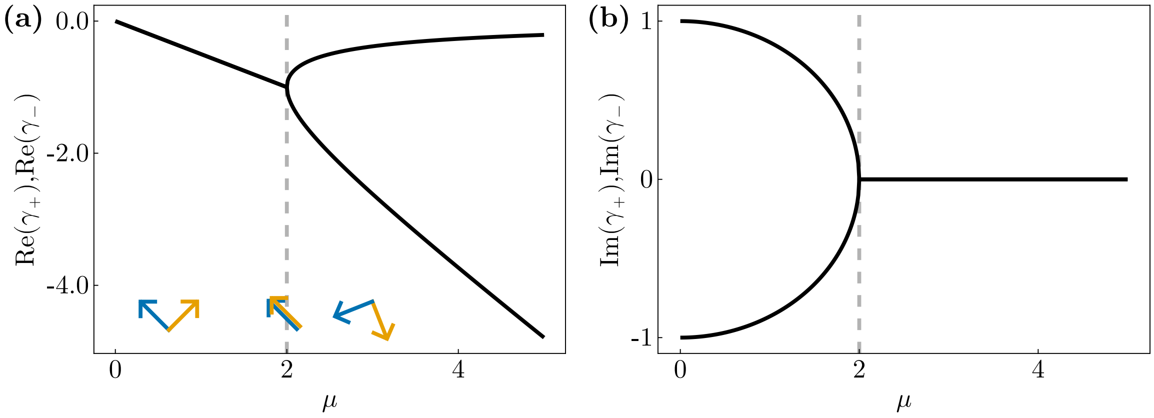

Figure 5.6: Eigenvalues of the damped harmonic oscillator as a function of the dimensionless damping μ, with the exceptional point marked by the dashed line. **(a)** The real part, with an illustration of the eigenvectors coalescing at the exceptional point. **(b)** The imaginary part, showing the signature square root behavior.

5.3.1 Experimental Observations

Now, the experiment in EuO that has been alluded to up until now is finally discussed. The schematic of the experimental setup is shown in Figure 5.7a. The pump consists of a 120fs pulse with an energy of 1.55eV and a fluence of 100μJ/cm^2. The system is then probed using 120fs pulses at 1.31eV across various temperatures, covering both the paramagnetic as well as the ferromagnetic phase of EuO, as shown in Figure 5.7b.

The reflectivity is proportional to the number of charge carriers in the system. Due to the charger carrier excitation caused by the pump, for all temperatures, the reflectivity increases at first and peaks within the duration of pump pulse. After this peak, two distinct behaviors are observed depending on the temperature regime. At low temperatures, a bi-exponential decay is observed, which plateaus to a positive value, see top panel in figure 5.7c. This indicates that the optically induced charge carriers are stabilized, which is attributed to a photo-assisted increase in the exchange coupling. This pushes the majority conduction band deeper below the Fermi level, stabilizing the pump induced charger carriers. On very long timescales, the system must eventually return to its original state. In contrast, at high temperatures, the initial reflectivity peak is followed by a rapid decay, reaching a negative change in the reflectivity before settling to $\Delta R = 0$, see bottom panel in figure 5.7c. The transition between these two behaviors occurs at a temperature $T^* = 84 \pm 5$K.

There are a variety of phenomena known to cause a negative dynamic response, with two of most common mechanisms found in the ultrafast magnetization literature being coherent photons [145] and Auger recombination [146, 147]. However, neither of these mechanism capture the observed behavior seen in this system. Coherent phonons corresponds to the process where optically excited phonons and the charge carriers exchange energy with each other leading to oscillations in the reflectivity data. The relevant optical phonons in EuO are on the eV scale [148], which would lead to much faster oscillations in the reflectivity response, whereas in this case, the oscillations occur on a timescale of approximately 10ps. Moreover, since this is an intrinsic energy scale this should not be a temperature dependent effect. Auger recombination corresponds to a non-radiative process where the recombination of an electron and a hole leads to an excitation of another electron to a higher energy state. Thus reducing the amount of charge carriers which leads to a reduction in the reflectivity. This process is unlikely to happen

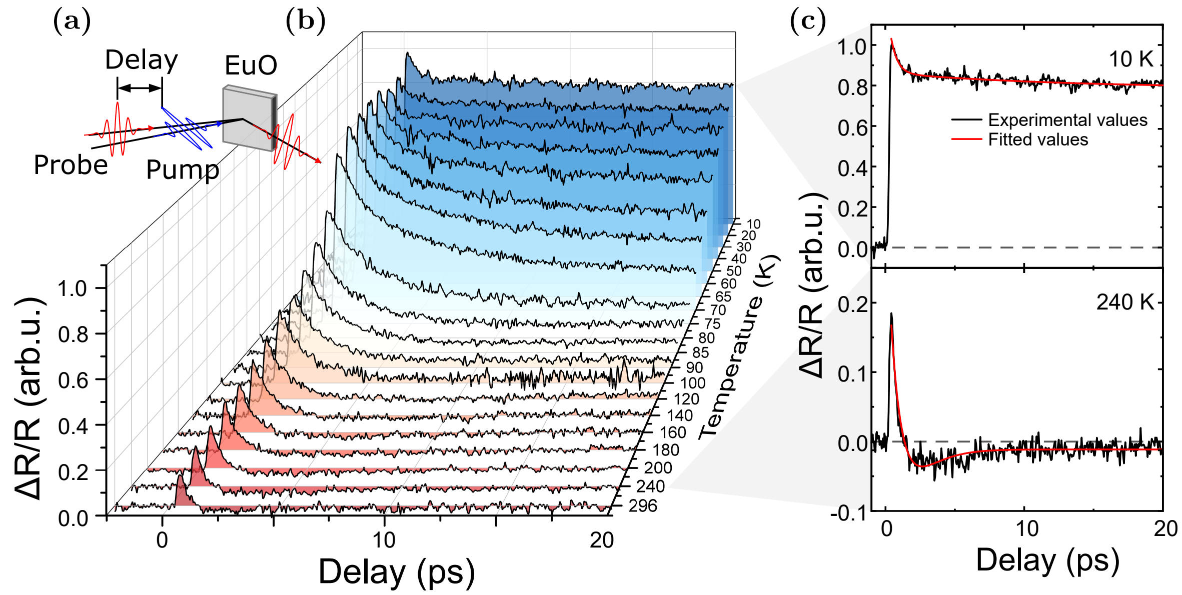

Figure 5.7: **(a)** Schematic of the pump-probe experiment on EuO, where a pump pulse excites the system, and a time-delayed probe pulse measures the reflectivity change. **(b)** Temperature-dependent relative change of the reflectivity normalized by the reflectivity of the non-pumped system as a function of delay time. The color gradient represents increasing temperatures from 10K (blue) to 296K (red) **(c)** Two distinct relaxation behaviors: at low temperatures (top panel), a bi-exponential decay that eventually plateaus to a constant value is observed, while at high temperatures (bottom panel), damped oscillations which eventually decay to $\Delta R = 0$ are observed. The figures are taken from [9]

in this system because the fluence of the pump pulse is not large enough for second order effects to dominate, and are expected to be insignificant. Despite this, great efforts have been put in to attempt to fit the experimental results using these and other possible mechanism, none of which were able to reproduce the observed behavior, see [149]. In particular, none of the above effects can explain the existence of a critical temperature $T^* > T_C$, beyond which a negative response occurs.

Having thus excluded previously known physical explanations, the focus now shifts to demonstrating that the system dynamics exhibit the unique signatures of a non-Hermitian phase transition. Based on the shape of the reflectivity data, the low temperature regime is well described by a bi-exponential fit

$$\frac{\Delta R}{R} = A_1 e^{-t/\tau_{\text{slow}}} + A_2 e^{-t/\tau_{\text{fast}}} + c, \tag{5.7}$$

where $A_{1,2}$ are the amplitudes of the slow and fast decaying components, with decay rates of τ_{slow} and τ_{fast}, respectively, and c is the offset that accounts for the long-time plateau. At high temperatures, the reflectivity is well captured by the damped oscillatory fit

$$\frac{\Delta R}{R} = -A e^{-t/\tau} \sin\big(\gamma'' t + \phi\big), \tag{5.8}$$

where γ'' is the imaginary part of the eigenvalue which corresponds to the oscillation frequency, and ϕ is a phase shift. The fits for both regimes are shown in Figure 5.8.

At low temperatures, the bi-exponential behavior is clearly visible in Figure 5.8a. As the temperature increases, the two decay rates come closer together and eventually merge

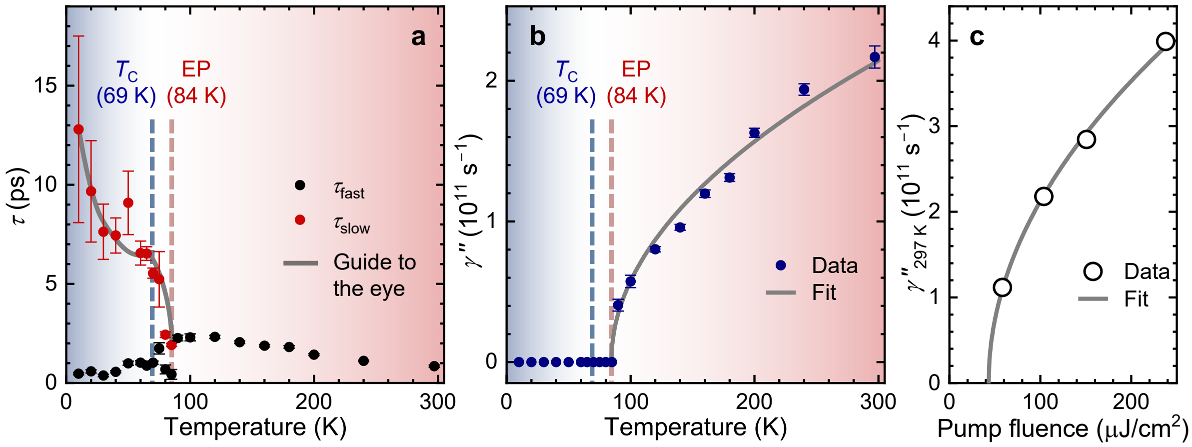

Figure 5.8: Fitting Equations (5.7) and (5.8) to the data in Figure 5.7 as a function of temperature. **(a)** Relaxation times extracted from the bi-exponential and damped oscillatory regimes. In the bi-exponential regime, two relaxation times are observed τ_{fast} (black) and τ_{slow} (red), while in the damped oscillatory regime, only a single relaxation time τ is present. **(b)** Imaginary part of the eigenvalue γ'', which becomes nonzero at the exceptional point around $T^* = 84K \pm 3$K. This agrees with the temperature at which the two real decay rates merge. **(c)** γ'' at $T = 297$K as a function of the pump fluence. The observed square-root dependence on temperature **(b)** and fluence **(c)** provides a smoking gun signature of the presence of an exceptional point. The figures are taken from [9].

at $T^* \approx 85$K. Precisely at this point, γ'' acquires a non-zero value, see Figure 5.8b. Beyond this point, only a single decay rate remains, and γ'' follows a square-root dependence on the temperature, scaling as $\gamma'' \sim \sqrt{T - T^*}$. In Figure 5.8c, the pump fluence dependence is analyzed, by plotting γ'' at $T = 297$K as a function of the pump fluence, yielding a similar square-root dependence $\gamma'' \sim \sqrt{P - P^*}$, where P^* represents the critical pumping threshold. This characteristic square-root scaling is a smoking gun evidence of a second-order exceptional point, marking the presence of a temperature-dependent non-Hermitian phase transition in EuO.

5.3.2 Exciton model

To construct a theoretical framework, it is first necessary to figure out the relevant degrees of freedom present in the system. When a pump pulse excites an electron from the $4f$ shell into the conduction band, it leaves behind a hole, forming an electron-hole pair that constitutes a spin 0 exciton [150]. When this electron-hole pair recombines, it emits a photon which is then measured in the reflectivity change. Due to this, these excitons are referred to as bright excitons. The spin interactions with the remaining $4f$ electrons can lead to the formation of higher-spin excitonic states with spin ± 1. These states do not contribute to the reflectivity change, because photon emission does not conserve spin. Due to this, they are referred to as dark excitons. The negative reflectivity response observed in the high temperature regime is thus attributed to the conversion of bright excitons into dark excitons, reducing the number of optically observable states. However, the conversion from bright to dark excitons requires overcoming the excitation energy of the dark excitons, which is provided by the availability of a background phonon bath. Taking these effects, which are illustrated in Figure 5.9, into

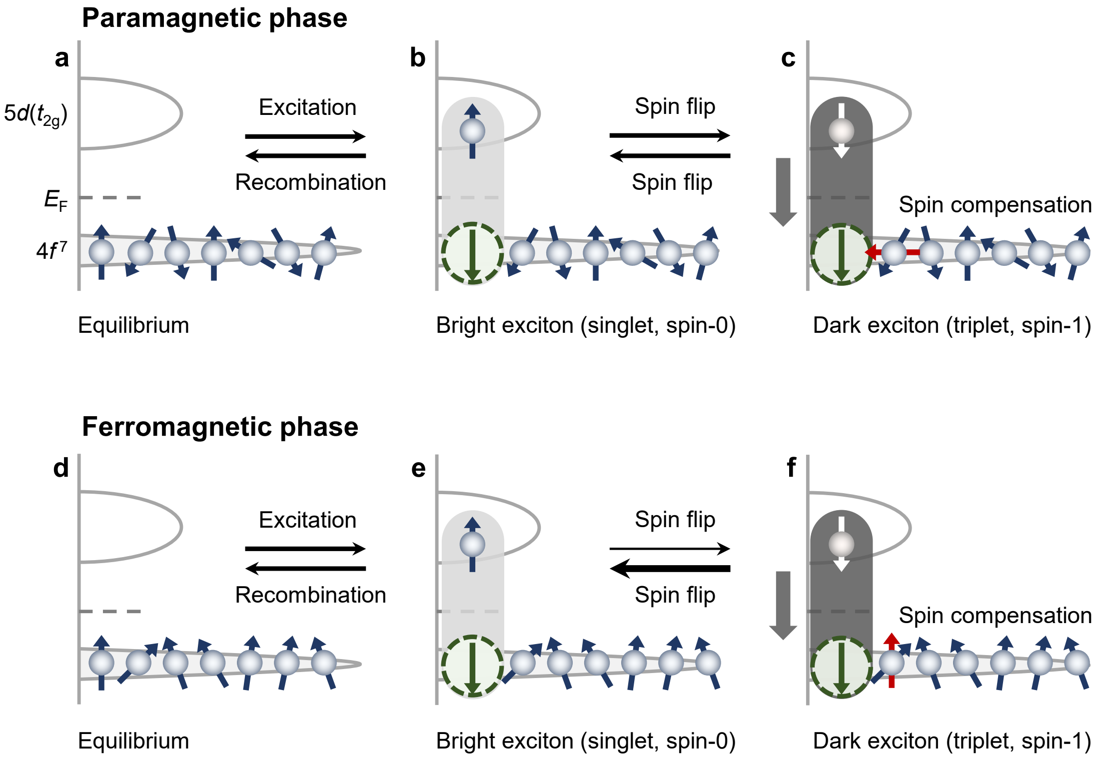

Figure 5.9: Schematic of the spin and exciton processes present in EuO for the paramagnetic phase **(a-c)** and the ferromagnetic phase **(d-f)**. **(a)** In equilibrium the $4f$ spins are randomly oriented. Upon excitation, **(b)** a bright exciton forms. This bright exciton can transform into a dark exciton **(c)** through spin-exchange, and vice versa. **(d-f)** In the ferromagnetic phase, the $4f$ spins are aligned, breaking the symmetry of the exciton transformation process. As a result, one of the dark exciton states becomes energetically unfavorable, leading to an asymmetry in the transition rates, indicated by the arrow thickness. The figures are taken from [9].

account, the effective exciton Hamiltonian is given by

$$H = H_{\text{EuO}} + \sum_{m=\pm1} \Omega_m a_m^\dagger a_m + \sum_k \varepsilon_k b_k^\dagger b_k + J_{df} \sum_{m=\pm1,k} (b_k + b_k^\dagger) \left[a_m^\dagger a_0 S^{-m} + a_0^\dagger a_m S^m \right], \tag{5.9}$$

where $a_m^\dagger$ is the creation operator of an exciton with spin m, and Ω_m is the excitation energy of a dark exciton relative to a bright exciton. The phonon creation operator is given by $b_k^\dagger$, with ε_k being the phonon dispersion relation. The coupling constant J_{df} describes the phonon-assisted conversion of bright exciton into dark exciton, mediated by spin compensation from the $4f$ moments [151]. Since the phonon energy scale is of the order eV [148], the phonon system is treated as a thermal Markovian bath at the cryostat temperature, with its effects incorporated using the Lindblad formalism, see Section 1.1.

The population of bright excitons by the pumping laser pulse, and their loss due to electron-hole recombination are described by the following Lindblad operators

$$PL[a_0^\dagger] \quad RL[a_0]. \tag{5.10}$$

While phonon-assisted transitions between bright and dark excitons, after integrating out the phonon bath, are given by the following jump operators

$$\sum_{m=\pm 1} \Gamma_m^+ L[a_m^\dagger a_0 S^{-m}] \quad \sum_{m=\pm 1} \Gamma_m^- L[a_0^\dagger a_m S^{m}], \tag{5.11}$$

where the temperature-dependent couplings are given by

$$\Gamma_m^+(T) = \frac{{J_{df}}^2}{2} N_{\text{ph}}(\Omega_m)\, B(\Omega_m), \qquad \Gamma_m^-(T) = \frac{{J_{df}}^2}{2} N_{\text{ph}}(\Omega_m)\, [1 + B(\Omega_m)] \ , \tag{5.12}$$

where B is the Bose distribution at the cryostat temperature T, and N_{ph} is the phonon spectral density. Due to the Kennard-Stepanov relation, these obey the $\Gamma_m^+/\Gamma_m^- = e^{-\beta\Omega_m} \ll 1$.

With the exciton model established, the equations of motions can now be constructed using the Lindblad formalism. Specifically, the equations of motion for the density of bright and dark excitons as well as the spin orientations S^z, which are given by

$$\begin{aligned} \frac{dn_0}{dt} = P(1+n_0) - Rn_0 - \Gamma_1^+ \langle S^+S^-\rangle\, (1+n_1)\, n_0 - \Gamma_{-1}^+ \langle S^-S^+\rangle\, (1+n_{-1})\, n_0 \\ + \Gamma_1^- \langle S^-S^+\rangle\, (1+n_0)\, n_1 + \Gamma_{-1}^- \langle S^+S^-\rangle\, (1+n_0)\, n_{-1} \end{aligned} \tag{5.13}$$

$$\frac{dn_1}{dt} = -\Gamma_1^- \langle S^-S^+\rangle\, (1+n_0)\, n_1 + \Gamma_1^+ \langle S^+S^-\rangle\, (1+n_1)\, n_0 \tag{5.14}$$

$$\frac{dn_{-1}}{dt} = -\Gamma_{-1}^- \langle S^+S^-\rangle\, (1+n_0)\, n_{-1} + \Gamma_{-1}^+ \langle S^-S^+\rangle\, (1+n_{-1})\, n_0 \tag{5.15}$$

$$\begin{aligned} \frac{dS_z}{dt} = -\Gamma_1^+ \langle S^+S^-\rangle\, (1+n_1)\, n_0 + \Gamma_{-1}^+ \langle S^-S^+\rangle\, (1+n_{-1})\, n_0 \\ - \Gamma_{-1}^- \langle S^+S^-\rangle\, (1+n_0)\, n_{-1} + \Gamma_1^- \langle S^-S^+\rangle\, (1+n_0)\, n_1, \end{aligned} \tag{5.16}$$

where $n_m = \langle a_m^\dagger a_m\rangle$ is the exciton density and the spin correlation function is given by $\langle S^\pm S^\mp\rangle = S(S+1) - \langle S^z S^z\rangle \pm \langle S^z\rangle$. These equations of motion conserve the total magnetization, given by $d(n_1 - n_{-1} + S^z)/dt = 0$.

To analyze the relaxation dynamics of the system, the equations of motion are expanded to linear order in the deviations of n_m and S^z from their peak values, $\overline{n}_m$, after excitation by the initial pump pulse. Since this expansions is performed around the initial peak, where the pump has already vanished, the pump term does not appear in the relaxation equations. In principle, these equations can be considerably simplified in the paramagnetic phase. Since $\langle S^z\rangle = 0$, the populations of the two dark excitons are equal, such that $n_1 = n_{-1} \equiv n_d$. Due to the conservation of total magnetization, this implies that $S^z = 0$ throughout the time evolution. As a result, the spin correlation remains constant, $\langle S^\pm S^\mp\rangle = \mathit{const}$ and $\Gamma_1^\pm = \Gamma_{-1}^\pm \equiv \Gamma^\pm$. Thus, the system is effectively reduced to only two degrees of freedom, given by the simplified equations of motion

$$\frac{dn_0}{dt} = -Rn_0 - 2\Gamma^+ \langle S^+S^-\rangle\, (1+n_d)\, n_0 + 2\Gamma^- \langle S^-S^+\rangle\, (1+n_0)\, n_1 \tag{5.17}$$

$$\frac{dn_d}{dt} = -\Gamma^- \langle S^-S^+\rangle\, (1+n_0)\, n_d + \Gamma^+ \langle S^+S^-\rangle\, (1+n_d)\, n_0. \tag{5.18}$$

Since the non-Hermitian phase transition occurs in the paramagnetic regime, this reduced framework provides a compact formulation for its analysis. However, in this work, the aim is to explore the behavior in the ferromagnetic regime as well, where the dark exciton states are no longer degenerate and their populations differ. Therefore, to fully capture the non-Hermitian phase transition as well as the ferromagnetic transitions, all four degrees of freedom are retained. The two eigenvalues which display the non-Hermitian phase transition are displayed as a function

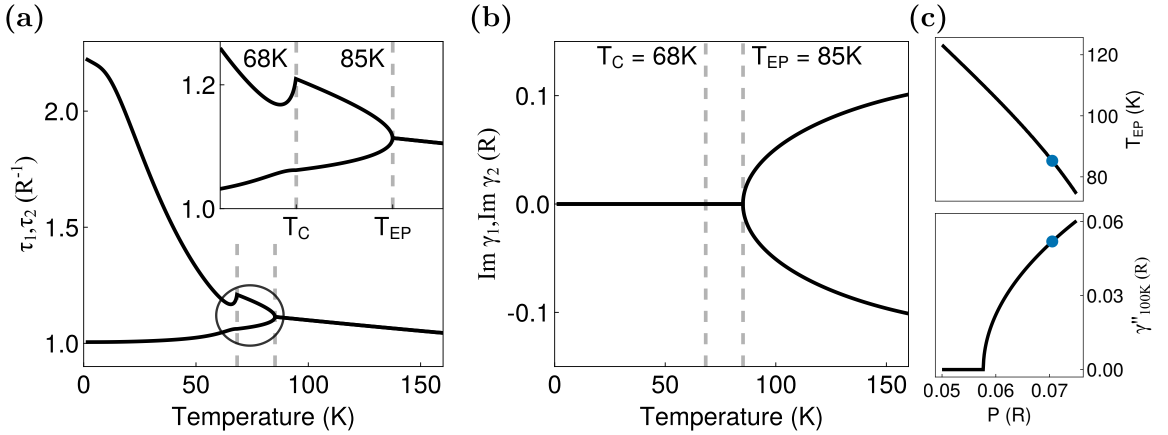

Figure 5.10: The eigenvalues of the linearized system as a function of temperature. The parameters used are $\overline{n}_0 = 0.07$, $\overline{n_{-1}} = \overline{n_1} = 0.25\overline{n}_0$, $\Gamma^- = (0.06 + 6.9 \times 10^{-4} k_B T/R)R$ and $\Gamma^+ = \Gamma_-/100$. $\langle S^z S^z \rangle$ is obtained from the mean-field analysis of EuO. The inset shows a zoomed in region close to the exceptional point, displaying a distinct kink at the Curie temperature.

of temperature in Figure 5.10. Typically, in Lindblad systems the temperature dependence only comes from the explicit temperature dependence of the coupling constants, given in Equation (5.12). In this case, there is an additional temperature dependence coming from the spin correlation term $\langle S^z S^z \rangle$, whose temperature dependence is obtained from a mean-field analysis of EuO, see Section 5.1.1. The eigenvalues show a remarkable agreement with the experimental observed relaxation rates, as seen in Figure 5.8. The square-root dependence of the relaxation rates on both the temperature and on the pump fluence, is well captured. Indicating that the exciton model provides a convincing explanation of the observed behavior. Additionally, a key feature reproduced by this model is the discontinuity in the relaxation rates at the Curie temperature. This discontinuity arises from the fact that, in the mean-field description, the magnetization exhibits a sharp change at the Curie temperature. Since the eigenvalues are directly dependent on these results, a sharp change should also appear in the relaxation rates, further validating the theoretical approach.

5.4 Summary and Outlook

In this chapter, the first observation of a non-Hermitian phase transition in a bulk condensed-matter system was presented, based on pump-probe experiments on EuO. The experiment measured the change in the reflectivity before and after a pump, which excited the system into a far-from-equilibrium state. The subsequent relaxation dynamics to the equilibrium, exhibited a transition between two distinct regimes a bi-exponential decay at low temperatures and a damped oscillatory behavior at higher temperatures, where the change in reflectivity becomes negative. The transition temperature, T^*, was found to be above the Curie temperature. None of the so far known phenomenona could explain the critical temperature at which the negative reflectivity would occur and the temperature and pump fluence dependence of the relaxation rates. The observed dynamics were shown to be consistent with the presence of an exceptional point, as evidenced by the smoking gun square-root dependence of the relaxation rates on the tuning parameters, which in this case are the temperature and the pump fluence.

Despite originating from the same microscopic coupling mechanism, the ferromagnetic

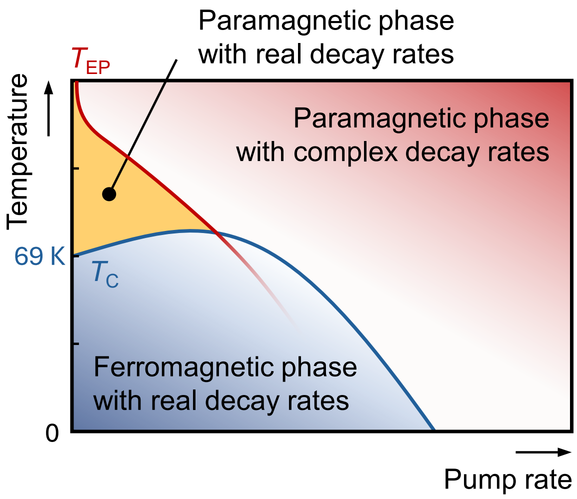

Figure 5.11: Phase diagram of the different equilibrium phases and non-Hermitian dynamics for EuO. The increase in T_C comes from Section 5.2. The experimentally relevant parameters are towards the lower pump rate.

transition and the non-Hermitian phase transition represent distinct physical phenomena, which therefore can occur at different critical temperatures. To provide a theoretical interpretation of these results, an exciton model was developed, which incorporated bright and dark exciton states that form in EuO after optical excitation, with transitions mediated by phonon absorption and emission. The phonon bath was treated as a thermal Markovian bath, and integrated out using the Lindblad formalism. Linearizing the resulting Lindblad equations around the non-equilibrium state induced by the pump pulse successfully reproduced the experimentally observed relaxation rates. Importantly, this model also captured the discontinuity in the relaxation rates at the Curie temperature, further validating the theoretical interpretation.

These findings can be incorporated into a broader understanding of photo-induced phenomena in EuO, particularly in connection with the T_C enhancement via photodoping discussed in Section 5.2. A cartoon phase diagram is proposed in Figure 5.11, illustrating the differences between the equilibrium ferromagnetic transition, as a function of temperature and the novel non-Hermitian phase transition, as a function of pump rate, which acts as a measure of the system's "distance" from equilibrium. The generality of the exciton model suggests that non-Hermitian phase transitions can occur in a wide variety of materials where two coupled dynamical variables interact via a third mode. Meaning that non-Hermitian phase transitions can be realized for a large class of condensed-matter systems, potentially allowing for novel ways to sensitively control bulk-dynamic properties.

Several key questions remain open. First, while the linearization procedure was performed around a physically relevant point, a systematic method for determining the non-equilibrium steady state that the pump pulse pushes the system into is desirable. However, the Lindblad formalism, being agnostic to band structure details is probably not good enough. Therefore, to be able to further analyze this system, a more detailed microscopic model as well as a better non-equilibrium treatment is essential. Given the complexity introduced by the local moments, ferromagnetic ordering, photon and phonon couplings developing such a framework is extremely challenging, yet a crucial task for future work. This need is emphasized by the break down of the exciton picture in the ferromagnetic regime. This is due to the simultaneous insulator-to-metal transition. In a metal system, the concept of excitons is no longer valid, suggesting that the model is not valid below the Curie temperature.

On the experimental side, an intriguing possibility arises from the fact that both T_C and T^* are tunable. An interesting questions is whether it is possible to realize a system, whether in EuO or another material, where these two temperatures can be made to coincide. If achievable, this would lead to a highly nontrivial interplay between critical fluctuations from the ferromagnetic transition and the non-Hermitian dynamics associated with the exceptional point [152], potentially revealing novel dynamical phenomena.

Chapter 6

Photon Bose-Einstein Condensate

Bose-Einstein condensation (BEC) is a fundamental phenomenon where a gas of bosons macroscopically occupies the lowest-energy state at sufficiently low temperatures, due to quantum statistics. Realizations of BECs have been achieved in various systems, including dilute atomic gases [153, 154], and later on also in bosonic quasiparticles [155–158]. Despite being bosons, photons do not undergo condensation due to two fundamental problems. First, since photons are gauge bosons of the electromagnetic force, they do not have a fixed particle number. Second, photons are massless, meaning they do not possess a well-defined ground state into which they can accumulate and form a BEC. A further complication arises in defining the temperature for a photon gas. Unlike massive bosons, whose temperature is determined by the average kinetic energy of particle collisions, photons do not interact with each other in this way. Instead, their thermalization is governed by absorption and emission processes with matter, which dictate both the temperature and the total particle number. This means that the photon gas can only acquire a well-defined temperature relative to a thermal bath.

These challenges were overcome experimentally by trapping photons in an optical microcavity filled with a fluorescent dye medium that is subjected to an external laser-pump [159]. The laser primarily excites high-lying molecular states, which rapidly decay and dephase. Furthermore, since the pump laser does not couple directly to the cavity modes, there is no back-action that would maintain coherence. Together, these effects result in an effectively incoherent pumping process. When a dye molecule, with a complex electronic structures, see Figure 6.1, absorbs a cavity photon, it undergoes a fast relaxation due to multiple absorption and emission cycles with the vibrational modes. Therefore, the dye molecules quickly thermalize with the solvent, typically at room temperature, leading to a thermal absorption and emission spectra of the dye molecules. Thus the dye medium serves as a thermal reservoir, and at the same time, due to repeated cavity photon absorption and emission fixes the average photon number. The competition between optical pumping and cavity losses establishes a steady-state photon number, with the ratio of the excited to ground state dye molecules serving as an effective chemical potential. Another important ingredient is the curvature of the cavity mirrors which creates a harmonic trapping potential, modifying the density of states of the photons to resemble that of a massive boson. Thus, a defining feature of photon BECs is their inherently driven-dissipative nature. This non-equilibrium character provides a platform to observe a range of dynamical phenomena, like an observation of a non-Hermitian phase transition [160].

While several theoretical models have successfully described various aspects of a photon BEC [161–163], a comprehensive framework that explicitly incorporates the $U(1)$ symmetry breaking terms, associated with condensation, alongside photon number fluctuations on an equal footing remains an open problem. After reviewing previous work, this chapter will incorporate the condensate, and provide insights into the mechanism that stabilizes it.

6.1 Photon BEC in a Driven-Dissipative Microcavity

The dye molecules filling the microcavity are modeled as two-level systems, representing their electronic state, denoted by the Pauli matrices σ^α, where $\alpha \in [+, -, z]$. Each molecule, indexed by i, is also equipped with vibrational degrees of freedom, represented by the bosonic modes b_i. In the photon BEC regime, the system can be effectively modeled using only the cavity mode into which the photons condense. This photon mode, denoted by a, interacts with the molecular electronic transitions via a Jaynes-Cummings coupling [164]. The Hamiltonian describing this system is given by

$$H = \delta a^\dagger a + \sum_{i=1}^{M} \left(\frac{\Delta}{2}\sigma_i^z + \Omega b_i^\dagger b_i + \Omega\sqrt{S}\sigma_i^z \left(b_i^\dagger + b_i\right)\right) + \tilde{g}\sum_i \left(a^\dagger \sigma_i^- + a\sigma_i^+\right). \tag{6.1}$$

Here $\delta = \omega - \Delta$ represents the detuning given by the energy difference between the photon mode with frequency ω and the two-level system energy splitting Δ. Typically, the cavity photon is red-detuned such that $\delta < 0$. The vibrational mode frequency is given by Ω, the number of dye molecules in the system is denoted by M, and S is the Huang-Rhys parameter, which quantifies the coupling strength between the electronic states and the phonon displacement operator. The light-matter coupling strength is given by $\tilde{g}$. The coupling S is typically large, meaning that processes containing multiple single-phonon scattering play a significant role in the system dynamics. To account for these effects, the polaron transformation is applied. This transformation undoes the shift of the displacement of the vibrational modes, thereby diagonalizing the molecular part of the Hamiltonian. It is defined by the unitary operator

$$U_i = e^{-\sqrt{S}\sigma_i^z\left(b_i^\dagger - b_i\right)}. \tag{6.2}$$

Applying this transformation to the Hamiltonian gives

$$\widetilde{H} = \delta a^\dagger a + \sum_{i=1}^{M} \left(\frac{\Delta}{2}\sigma_i^z + \Omega b_i^\dagger b_i\right) + \tilde{g}\sum_i \left(D_i^\dagger(-\sqrt{S})\, a^\dagger \sigma_i^- + D_i(\sqrt{S})\, a\sigma_i^+\right), \tag{6.3}$$

where $\widetilde{H} = \sum_i U_i^\dagger H_i U_i$ and $D_i(\pm\sqrt{S}) = e^{\pm 2\sqrt{S}\left(b_i^\dagger - b_i\right)}$ is the phonon displacement operator, which introduces the multi-phonon processes into the light-matter interaction term. The fast relaxation in the vibrational modes allows the phonon displacement operator to be assumed to be in thermal equilibrium. As a result, the expectation value of the displacement operators is given by $D_{i,T}(\pm\sqrt{S}) = e^{-2S\coth\frac{\beta\Omega}{2}}$. To account for fluctuations around this equilibrium value, the displacement operator is decomposed as $D_i(\sqrt{S}) = \widetilde{D}_i(\sqrt{S}) + D_{i,T}(\sqrt{S})$ [163]. Since the coupling constant $\tilde{g}$ is typically small, the bath effects can be effectively captured by a Lindblad approach, introduced in Section 1.1, where $\widetilde{D}_i(\sqrt{S})$ is treated as the bath [162]. Thus, the system Hamiltonian is given by

$$H_S = \delta a^\dagger a + \sum_{i=1}^{M} \frac{\Delta}{2}\sigma_i^z + g\sum_i \left(a^\dagger \sigma_i^- + a\sigma_i^+\right), \tag{6.4}$$

where the renormalized light-matter coupling is given by $g = \tilde{g}e^{-2S\coth\frac{\beta\Omega}{2}}$. The dissipative processes introduced by the interaction with the bath are described by the following Lindblad operators

$$\Gamma_{\mathrm{e}} L\left[a^\dagger \sigma_i^-\right], \quad \Gamma_{\mathrm{a}} L\left[a\sigma_i^+\right], \tag{6.5}$$

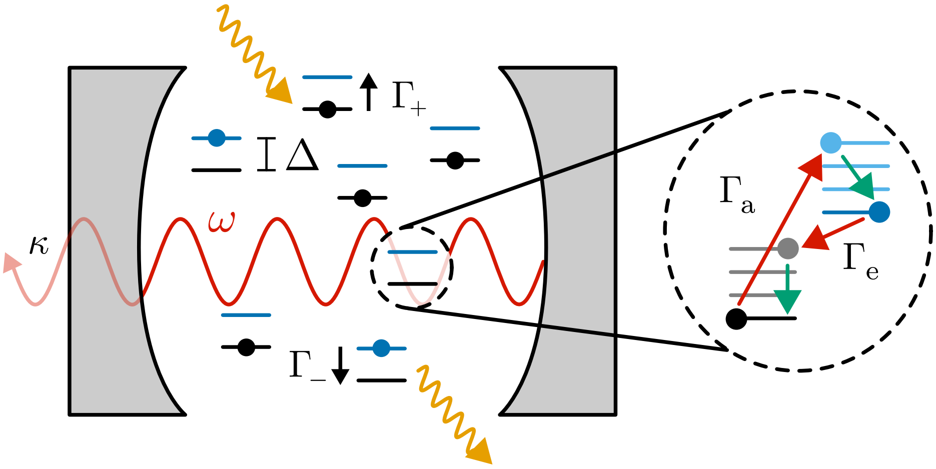

Figure 6.1: Illustration of an optical microcavity filled with dye molecules. A single photon mode is confined between two highly reflective mirrors, with cavity losses indicated by κ. The external incoherent pump excited the molecule system, represented by Γ_+, while spontaneous emission occurs at a rate Γ_-. The inset highlights the absorption (Γ_a) and emission (Γ_e) processes, as well as the dye molecules substructure. Fast vibrational relaxation processes, responsible for thermalization, are indicated by the green arrows.

where Γ_e and Γ_a correspond to the emission and absorption coefficients, respectively. Due to the fast relaxation of the vibrational modes, these two coefficients follow the Kennard-Stepanov relation, given by $\Gamma_\mathrm{a} = \Gamma_\mathrm{e} e^{\beta\delta}$, where β is the inverse temperature of the phonon bath. In addition to these processes, to account for the open nature of the cavity system, the following additional Lindblad operators are added

$$\Gamma_+ L\left[\sigma_i^+\right], \quad \Gamma_- L\left[\sigma_i^-\right], \quad \kappa L\left[a\right]. \tag{6.6}$$

Here Γ_+ describes the incoherent laser pumping and Γ_- corresponds to non-radiative decay. The photon loss due to cavity leakage is represented by κ. An illustration of the system, including all these processes, is shown in Figure 6.1.

For simplicity, the analysis is first performed without explicitly introducing $U(1)$ symmetry breaking terms, and is restricted to second-order cumulants only.[1] The system is considered to be in the weak light-matter coupling regime, far from the polariton formation regime, meaning that photon-molecule correlators can be neglected. Additionally, due to the frequent molecular collisions, the molecule-molecule correlations decay on a fast time scale and, thus, are also neglected. Finally, since the molecules see a homogeneous cavity field, they are assumed to be identical, allowing the molecular sum to be evaluated. Under these assumptions, the system is described by two degrees of freedom, the photon number, defined as $n = \langle a^\dagger a \rangle$, and the total number of excited molecules given by $m = \sum_{i=1}^{M} \langle \sigma^+ \sigma^- \rangle$. The equations of motion governing these quantities are obtained via the Lindblad formalism as

$$\dot{n} = -\kappa n - \Gamma_\mathrm{a} n(M - m) + \Gamma_\mathrm{e}(n + 1)m, \tag{6.7}$$
$$\dot{m} = \Gamma_+(M - m) - \Gamma_- m + \Gamma_\mathrm{a} n(M - m) - \Gamma_\mathrm{e}(n + 1)m. \tag{6.8}$$

To visualize how these processes lead to a finite photon number, it is useful to determine the steady-state solutions of the above equations, which are defined by setting the time derivatives

---

[1] This also follows the historical developments of the field, as early experiments on photon BECs primarily measured the photon number distributions.

to zero. Doing so, gives the following expression for the photon number

$$\overline{n} = \frac{\Gamma_{\mathrm{e}}\overline{m}}{\kappa + \Gamma_{\mathrm{a}}(M-\overline{m}) - \Gamma_{\mathrm{e}}\overline{m}}, \tag{6.9}$$

where $\overline{n}$ and $\overline{m}$ correspond to the steady state values of the photon number and the number of excited molecules, respectively. By using the Kennard-Stepanov relation for the absorption and emission coefficients, this expression can be rewritten in a form resembling the Bose distribution,

$$\overline{n} = \frac{1}{e^{\beta(\delta-\mu_{eff})} - 1 + d}, \tag{6.10}$$

where the chemical potential, determined by the ratio of excited to ground-state molecules, is introduced as

$$\mu_{eff} = T \ln\left[\frac{\overline{m}}{M-\overline{m}}\right], \tag{6.11}$$

Here, $d = \kappa/(\Gamma_{\mathrm{e}}\overline{m})$ represents the deviation[2] to form an ideal Bose distribution caused by cavity losses [166].

This result highlights the fact that by incorporating all the experimentally relevant excitation and decay processes, the fundamental challenges associated with the photon BEC can be effectively mitigated. However, while the steady-state photon number follows a Bose-like distribution, the stability of this state still needs to be analyzed. To address this, the next step involves computing the steady-state of the excited molecule number and performing a linear stability analysis. This will provide insight whether the system remains stable under small perturbations and will lead to uncovering the conditions under which this system undergoes a non-Hermitian phase transition [160].

6.2 Non-Hermitian Phase Transition

Understanding the stability of the photon BEC state requires analyzing how small fluctuations evolve over time. To systematically investigate this, the full steady-state must first be determined. To do that, it is convenient to first eliminate $\overline{n}$ by summing Equations (6.7) and (6.8), leading to the relation

$$\overline{n} = \frac{\Gamma_{+}M}{\kappa} - \frac{\Gamma_{+}+\Gamma_{-}}{\kappa}\overline{m}. \tag{6.12}$$

Substituting this into Equation (6.8) yields a quadratic equation for $\overline{m}$, which has the general solution

$$\overline{m} = -\frac{b}{2a} \pm \frac{1}{2a}\sqrt{b^2-4ac} \tag{6.13}$$

where the coefficients are given by

$$a = \frac{(\Gamma_{\mathrm{a}}+\Gamma_{\mathrm{e}})(\Gamma_{+}+\Gamma_{-})}{\kappa}, \quad b = -\left(\Gamma_{\mathrm{e}}+\Gamma_{+}+\Gamma_{-}+\frac{\Gamma_{\mathrm{e}}\Gamma_{+}M+\Gamma_{\mathrm{a}}M(2\Gamma_{+}+\Gamma_{-})}{\kappa}\right), \\ c = \frac{\Gamma_{+}M}{\kappa}(\kappa+\Gamma_{\mathrm{a}}M). \tag{6.14}$$

---

[2] Sometimes, this deviation is incorporated into the definition of the effective chemical potential, leading to the modified expression $\mu_{eff} = -T\ln\left[\frac{M-\overline{m}}{\overline{m}}\left(1+\frac{\kappa}{\Gamma_{\mathrm{a}}(M-\overline{m})}\right)\right]$ [165].

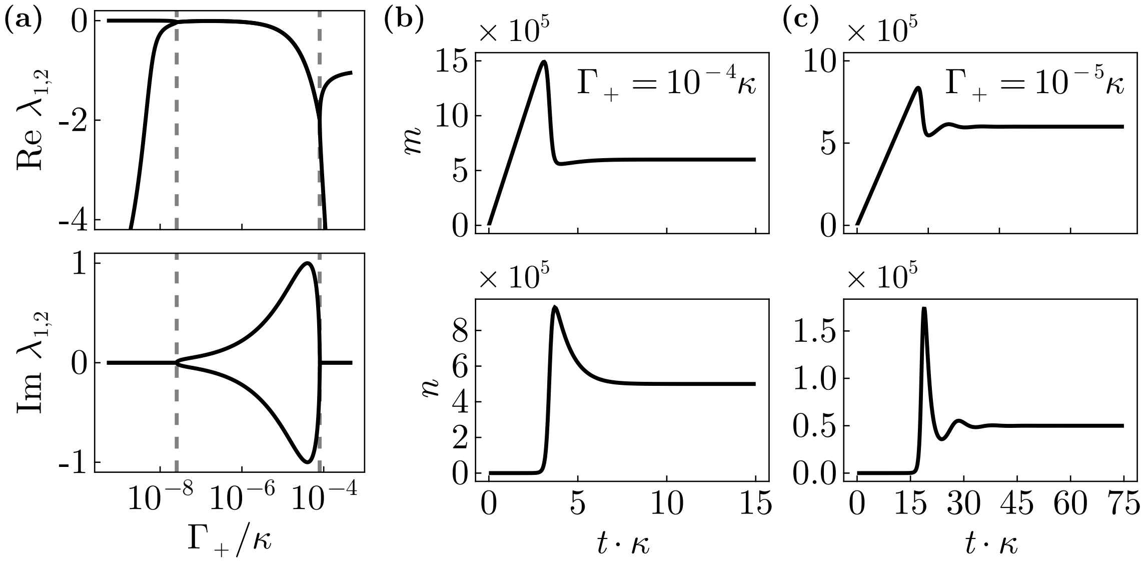

Figure 6.2: **(a)** Real and imaginary parts of the eigenvalues $\lambda_{1,2}$ of the non-Hermitian Jacobian matrix, as a function of the pumping rate Γ_+. For small Γ_+, the eigenvalues are real and negative, indicating a dissipative regime. At a critical value of Γ_+, marked by a dashed line, the two real eigenvalues coalesce, and a finite imaginary part emerges, highlighting an exceptional point. As Γ_+ is increased further, a second exceptional point appears, where the eigenvalues revert to being purely real. **(b,c)** Full time evolution of the number of excited molecules m (top) and the photon number n (bottom) for two different pumping regimes. **(b)** the bi-exponential decay regime with $\Gamma_+ = 10^{-4}\kappa$, **(c)** the oscillatory regime with $\Gamma_+ = 10^{-5}\kappa$. The parameters for both plots used are $M = 5 \cdot 10^9$, $\Gamma_- = 5 \cdot 10^{-5}\kappa$, $\Gamma_\mathrm{e} = 10^{-5}\kappa$, and $\Gamma_\mathrm{a} = 10^{-9}\kappa$, with initial conditions for **(b)** and **(c)** being $n_0 = m_0 = 0$.

Typically, one of these solutions leads to unphysical values, where $\overline{m} > M$ and $\overline{n} < 0$. This ensures that the other solution, which is a physical one, is the unique steady state. To assess the stability of the physical solution, a linear stability analysis is performed using the Jacobian matrix of the system, which describes the time evolution of small perturbations around the steady state and is given by

$$\frac{d}{dt}\begin{pmatrix}\delta n\\ \delta m\end{pmatrix} = \begin{pmatrix}-\kappa - \Gamma_\mathrm{a}(M-\overline{m}) + \Gamma_\mathrm{e}\overline{m} & \Gamma_\mathrm{a}\overline{n} + \Gamma_\mathrm{e}(\overline{n}+1)\\ \Gamma_\mathrm{a}(M-\overline{m}) - \Gamma_\mathrm{e}\overline{m} & -\Gamma_+ - \Gamma_- - \Gamma_\mathrm{a}\overline{n} - \Gamma_\mathrm{e}(\overline{n}+1)\end{pmatrix}\begin{pmatrix}\delta n\\ \delta m\end{pmatrix}. \tag{6.15}$$

Here δn and δm represent small deviations from the steady state values $\overline{n}$ and $\overline{m}$. As expected, the Lindblad processes lead to a non-Hermitian Jacobian matrix, where tuning the pumping rate Γ_+ can drive the system through a non-Hermitian phase transition. The eigenvalues of the Jacobian matrix are shown in Figure 6.2a as a function of Γ_+. For small Γ_+, both eigenvalues are real and negative, corresponding to a purely dissipative regime where perturbations decay monotonically. In this regime, the system exhibits a bi-exponential relaxation into the steady-state, as illustrated in Figure 6.2b. As Γ_+ increases, the two real eigenvalues coalesce at a critical pumping value, marking the emergence of an exceptional point. Beyond this, the eigenvalues acquire an imaginary component, leading to damped oscillatory dynamics as the steady-state is approached, as illustrated in Figure 6.2c. Further increasing Γ_+ results in the emergence of a second exceptional point, where the system transitions back to bi-exponential behavior.

6.2.1 Mode Reduction at the Exceptional Point

Due to the coalescence of the eigenvectors at a non-Hermitian phase transition, the number of independent modes in the system is reduced. A key question is what is the nature of the remaining mode at the exceptional point. Generally, answering this question is highly nontrivial because the concept of exceptional points originates from a linearized analysis, meaning that the full nonlinear dynamics is inaccessible within this framework. However, in this case, the full set of equations of motion can be rewritten as a single second order differential equation for the total excitations in the system, defined as the sum of the photon number and the number of excited molecules. This reformulation reveals that the system effectively possesses only a single degree of freedom, even at the exceptional point. To achieve this reduction, the system is transformed into new variables, given by the sum $x = (m+n)/\sqrt{2}$ and the difference $y = (m-n)/\sqrt{2}$. The differential equations for x and y can be obtained from Equations (6.7) and (6.8). Focusing on the differential equation for x

$$\dot{x} = \frac{\Gamma_+ M}{\sqrt{2}} - \frac{\kappa + \Gamma_+ + \Gamma_-}{2} x + \frac{\kappa - \Gamma_+ - \Gamma_-}{2} y, \tag{6.16}$$

which will be used to eliminate y from the system. Differentiation this equation with respect to time gives

$$\ddot{x} = -\frac{\kappa + \Gamma_+ + \Gamma_-}{2} \dot{x} + \frac{\kappa - \Gamma_+ - \Gamma_-}{2} \dot{y}, \tag{6.17}$$

which will be used to eliminate $\dot{y}$ from the system. The differential equation for y is given by

$$\dot{y} = \dot{x} - (\kappa + \Gamma_{\mathrm{a}} M)(x - y) + \Gamma_{\mathrm{e}}(x + y) + \frac{\Gamma_{\mathrm{a}} + \Gamma_{\mathrm{e}}}{\sqrt{2}} (x^2 - y^2). \tag{6.18}$$

Using Equations (6.16) and (6.17) this can be rewritten as

$$\ddot{x} + \alpha \dot{x} + \beta x + \lambda x^2 + \delta \dot{x}^2 + \mu \dot{x} x + \phi = 0. \tag{6.19}$$

The expressions for the coefficients are rather lengthy, making it instructive to introduce new constants that simplify the notation, let

$$\Gamma_t = \Gamma_+ + \Gamma_-, \quad \widetilde{\Gamma} = \frac{\Gamma_{\mathrm{a}} + \Gamma_{\mathrm{e}}}{\sqrt{2}}, \quad \gamma = \frac{\widetilde{\Gamma}}{\kappa - \Gamma_t}, \quad R = \kappa + \Gamma_{\mathrm{a}} M, \text{ and } p = \frac{\Gamma_+ M}{\sqrt{2}}. \tag{6.20}$$

With these definitions, the coefficients take a more compact form

$$\begin{aligned} &\alpha = -R - \Gamma_{\mathrm{e}} + \Gamma_t - 4\gamma p, \quad \beta = -\Gamma_t R - \kappa \Gamma_{\mathrm{e}} - 4\gamma p(\kappa + \Gamma_t), \\ &\lambda = 2\gamma\kappa\Gamma_t, \quad \delta = 2\gamma, \quad \mu = 2\gamma(\kappa + \Gamma_t), \quad \phi = 2\gamma p^2 + p(R + \Gamma_{\mathrm{e}}). \end{aligned} \tag{6.21}$$

The final equation of motion obtained in Equation (6.19) takes on the form of a nonlinear oscillator equation, where the total number of excitations plays the role of the displacement. This analogy assigns physical meaning to each coefficient, α represents the damping force, β characterizes the linear restoring force, γ corresponds to a nonlinear restoring force, δ acts as a nonlinear damping, μ describes the coupling between the total excitation number and its time derivative, and finally, ϕ is a constant driving force. Given the apparent complexity of the equation, with multiple nonlinear terms, it is rather surprising that the resulting dynamics remain stable and well-behaved.

This equation will not be analyzed further but rather serves as a proof of concept, demonstrating that the system can indeed be reduced to a single effective degree of freedom, which survives even when the parameters are tuned through the exceptional point. However, an interesting question remains, namely what happens to the non-Hermitian phase transition when explicit $U(1)$ symmetry-breaking terms are introduced? In principle, additional degrees of freedom act as spectators, meaning that the exceptional point should persist. However, in the construction of these equations, the condensate expectation value was explicitly neglected, suggesting that allowing for a finite condensate could significantly impact the system's behavior. Moreover, it remains unclear whether a finite condensate actually emerges in the steady state, or whether the system instead stabilizes in a regime where condensation does not occur. If a condensate does form, it remains to be determined whether the non-Hermitian phase transition persists in this regime. To properly address these questions, the formalism must be extended, and explicit equations of motion for the condensate need to be constructed.

6.3 Photon BEC Dynamics with $U(1)$ Symmetry Breaking

In the previous section, all the necessary ingredients for the photon number to follow a Bose distribution with a finite chemical potential in the steady state were introduced. Physically, when the system enters the BEC regime, the ground state acquires a well-defined phase [167, 168], corresponding to the spontaneous breaking of the $U(1)$ symmetry. In this system, photon emission arises from a coherent dipole process, where the polarization and the phase of the molecular ensemble dictates the phase of the photon condensate. Since the polarization is considered to be fixed and follows the pump laser [168], it is omitted, and the coherent regime is considered. Without molecular coherence, the molecules would act as independent emitters, leading to purely incoherent spontaneous emission. Therefore, to fully account for all the terms that break the $U(1)$ symmetry, it is not sufficient to only introduce $\langle a \rangle$, the coherent electronic transition rate, $\langle \sigma^- \rangle$, must also be included.[3] Moreover, by explicitly constructing an equation of motion for $\langle \sigma^- \rangle$, the formalism ensures that the coherent energy transfer between the molecules and the cavity photons is captured dynamically. With these additions, the system is now described by four degrees of the freedom, whose equations of motion are derived by incorporating the Lindblad operators defined in Equations (6.5) and (6.6), leading to

$$\dot{n} = -\kappa n - \Gamma_{\mathrm{a}} n(M-m) + \Gamma_{\mathrm{e}}(n+1)m + ig\left(\psi^*\chi - \psi\chi^*\right), \tag{6.22}$$

$$\dot{m} = \Gamma_+(M-m) - \Gamma_- m + \Gamma_{\mathrm{a}} n(M-m) - \Gamma_{\mathrm{e}}(n+1)m - ig\left(\psi^*\chi - \psi\chi^*\right), \tag{6.23}$$

$$\dot{\psi} = ig\chi - \frac{\kappa}{2}\psi - \frac{\Gamma_{\mathrm{a}}}{2}(M-m)\psi + \frac{\Gamma_{\mathrm{e}}}{2}m\psi, \tag{6.24}$$

$$\dot{\chi} = -ig(2m-M)\psi - \frac{\Gamma_+ + \Gamma_-}{2}\chi - \frac{\Gamma_{\mathrm{a}}}{2}n\chi - \frac{\Gamma_{\mathrm{e}}}{2}(n+1)\chi, \tag{6.25}$$

where $\psi = \langle \hat{a} \rangle$ and $\chi = \langle \hat{\sigma}_- \rangle$ are complex quantities. It can be seen that there are two modifications to Equations (6.7) and (6.8). First a coherent term appears from the Hamiltonian part in the Lindblad equation. Second, since ψ is now explicitly included, n now consists of a fluctuating part and an average part, given by $n = n_{fl} + |\psi|^2$. Consequently, the relation $n > |\psi|^2$ must hold throughout the entire time evolution. Note that direct contribution from the detuning δ to the equation of motion has been neglected. This is because δ only induces a global phase rotation in the symmetry breaking terms, since both ψ and χ have a global phase that is not physically measurable, its effect is irrelevant. However, the dependence of the emission and absorption coefficients on δ is retained.

---

[3] Superradiant effects are neglected since the system is taken to be in the weak light-matter coupling regime. Photon emission is therefore governed by local molecular coherence rather than inter-molecular collective radiative processes.

Before analyzing the full steady-state of all quantities, it is useful to first gain physical insight into the conditions that allow a finite condensate. To this end, it is useful to construct equations of motion for the combinations $\psi^*\dot{\chi} + \psi\dot{\chi}^*$, $\psi^*\dot{\chi} - \psi\dot{\chi}^*$, and $\chi\dot{\psi}^* - \chi^*\dot{\psi}$, which take the form

$$\psi^*\dot{\chi} + \dot{\chi}^*\psi = -\frac{\Gamma_+ + \Gamma_- + \Gamma_\mathrm{a} n + \Gamma_\mathrm{e}(n+1)}{2}\left(\psi^*\chi + \psi\chi^*\right), \tag{6.26}$$

$$\psi^*\dot{\chi} - \dot{\chi}^*\psi = -2ig(2m - M)|\psi|^2 + \frac{\Gamma_+ + \Gamma_- + \Gamma_\mathrm{a} n + \Gamma_\mathrm{e}(n+1)}{2}\left(\psi^*\chi - \psi\chi^*\right), \tag{6.27}$$

$$\chi^*\dot{\psi} - \dot{\psi}^*\chi = 2ig|\chi|^2 - \frac{\Gamma_\mathrm{e} m - \kappa - \Gamma_\mathrm{a}(M - m)}{2}\left(\psi^*\chi - \chi^*\psi\right). \tag{6.28}$$

When the steady state is considered, it follows that $\overline{\psi}^*\overline{\chi} + \overline{\psi}\overline{\chi}^* = 0$. Which when expressed in polar form, $\overline{\psi} = |\overline{\psi}|e^{i\theta_{\bar{\psi}}}$, $\overline{\chi} = |\overline{\chi}|e^{i\theta_{\bar{\chi}}}$ implies a relation between the phases, given by $\cos\left(\theta_{\bar{\psi}} - \theta_{\bar{\chi}}\right) = 0$. This confirms that a phase-locking condition is present in the steady state, given by $\theta_{\bar{\psi}} - \theta_{\bar{\chi}} = \pi/2$. This particular phase relation minimizes the coherent energy in the Hamiltonian given in Equation (6.1), meaning that coherence exchange between the photon condensate and the molecules does not cost energy. Moreover, a consequence of this is that $\overline{\psi}^*\overline{\chi} - \overline{\psi}\overline{\chi}^* = 2i|\overline{\psi}||\overline{\chi}|$, which leads to a maximum contribution of the condensate to the steady-states of n and m. Substituting this into Equation (6.28), yields $|\overline{\chi}| = G_\psi|\overline{\psi}|/2g$, which highlights the necessity of a finite polarization for a finite steady-state condensate. Using this relation allows Equation (6.27) to be rewritten as

$$\left(2g(2\overline{m} - M) + \frac{G_\psi G_\chi}{2g}\right)|\overline{\psi}|^2 = 0, \tag{6.29}$$

where $G_\psi = \Gamma_\mathrm{e}\overline{m} - \kappa - \Gamma_\mathrm{a}(M - \overline{m})$ and $G_\chi = \Gamma_+ + \Gamma_- + \Gamma_\mathrm{a}\overline{n} + \Gamma_\mathrm{e}(\overline{n} + 1)$ depend on the yet-to-be determined steady state values of n and m. The last step to determine a condition for a finite condensate in the steady-state is to substitute all previously derived relations into Equation (6.22), obtaining

$$G_\psi(\overline{n} - |\overline{\psi}|^2) + \Gamma_e\overline{m} = 0. \tag{6.30}$$

Since the steady state value of n must satisfy $\overline{n} > |\overline{\psi}|^2$, it follows that $G_\psi < 0$ in the steady state. Substituting this into Equation (6.29) implies that $2\overline{m} - M > 0$ must hold. This suggests that a finite condensate can only occur in the presence of population inversion, corresponding to the lasing regime of the system. This conclusion does not immediately follow from the structure of the equations nor from physical intuition, making it appear inconsistent with experimental observations. Surprisingly, these equations contain a mechanism that fully resolves this apparent discrepancy. To uncover this mechanism, the steady-states of all quantities must be computed.

6.3.1 Condensate Stabilization via Ghost Fixed-Point

It turns out that the system dynamics naturally lead to an unexpected stabilization mechanism, preventing the condensate from vanishing over long timescales. To understand how this occurs, the full steady-state values need to be computed. This is done by using Equation (6.29) with Equation (6.12)[4], leading to a quadratic equation for $\overline{m}$ with the general solution

$$\overline{m} = -\frac{b}{2a} \pm \frac{1}{2a}\sqrt{b^2 - 4ac}, \tag{6.31}$$

---

[4] Even though this equation has been derived in the absence of condensate, the validity of this equation in this case can be confirmed by summing Equations (6.22) and (6.23).

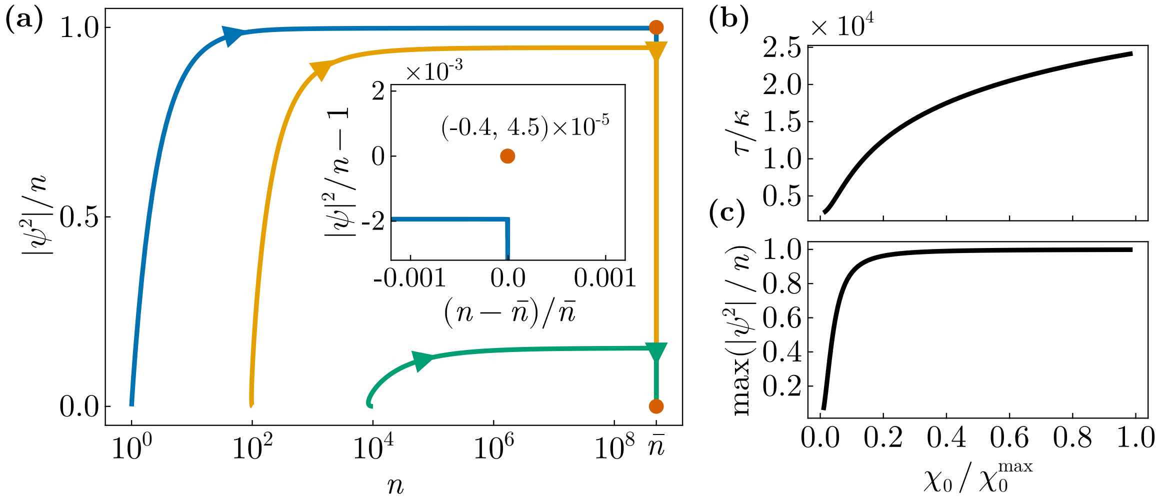

Figure 6.3: **(a)** Time evolution trajectories of $|\psi|^2/n$ for different initial photon numbers, obtained from Equations (6.22) to (6.25). Two fixed points are marked by filled circles, one unphysical hyperbolic fixed point where $|\overline{\psi}|^2 > \overline{n}$ and another one corresponding to the physical fixed point where the condensate vanishes. The inset shows the dynamics close to the unphysical fixed point. **(b,c)** Life time τ and maximum condensate fraction as functions of the initial ratio $\chi_0/\chi_0^{\max}$. The life time is defined as the time it takes for the system to reach half of it's maximum condensate fraction. The parameters used are $M = 5 \cdot 10^9$, $\Gamma_- = 5 \cdot 10^{-5}\kappa$, $\Gamma_\mathrm{e} = 1.48 \cdot 10^{-7}\kappa$, $\Gamma_\mathrm{a} = 10^{-9}\kappa$, and $g = 10^{-6}\kappa$. The initial conditions used in **(a)** are $n_0 = 1, 10^2, 10^4$ for each line, $m_0 = 5 \cdot 10^6$, $\chi_0 = 0.9\chi_0^{\max}$ and $\psi_0 = 0$.

where the coefficients are given by

$$a = -\frac{2\widetilde{\Gamma}^2\Gamma_\mathrm{t}}{\kappa}, \quad b = \sqrt{2}\,\widetilde{\Gamma}\left(\frac{R\Gamma_\mathrm{t}}{\kappa} + \Gamma_\mathrm{t} + \Gamma_\mathrm{e} + \frac{\sqrt{2}\,\widetilde{\Gamma}}{\kappa}\right), \quad c = -\left(4gM + R(\Gamma_\mathrm{t} + \Gamma_\mathrm{e}) + \frac{2pR\widetilde{\Gamma}}{\kappa}\right). \tag{6.32}$$

One of these two solutions leads to $\overline{m} > M$ and $\overline{n} < 0$. The steady-state value of $|\psi|^2$ is then determined using Equation (6.30). The remaining two solutions correspond to $\overline{\psi} = \overline{\chi} = 0$ and match those obtained from the reduced system in Equation (6.13).

Although the steady-state solutions with $\overline{m} < M/2$ and a finite condensate are unphysical, the associated fixed point nonetheless has a significant impact on the system dynamics. This effect is illustrated in Figure 6.3, where trajectories are drawn toward the unphysical fixed point and remain there for a significant duration, with a lifetime $\tau \sim 10^4/\kappa$. This behavior is reminiscent of ghost attractor dynamics, which lead to a slow passage through a bottleneck [120].[5] Notably, this timescale is orders of magnitude longer than the typical experimental observation times ($\sim 10^3/\kappa$). Eventually, the trajectories are repelled and relax toward the stable fixed point.

The maximum condensate fraction depends on the initial number of photons in the cavity and on the initial electronic transition rate χ_0. The latter is constrained by the requirement

---

[5] There are, however, some differences. In the usual mathematical sense, a ghost attractor arises when a stable fixed point is removed from the system, meaning that only the "ghost" of the attractor remains, yet it still influences the dynamics. In contrast, the fixed point in this system lies beyond the physical boundary that constrains the trajectory. Thus, although the origins of the bottleneck dynamics differ, the term "ghost" fits this system also rather well.

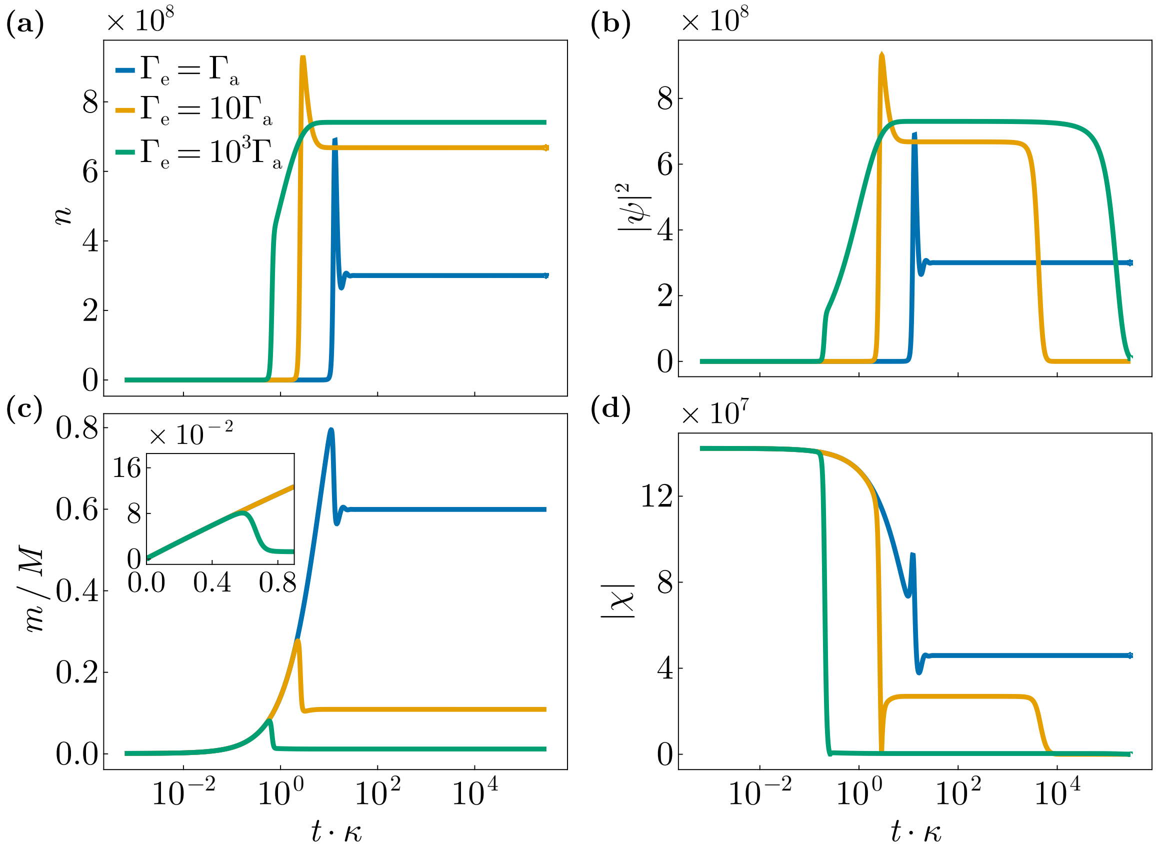

Figure 6.4: Time evolution of Equations (6.22) to (6.25) for different emission coefficients, highlighting the lasing regime where $\overline{m} > M/2$ and two long-lived metastable condensate regimes where $\overline{m} \ll M/2$. **(a)** Photon number n, showing similar dynamics to Figure 6.2b. **(b)** Condensate amplitude $|\psi|^2$, initially following the photon number dynamics before decaying in the metastable regime, while remaining finite in the lasing regime. **(c)** Fraction of excited molecules, with the inset detailing the initial linear growth arising from the pumping. **(d)** Electronic transition rate amplitude $|\chi|$, displaying decay behavior outside the lasing regime and stabilization within it. The parameters used apart from the emission coefficients are the same as in Figure 6.3 with $n(0) = 1$ for all trajectories.

that the initial molecular density matrix

$$\rho = \begin{pmatrix} m_0 & \chi_0 \\ \chi_0^* & M - m_0 \end{pmatrix} \tag{6.33}$$

has strictly positive eigenvalues, implying $|\chi_0| < \sqrt{m_0(M - m_0)} = \chi_0^{\max}$. Physically $|\chi_0|$ represents the initial strength of the classical dipole moment of the molecules, which determines the efficiency of photon emission, which experimentally is around 95% [159], meaning that nearly all absorbed photons are re-emitted. However, a large part of this emission escapes through the sides of the cavity rather than emitting into the cavity mode. Despite this, as shown in Figure 6.3b, a large condensate fraction occurs even at $\chi_0 \sim 0.2\chi_0^{\max}$.

Further time evolutions, shown in Figure 6.4, explore this behavior for different emission coefficients. As the emission coefficient approaches the absorption coefficient, the population in the ground and excited state balances out, meaning that achieving population inversion

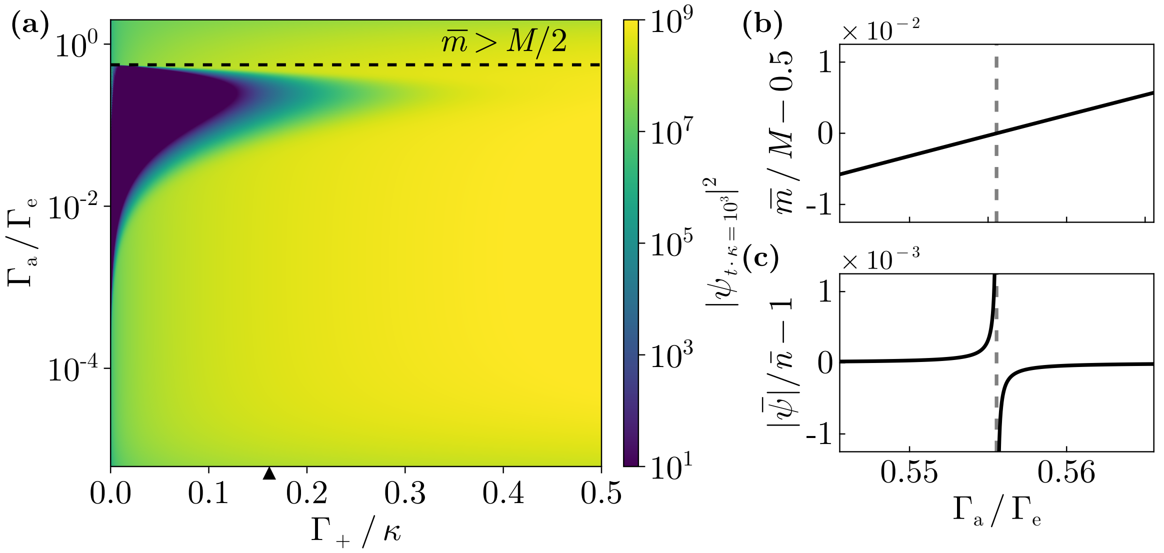

Figure 6.5: Phase diagram showing the value of the condensate amplitude $|\psi|^2$ at $t \cdot \kappa = 2 \times 10^3$ as a function of the ratio of absorption and emission coefficients Γ_a/Γ_e and the pumping strength Γ_+/κ[10]. The lasing regime, where the steady state exhibits population inversion, lies above the dashed line. **(b,c)** Cross-sections at $\Gamma_+ = 0.15\kappa$ near the lasing transition. **(b)** Deviation from population inversion. **(c)** Position of the fixed point, illustrating the transition from a physical fixed point in the lasing regime to an unphysical one outside of it. The parameters used are $M = 5 \cdot 10^9$, $\Gamma_a = 5 \cdot 10^{-10}\kappa$ and $g = 10^{-6}\kappa$

with pumping is easier, as seen in the plots. In this regime, as predicted from the steady-state calculations, the condensate does not decay. When the emission coefficient is increased, a long-lived metastable condensate regime emerges. This state is stabilized by the proximity of the trajectory to the unphysical fixed point in phase space, and can persist for lifetimes longer than $\tau \sim 10^6/\kappa$, depending on system parameters. During this bottleneck period, both the photon number and the total molecule number remain constant.

To analyze the system's behavior across a broader range of parameters, a phase diagram, shown in Figure 6.5, is constructed where the pumping rate and the emission coefficient are varied. The value of $|\psi|^2$ measured at $t \cdot \kappa = 10^3$ is represented by the color scale. The lasing regime occurs close to the point where the absorption and emission coefficients are equal to one another, the boundary is constructed by the population inversion requirement. When the emission coefficient is increased, the system transitions into the photon BEC regime. The unphysical fixed point diverges precisely at half filling, when $\overline{m} = M/2$, marking the transition of the fixed point being physical to unphysical. Beyond this transition, the unphysical fixed point becomes algebraically close to the physical boundary given by $|\overline{\psi}|^2 = \overline{n}$. The closer this fixed point is to the physical boundary, the more it influences the dynamics, leading to a progressively longer-lived photon BEC.

6.3.2 Non-Hermitian Phase Transition with Condensate

The matrix describing the time evolution of small perturbation around the steady state is given by

$$\frac{d}{dt}X = JX, \tag{6.34}$$

where $X = (\delta n, \delta m, \delta\psi, \delta\chi, \delta\psi^*, \delta\chi^*)^T$ and the Jacobian matrix is given by

$$J = \begin{pmatrix} G_\psi & \sqrt{2}\,\widetilde{\Gamma}\,\overline{n} + \Gamma_\mathrm{e} & -ig\overline{\chi}^* & ig\overline{\psi}^* & ig\overline{\chi} & -ig\overline{\psi} \\ \Gamma_\mathrm{a} M - \sqrt{2}\,\widetilde{\Gamma}\,\overline{m} & -G_\chi & ig\overline{\chi}^* & -ig\overline{\psi}^* & -ig\overline{\chi} & ig\overline{\psi} \\ 0 & \widetilde{\Gamma}\,\overline{\psi}/\sqrt{2} & G_\psi/2 & ig & 0 & 0 \\ -\widetilde{\Gamma}\,\overline{\chi}/\sqrt{2} & -2ig\overline{\psi} & -ig(2\overline{m} - M) & -G_\chi/2 & 0 & 0 \\ 0 & \widetilde{\Gamma}\,\overline{\psi}^*/\sqrt{2} & 0 & 0 & G_\psi/2 & -ig \\ -\widetilde{\Gamma}\,\overline{\chi}^*/\sqrt{2} & -2ig\overline{\psi}^* & 0 & 0 & ig(2\overline{m} - M) & -G_\chi/2 \end{pmatrix}. \tag{6.35}$$

In the true steady state, where $\overline{\psi} = \overline{\chi} = 0$, the Jacobian matrix is block diagonal. This ensure that the non-Hermitian phase transition observed in the reduced system survives. This is explicitly shown Figure 6.6, where the eigenvaluesare plotted. Interestingly, the two additional eigenvalues also undergo a non-Hermitian phase transition, but at different critical pumping rates. As previously discussed, the system's dynamics are strongly influenced by the presence of the unphysical fixed point. Consequently, the dynamics associated with the phase transition would only manifest on an extremely large time scale, when the true steady state is approached. During the bottleneck period, the trajectories are dominated by the eigenvectors associated with the unphysical fixed point, To further explore this, a linear stability analysis was performed at that fixed point, and the corresponding eigenvalues are plotted in Figure 6.6b. Interestingly, the critical pumping at which the right-most phase transition occurs is identical for both the physical and unphysical fixed point, and the eigenvalues exhibit similar behavior. This implies that, although the phase transition at the true steady state would only manifest on extremely long time-scales, the same dynamics occur earlier due to the influence of the unphysical fixed point when the bottleneck dynamics are approached. Since the true steady state matches that of the reduced system, this explains why the reduced system provided such accurate predictions despite its simplifications.

6.4 Summary and Outlook

In this chapter, the non-equilibrium dynamics and steady-state properties of the photon BEC were explored within the Lindblad formalism, with a particular focus on explicit $U(1)$ symmetry breaking terms arising from the condensate and the molecular degrees of freedom. A key result was the identification of an extremely long-lived metastable condensate state, which arise due to the presence of a fixed point beyond the physical boundary in phase space. Because of this, this fixed point was coined as a ghost fixed point. The lifetime of this metastable state was shown to scale dramatically, even reaching timescales as large as $\tau \sim 10^5/\kappa$ for experimentally relevant parameter regimes. Notably, in experiments, the observation window is roughly $\tau \sim 10^3/\kappa$ [159], meaning that any decay effects would not be visible. This provides a compelling explanation for the apparent steady condensate values seen in experiments.

The behavior of the system was further analyzed by constructing a phase diagram, where the pump strength and the emission coefficient were varied, two parameters which are easily tuned experimentally. This revealed two distinct regimes, a lasing phase characterized by population inversion and a finite steady state condensate and a photon BEC regime where the condensate eventually decays. At the transition boundary, the ghost fixed point diverges and emerges as the stable lasing fixed point in the lasing regime. In the BEC regime, the ghost fixed point is algebraically close to the physical boundary, where the condensate fraction becomes 1. During this long-lived dynamics, both the photon number and the total molecule number have

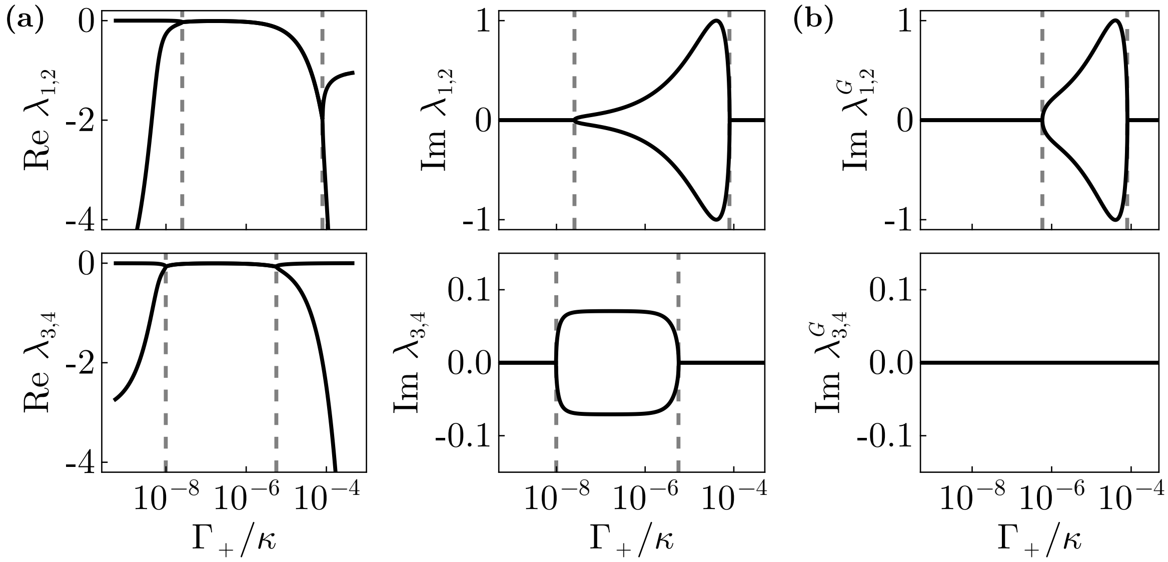

Figure 6.6: **(a)** Dependence of the eigenvalues of the Jacobian matrix for the system of equations given by Equations (6.22) to (6.25) on the pumping rate Γ_+. The top two panels are identical to the eigenvalues of the reduced system, previously shown in Figure 6.2a. The parameters are also taken to be the same as in that figure, with the addition of $g = 10^{-6}\kappa$. The bottom two panels depict the eigenvalues associated with ψ and χ. Notably, they also exhibit an exceptional point at independent critical pumping rates. **(b)** The imaginary parts of the eigenvalues associated with the unphysical fixed point λ^G. The critical value of the pumping rate Γ_+ at which the right-most phase transition occurs is identical in both panels.

reached their steady-state values, meaning that the system effectively thermalizes before the condensate decays. This is consistent with the experimental findings in [169].

Beyond steady-state properties, a linear stability analysis was performed to investigate the fate of non-Hermitian phase transition observed in this system [160] when explicit $U(1)$ symmetry breaking terms are introduced. The analysis revealed that at the true steady state, where the condensate vanishes, the non-Hermitian phase transition observed in the reduced system persists. However, since the bottleneck time is the experimentally relevant timescale, this phase transition would not be observed. Strikingly, the ghost fixed point provides an identical phase transition at the exact same critical pumping rate. These dynamics would appear when the bottleneck region is approached. This explains why the previous studies using the reduced system were able to accurately predict the system's behavior.

Although this analysis was carried out in the context of photon BECs, the equations of motion studied here are not unique to this system. Similar dynamical equations arise in other driven-dissipative bosonic system, such as polariton lasers [170] or exciton-polariton systems [171]. This suggests that the analysis presented here is broadly applicable beyond photon BECs. A key takeaway from this work is the importance of not restricting analyses to steady-state solutions alone, but rather consider the full dynamical evolution, which can reveal unexpected features such as seen in this work. While these results had a more theoretical interest, experimental verification of these predictions, remains an important next step. Specifically, measuring the finite lifetime of the metastable condensate would provide a direct test of these predictions. This could be achieved either by extending measurement window or by tuning the system parameters to shorten the bottleneck time.

Another further outlook is the investigation of the mode at the exceptional point induced by the ghost fixed point. Notably, in this case, the only modification introduced is the addition of an extra term in Equation (6.19), which does not couple to the total excitation number, corresponding to the coherent part of the Hamiltonian. This suggests that even a simplified analysis of Equation (6.19) could provide valuable insight. Once this is understood, the coupling to ψ and χ can be examined in greater detail.

An important question concerns the validity of the assumptions made in this analysis. For instance, when multiple photon modes are considered, non-Markovian effects become important [164], introducing memory effects that are not captured by the Lindblad formalism. It remains an open question whether the ghost fixed point observed here is simply an artifact of ignoring memory effects, which could, in principle, stabilize the condensate to a finite value in the steady state, or whether the inclusion of higher-order terms in the cumulant expansion would lead to a physical fixed point. A non-Markovian quantum field theory based approach to study these effects was developed in [172], though due to the complexity of the problem, was restricted to short time evolutions, meaning that the long bottleneck dynamics would have not been seen. Performing a steady-state calculation using the non-Markovian framework would provide valuable insights into the importance of memory effects.

Conclusion

The work presented in this thesis has examined a broad range of non-equilibrium phenomena across several distinct physical systems. The focus has been on driven, dissipative fermionic and bosonic systems, where far from equilibrium Floquet steady states, many body optical responses, non-Hermitian phase transitions, and photon condensation were explored. These phenomena show how non-equilibrium systems provide a platform for exploring rich physics across a wide variety of experimental and theoretical settings.

Chapters 1 and 2 established the theoretical foundation on which the later chapters build. Chapter 1 introduced two approaches to non-equilibrium systems, the Lindblad formalism and the Keldysh quantum field theory formalism. The Lindblad approach is suited for systems coupled to a Markovian bath, while the Keldysh method, although more involved, allows for memory and correlation effects to be treated. Chapter 2 covered strongly correlated electron systems, with an emphasis on heavy fermion physics. The techniques discussed include non-equilibrium dynamical mean field theory (DMFT) and the non-crossing approximation (NCA), implemented using the auxiliary particle method. Although primarily introductory, this chapter also presented some developments, such as a formulation for computing entanglement entropy in the auxiliary particle framework and a method for using standard FFTs on exponential grids, which are well suited to treat the Kondo problem. The entanglement entropy formulation could be useful in future work where the effect of crystalline electric fields in heavy fermion systems is studied. The FFT method can be broadly applicable in any context where exponential grids are useful.

The research part of this thesis begins with Chapter 3, which studies how a heavy fermion system responds to being driven by light. Because the heavy fermion states is strongly dependent on the hybridization between the conduction electrons and the *d*-electrons, the light-matter interaction had to be extended beyond the standard Peierls substitution to include dipole transitions. This meant that the driving field now affects two quantities, namely the impurity energy level, influenced from the intraband transitions, and the hybridization, modified through dipole processes. In this setting, the light field was treated semiclassically and assumed to be time periodic, which enabled a Floquet analysis. This scenario was analyzed within the Floquet Keldysh DMFT framework, allowing both the periodic nature of the drive and the strong electronic correlations to be captured. The developed Floquet Keldysh DMFT formalism is a general approach and can be applied to a wide range of strongly correlated systems, without relying on high-frequency expansions.

The heavy fermion state was found to be robust against the drive at both small and large driving frequencies, where the system either experiences an adiabatic response to the drive or an averaged out response. However, at intermediate frequencies, a competition between the Kondo screening and the drive led to a suppression of the heavy fermion state. In general, it was found that the hybridization driving leads to a stronger suppression compared to the impurity level driving, reinforcing the importance of including dipole terms in the light-matter coupling. The most pronounced suppression occurred when the driving frequency was comparable to the hybridization energy scale, $\Omega \approx V$. This was attributed to the fact that in this case, the electrons can transition from the singly occupied state to the Fermi level via the usual hybridization and now additionally via photon-assisted hybridization. This enhances the effective hybridization, and drives the system into a mixed valence regime, ultimately destroying the Kondo state.

The study of the fate of the heavy fermion state under irradiation of light continues in Chapter 4, which analyzes a THz spectroscopy experiment performed on CeCu_6 [68]. Following an initial reflection from the sample, a delayed secondary pulse was observed in the experimental measurement, attributed to Kondo physics. To analyze such a scenario, the semi classical analysis used in the previous chapter is no longer sufficient. This is because the energy scales of THz pulse closely matches that of the Kondo quasiparticles, meaning that there is no separation of time scales and that the light field must be treated within a quantum field theory framework. This was achieved by incorporating the light field into the DMFT formalism. At the level of the local problem, and using the auxiliary particle method, it was shown that the light field enters as an additional NCA diagram. A two-time non-equilibrium DMFT solver [89] was used to capture the real-time response of the system to the pulse. This allowed for the calculation of the renormalized photon pulse after interacting with the system, giving access to the optical response of the heavy fermion material that could be directly compared to the THz spectroscopy data.

This microscopic description of the problem revealed two main insights. Initially, the Kondo state is rapidly destroyed, due to the strong renormalization of the hybridization at the peak of the incoming pulse. Similarly to the conclusions of the previous chapter, this drives the system into a mixed valence regime, destroying the Kondo state altogether. After the pulse has passed, the Kondo state can rebuild itself, however, this recovery requires a very long timescale. As the system relaxes, the excess energy introduced by the pulse is released via two dissipative channels. The first one is via photon emission, which is captured by the renormalized photon pulse. The second one is via energy transfer to the other electronic bands, which are modeled by the inclusion of a fermionic bath. By fitting the photon response with all of these processes, the shape of the echo pulse was extracted. This revealed that the echo pulse is not simply a reflection of the initial Gaussian pulse but has a distinct lineshape, confirming the many-body origin of the delayed response.

Experimentally, the study also analyses gold-doped samples of $\mathrm{CeCu}_{6-x}\mathrm{Au}_x$, where the system undergoes a quantum phase transition with a critical point near $x \approx 0.1$. For intermediate concentrations $0.1 \leq x \leq 0.5$, an initial increase in the Kondo weight is still observed, but it never reaches the same Kondo weight as in undoped case. Interestingly, deep in the AFM regime, at $x = 1$, no Kondo response is observed for any temperature. This indicates that the influence of the RKKY interaction already begins at much higher temperatures than anticipated, namely, orders of magnitude above the Néel temperature [101]. From a theoretical standpoint, the formalism can be extended to other models and materials in studies where the light–matter coupling plays a non-trivial role. It is particularly well suited to systems where no clear separation of timescales exists and a full quantum treatment of the light field is required.

The focus of the thesis moves away from heavy-fermion systems in Chapter 5, which analyzes a THz pump-probe experiment performed on EuO. In the experiment, a temperature-dependent non-Hermitian phase transition was observed in the magnetization dynamics following optical excitation. The relaxation dynamics was found to change from bi-exponential decay to oscillatory dynamics at a temperature $T^* \approx 85\mathrm{K}$, marking the first observation of a non-Hermitian in a bulk condensed matter system rather than in an engineered device. By fitting the relaxation rates, the signature square root dependence near an exceptional point was identified.

In equilibrium, EuO consists of localized moments which undergo a ferromagnetic phase transition at $T_C = 69\mathrm{K}$. Upon excitation by the pump pulse, electrons are promoted into the conduction band and subsequently form excitons. Through spin scattering, these excitons can transition into excited triplet states. Since these triplet excitons do not have an optical signature, they were dubbed as dark excitons, while the optically active ones were labeled as bright excitons. To describe the system, a set of rate equations were developed using the Lindblad formalism. The relevant degrees of freedom were identified as the magnetization and the populations of bright and dark excitons. Due to the temperature dependence of the magnetization and the Lindblad coupling constants, a non-Hermitian phase transition can occur. The theoretical results demonstrate good agreement with the experimental observations, including a kink-like feature in the decay rates at the Curie temperature, giving strong support to the proposed mechanism. The underlying mechanism response for the non-Hermitian phase transition is quite general, and therefore it expected that similar phase transitions could occur in a broader class of materials. While the analysis here was performed within the Lindblad formalism, a more complete quantum field theory treatment would be necessary to capture the full many-body dynamics, and to explain the features which are not captured by the rate-equation approach. The tools in Chapter 4, provide a good starting point for such an extension.

Finally, Chapter 6 shifts the focus once again, this time towards studying photon Bose-Einstein condensation in a dye-filled microcavity. In this system, the dissipative processes enabled the condensation of photons, and a steady condensate was observed experimentally [159]. Until now, most theoretical treatments have not considered the $U(1)$ symmetry breaking as well as fluctuations on equal footing. In this system, the Lindblad formalism has been shown to be well suited to capturing the relevant physics [161]. This chapter investigates the $U(1)$ symmetry breaking terms, captured by the condensate field and the electronic transition rate, as well as fluctuations, given by the photon number and the number of excited molecules, using a systematic second-order cumulant expansion.

The steady-state analysis showed that this system admits only a single stable fixed point where the condensate amplitude vanishes. This contradicts the experimental observations of a steady non-zero condensate and raises concerns, given that this approach has been successfully used previously. Surprisingly, when the time evolution was examined, a long-lived metastable state was found with finite condensate amplitude was found. This state persisted for timescales much longer than the experimentally relevant observation window. The origin of this metastability was traced to the presence of an unphysical fixed point located near the physical boundary of the phase space. This fixed point has a finite condensate amplitude, and although it is not stable in the long-time limit, it acts as an attractor. As a result, the system spends an enormously large amount of time near this point in phase space before eventually reaching the true steady state with no condensate. Such fixed points are well known in nonlinear dynamical systems. Moreover, This stabilization mechanism provides an alternative to prethermalization and may potentially be realized on other dynamical platforms as well.

Appendix A

Numerical Fourier Transforms

The Fast Fourier transform (FFT) algorithm is considered to be one of the most important algorithms ever developed. It was built to compute discrete Fourier transforms, reducing computing costs from $\mathcal{O}(N^2)$ to $\mathcal{O}(N \log N)$, leading to a significant time speed up. Due to this, many researchers nowadays try to utilize FFTs to develop efficient solving methods for complex problems. This appendix describes how FFTs were used to compute Fourier transforms on a special non-equidistant grid.

A.1 Symmetric Grids

The Fourier transformation is defined as

$$F(\omega) = \int_{-\infty}^{\infty} dt\, f(t) e^{i\omega t}\,, \tag{A.1}$$

with the inverse Fourier transform defined as

$$F(t) = \int_{-\infty}^{\infty} \frac{d\omega}{2\pi}\, f(\omega) e^{-i\omega t}\,. \tag{A.2}$$

The forward FFT computes the following discrete sums

$$F_m = \sum_{j=0}^{N-1} f_j\, e^{-i\frac{2\pi}{N}jm}, \tag{A.3}$$

where N is the number of points in the array and is given by a power of 2. The backwards FFT is defined as

$$F_m = \sum_{j=0}^{N-1} f_j\, e^{i\frac{2\pi}{N}jm}. \tag{A.4}$$

Note that the arbitrary choice of directions is reversed in these two definitions. To bring Equation (A.1) and Equation (A.2) into a discrete form it is necessary to massage the expressions. First of all, it is assumed that the function f has finite support within some interval. This allows the variable t to be discretized as follows $t_j = (j - N/2)\,\Delta t$, where $j \in (0, 1, ..., N-1)$, the time grid discretization is $\Delta t = (t_f - t_0)/N$ where t_0 is the initial time and t_f is the final time. The frequency grid needs to be constructed in an equivalent way. Such that $\omega_j = (j - N/2)\,\Delta\omega$ for an initial ω_0 and a final ω_f, the frequency grid discretization is given as $\Delta\omega = (\omega_f - \omega_0)/N$.

One of the most useful ways to discretize the grid is in a symmetric way, where $t_f = -t_0$ and $\omega_f = -\omega_0$. Since the function has finite support, finite boundaries for the integral can be introduced,

$$F(\omega) = \int_{-t_f}^{t_f} dt\, f(t) e^{i\omega t}\,, \tag{A.5}$$

Discretizing and approximating the integral by a Riemann sum gives

$$\begin{aligned} F(\omega_k) &\approx \Delta t \sum_{j=0}^{N-1} f(t_j) e^{i\omega_k t_j} && \text{(A.6)} \\ &= \Delta t \sum_{j=0}^{N-1} f(t_j) e^{i(k-\frac{N}{2})\Delta\omega(j-\frac{N}{2})\Delta t} && \text{(A.7)} \\ &= \Delta t\, e^{i\frac{N^2}{4}\Delta\omega\Delta t} e^{-i\frac{N}{2}\Delta\omega\Delta t\, k} \sum_{j=0}^{N-1} e^{-i\frac{N}{2}j\,\Delta\omega\Delta t} f(t_j) e^{i\Delta\omega\Delta t\, kj}. && \text{(A.8)} \end{aligned}$$

To be able to obtain an expression similar to Equation (A.3), $\Delta\omega\Delta t = \frac{2\pi}{N}$ must be chosen. Since N is a power of 2, the first part is given by $e^{i\frac{N}{2}\pi} = 1$. Therefore,[1]

$$\begin{aligned} F(\omega_k) &\approx \Delta t e^{-i\pi k} \sum_{j=0}^{N-1} e^{-i\pi j} f(t_j) e^{i\frac{2\pi}{N}kj} && \text{(A.9)} \\ &= \Delta t (-1)^k \sum_{j=0}^{N-1} (-1)^j f(t_j) e^{i\frac{2\pi}{N}kj} && \text{(A.10)} \\ &= \Delta t (-1)^k \, \mathrm{BFFT}\left((-1)^j f(t_j)\right). && \text{(A.11)} \end{aligned}$$

Similarly, the inverse Fourier transform is given by

$$F(t) \approx \frac{\Delta\omega}{2\pi} (-1)^k \, \mathrm{FFT}\left((-1)^j f(t_j)\right). \tag{A.12}$$

It can now be easily verified that applying the Fourier transform and then the inverse Fourier transform on an array returns the array.

$$\begin{aligned} &\frac{\Delta\omega}{2\pi} (-1)^m \, \mathrm{FFT}\left((-1)^j \Delta t (-1)^j \, \mathrm{BFFT}\left((-1)^l f(t_l)\right)\right) && \text{(A.13)} \\ &= \frac{\Delta\omega\Delta t}{2\pi} (-1)^m \, \mathrm{FFT}\left(\mathrm{BFFT}\left((-1)^l f(t_l)\right)\right) && \text{(A.14)} \\ &= \frac{\Delta\omega\Delta t}{2\pi} (-1)^m N (-1)^m f(t_m) && \text{(A.15)} \\ &= \underbrace{\frac{N\Delta\omega\Delta t}{2\pi}}_{=1} f(t_m) = f(t_m), && \text{(A.16)} \end{aligned}$$

where $\mathrm{FFT}(\mathrm{BFFT}(x_j)) = N x_m \delta_{m,j}$ was used to obtain the third line. Note that this relation, which seems trivially true, holds because of the definition of the time and frequency grids. Other definitions might not fulfill this relation.

---

[1] Many FFT packages provide a function that directly computes the expression in Equation (A.11). Since the function $f(t_j)$ is assumed to be periodic, the multiplication by $(-1)^j$ constitutes to an index shift, the result can be obtained by shifting the indices, given by $\mathrm{fftshift}(\mathrm{BFFT}\,(f(t_j)) = \mathrm{BFFT}\left((-1)^j f(t_j)\right)$.

A.2 Exponential Grids

The symmetric equidistant grids defined above are quite good for most applications. Sometimes, especially when a large N is required, it can be useful to construct a non-equidistant grid which has many points in important regions and is sparse in non-important ones. In this case, application of the FFT algorithm is not as straightforward as in the previous section. In this section, a specialized grid for which the FFT algorithm can be applied to compute a Fourier transform on a non-equidistant grid with complexity $\mathcal{O}(2N\log N)$ is demonstrated.

A.2.1 Construction

First of all, to motivate the choice of the grid some derivations are in order. Starting with the separation of Equation (A.1) into even and odd parts in both ω and t, giving

$$F(\omega) = F_o(\omega) + iF_e(\omega), \tag{A.17}$$

where

$$F_e(\omega) = \int_0^\infty dt\, f_e(t)\cos(\omega t), \tag{A.18}$$

and

$$F_o(\omega) = \int_0^\infty dt\, f_o(t)\sin(\omega t). \tag{A.19}$$

The subscript stands for the even or odd part of the function respectively, defined by $f_{e/o}(x) = \frac{1}{2}\left(f(x) \pm f(-x)\right)$. Now, $\omega = e^\nu$ and similarly $t = e^\tau$, thus,

$$F(e^\nu) = \int_{-\infty}^\infty d\tau\, e^\tau f_e(e^\tau)\cos\!\left(e^{\nu+\tau}\right) + i\int_{-\infty}^\infty d\tau\, e^\tau f_o(e^\tau)\sin\!\left(e^{\nu+\tau}\right). \tag{A.20}$$

These integrals are cross correlations, which can be solved with Fourier transforms, moreover, ν and τ can be chosen on an equidistant grid, for which FFTs can be applied to. These integrals can be simplified even more

$$\begin{aligned}
F_e(e^\nu) &= \int_{-\infty}^\infty d\tau\, e^\tau f(e^\tau)\cos\!\left(e^{\nu+\tau}\right) && \text{(A.21)}\\
&= e^{-\lambda\nu}\int_{-\infty}^\infty d\tau\, \underbrace{e^{(1-\lambda)\tau} f(e^\tau)}_{\overline{g_e(\tau)}}\, \underbrace{e^{\lambda(\nu+\tau)}\cos\!\left(e^{\nu+\tau}\right)}_{h_e(\tau+\nu)} && \text{(A.22)}\\
&= e^{-\lambda\nu}\int_{-\infty}^\infty \frac{dk}{2\pi}\, e^{-i\nu k}\overline{G_e(k)}H_e(k), && \text{(A.23)}
\end{aligned}$$

where $\overline{h}$ denotes the complex conjugate of h, and a capitalized letter denotes a Fourier transform, $H(k) = \int_{-\infty}^\infty d\tau\, h(\tau)e^{ik\tau}$. Note that, λ was seemingly introduced arbitrarily, however it allows the analytic computation of $H_e(k)$

$$\begin{aligned}
H_e(k) &= \int_{-\infty}^\infty d\tau\, e^{\lambda\tau}\cos(e^\tau)e^{ik\tau} && \text{(A.24)}\\
&= \frac{1}{2}\left(\int_{-\infty}^\infty d\tau\, e^{(\lambda+ik)\tau+ie^\tau} + \int_{-\infty}^\infty d\tau\, e^{(\lambda+ik)\tau-ie^\tau}\right) && \text{(A.25)}\\
&= \frac{1}{2}\left(e^{i\frac{\pi}{2}(\lambda+ik)}\int_{-\infty}^\infty d\tau\, e^{(\lambda+ik)\tau-e^\tau} + e^{-i\frac{\pi}{2}(\lambda+ik)}\int_{-\infty}^\infty d\tau\, e^{(\lambda+ik)\tau-e^\tau}\right) && \text{(A.26)}\\
&= \cos\left(\frac{\pi}{2}(\lambda+ik)\right)\Gamma(\lambda+ik) && \text{(A.27)}
\end{aligned}$$

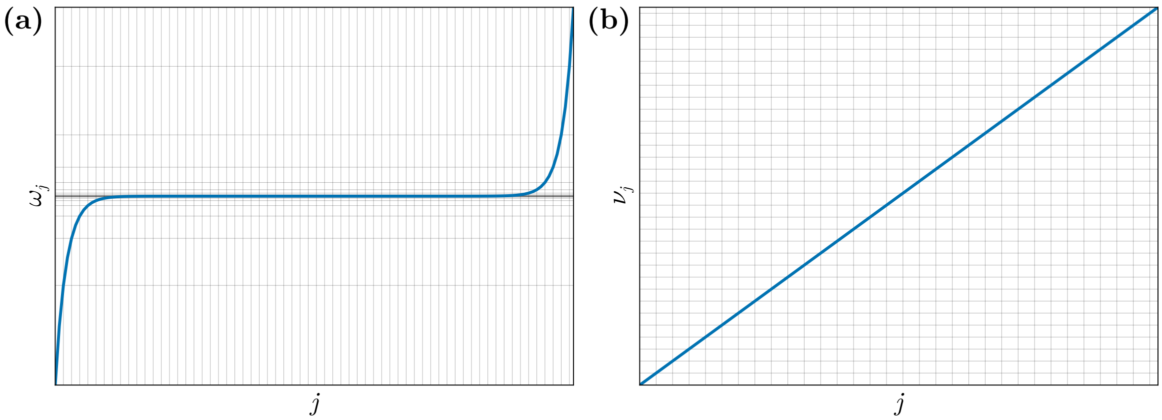

Figure A.1: **(a)** Grid points given by Equation (A.30), concentrated around $\omega_j = 0$. **(b)** The computational grid points, on which the FFT will be performed.

where in the third line, the integration variable was shifted as $\tau \to \tau \pm i\pi/2$. It is clear that had $\lambda = 0$ been chosen, the value at $k = 0$ would not be defined. The odd integral can be treated in an analogous way to obtain

$$H_o(k) = \sin\left(\frac{\pi}{2}(\lambda + ik)\right)\Gamma(\lambda + ik). \tag{A.28}$$

All that is left, is to compute $\overline{G(k)}$ which will be done using an FFT. This is done using the approach developed in the previous section where the computational grid is given by $\tau_j = (j - \frac{N}{2})\Delta\tau$. The negative frequency and time arguments can be simply obtained from the odd and even parts of the function. Meaning that the physical grid on which the function is evaluated is given by

$$t_j = \begin{cases} +e^{\tau_j^p} & \text{for } t_j > 0, \\ -e^{\tau_j^n} & \text{for } t_j < 0. \end{cases} \tag{A.29}$$

where $\tau_j^p = \tau_j^m$ corresponds to the computational grid for the positive and negative values of t_j respectively. The frequency grid is defined in an equivalent way by

$$\omega_j = \begin{cases} +e^{\nu_j^p} & \text{for } \omega_j > 0, \\ -e^{\nu_j^n} & \text{for } \omega_j < 0. \end{cases} \tag{A.30}$$

where $\nu_j^p = \nu_j^m = (j - \frac{N}{2})\Delta\nu$ corresponds to the computational grid for the positive and negative values of ω_j respectively, see Figure A.1.

Appendix B

Periodically Driven Single Impurity

In this appendix, additional plots for the periodically driven single impurity Anderson model are presented. In principle, these do not show any significantly new results since the discussion in Chapter 3 incorporated all the effects of the driving in the lattice model scenario, and the overall behavior of the driven single impurity model follows the same trends as in the driven lattice model. Therefore, the results shown here are only for completeness and thus shown with minimal discussion. The full discussion is presented in Section 3.3.3.

The periodically driven d-electron spectral functions are presented in Figure B.1. Panel **(a)** shows to hybridization driving, while panel **(b)** corresponds to the impurity energy level driving. In both cases, Floquet replicas of the Kondo peak appear, following the Floquet theorem. The insets show the corresponding distribution function, which indicate that the system is in a non-thermal Floquet steady state. The redistribution of spectral weight corresponds to photon absorption and emission processes, which populate high-energy states and depopulate low-energy states. In contrast to the lattice model, there are no heating effects in the driven single impurity model. This is because, within the NCA, the conduction electrons remain unrenormalized and effectively act as a heat bath, which maintains the temperature of the system and prevents heating. It can be seen, the Kondo resonance peak is much more sensitive to the hybridization driving than to the impurity energy level driving.

The middle row of Figure B.1 shows the dependence of the spectral function on the driving frequency Ω. For low Ω, the Kondo peak remains largely unaffected. This is because, in this case the driving acts an adiabatic perturbation, leaving the system unharmed. As Ω increases, the main Kondo peak is gradually suppressed and eventually recovers at large frequencies. The large frequency behavior can be understood as when the frequency is so large the fast oscillations just average out the effect of the drive, essentially removing it's dependence and the original Kondo peak is recovered. The behavior in the intermediate driving regime is associated the an effective increase in the hybridization, described in detail in Section 3.3.3.

The bottom row of Figure B.1 shows the dependence of the spectral function on the driving strength. For weak driving, the driving acts as a small perturbation, meaning that the system is largely unchanged. As Δ increases, sidebands emerge in both cases and the central Kondo peak is suppressed. At strong enough driving, the Kondo effect is destroyed altogether, since at this point the driving is so strong that it completely dominates and washes out the underlying properties of the system. Once again, the impact of the hybridization driving is found to be stronger than that of the energy level driving, as in the lattice case.

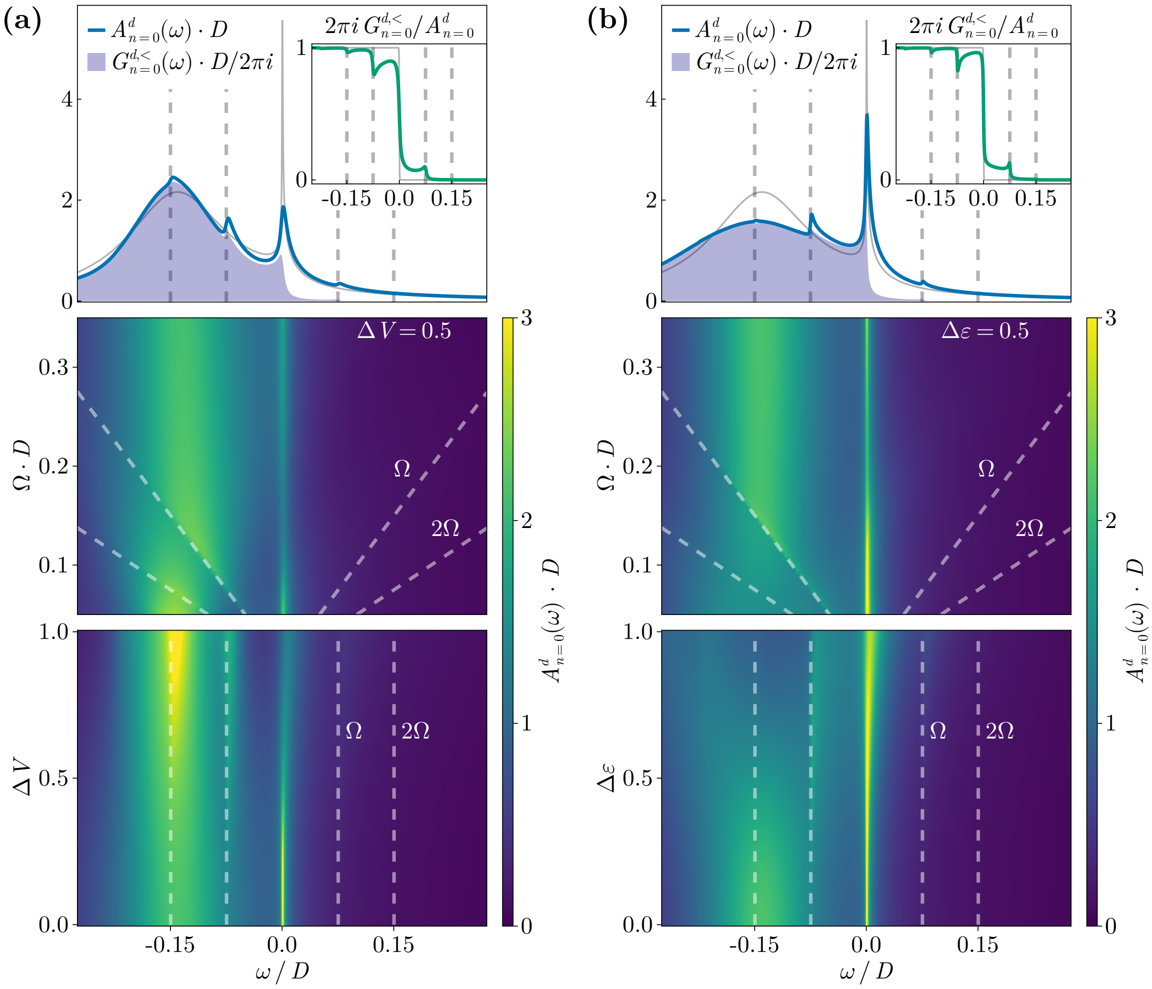

Figure B.1: *d*-electron spectral function for the periodically driven single impurity Anderson model. From top to bottom, the panels show the spectral function at a fixed driving frequency $\Omega = 0.075D$ and a fixed driving strength $\Delta_{V,\varepsilon} = 0.5$, where the inset shows the distribution function. Below that, the panels show the dependence on Ω and then the Δ dependence for **(a)** hybridization drive and **(b)** impurity energy level drive. The dashed line in all panels indicate the driving frequency Ω and twice the driving frequency. The parameters are $\varepsilon_d = -0.15D$, $V = \sqrt{0.0175}D$, $\beta = 3000/D$.

Bibliography

[1] J. Zhang, P. W. Hess, A. Kyprianidis, P. Becker, A. Lee, J. Smith, G. Pagano, I. D. Potirniche, A. C. Potter, A. Vishwanath, N. Y. Yao, and C. Monroe, “Observation of a discrete time crystal”, Nature 2017 543:7644 **543**, 217 (2017).

[2] D. Abanin, W. D. Roeck, W. W. Ho, and F. Huveneers, “A Rigorous Theory of Many-Body Prethermalization for Periodically Driven and Closed Quantum Systems”, Communications in Mathematical Physics **354**, 809 (2017).

[3] B. Liu, M. Först, M. Fechner, D. Nicoletti, J. Porras, T. Loew, B. Keimer, and A. Cavalleri, “Pump Frequency Resonances for Light-Induced Incipient Superconductivity in $YBa_2Cu_3O_{6.5}$”, Physical Review X **10**, 011053 (2020).

[4] Z. Fedorova, H. Qiu, S. Linden, and J. Kroha, “Observation of topological transport quantization by dissipation in fast Thouless pumps”, Nature Communications 2020 11:1 **11**, 1 (2020).

[5] N. Goldman and J. Dalibard, “Periodically driven quantum systems: Effective Hamiltonians and engineered gauge fields”, Physical Review X **4**, 031027 (2014).

[6] W. J. de Haas, J. de Boer, and G. J. van dën Berg, “The electrical resistance of gold, copper and lead at low temperatures”, Physica **1**, 1115 (1934).

[7] P. Thalmeier, G. Zwicknagl, O. Stockert, G. Sparn, and F. Steglich, “Superconductivity in heavy fermion compounds”, in *Frontiers in superconducting materials* (Springer Berlin Heidelberg, Berlin, Heidelberg, 2005).

[8] H. Aoki, N. Tsuji, M. Eckstein, M. Kollar, T. Oka, and P. Werner, “Nonequilibrium dynamical mean-field theory and its applications”, Reviews of Modern Physics **86**, 779 (2014).

[9] J. Li, M. Turaev, M. Matsubara, K. Kliemt, C. Krellner, S. Pal, M. Fiebig, and J. Kroha, “Discovery of a non-Hermitian phase transition in a bulk condensed-matter system”, `https://arxiv.org/abs/2412.16012`, 2024.

[10] A. Abouelela, M. Turaev, R. Kramer, M. Janning, M. Kajan, S. Ray, and J. Kroha, “Stabilizing Open Photon Condensates by Ghost-Attractor Dynamics”, Phys. Rev. Lett. **135**, 053402 (2025).

[11] A. Kamenev, *Field Theory of Non-Equilibrium Systems* (Cambridge University Press, 2011).

[12] G. Stefanucci and R. van Leeuwen, *Nonequilibrium Many-Body Theory of Quantum Systems* (Cambridge University Press, 2013).

[13] L. P. Kadanoff and G. Baym, *Quantum Statistical Mechanics* (CRC Press, 2018).

[14] A. C. Hewson, *The Kondo Problem to Heavy Fermions* (Cambridge University Press, 1993).

[15] L. M. Sieberer, M. Buchhold, and S. Diehl, “Keldysh field theory for driven open quantum systems”, Reports on Progress in Physics **79**, 096001 (2016).

[16] N. Dupuis, *Field Theory of Condensed Matter and Ultracold Gases* (World Scientific (Europe), 2023).

[17] H.-P. Breuer and F. Petruccione, *The theory of open quantum systems* (Oxford university press, 2002).

[18] R. Kubo, “Generalized cumulant expansion method”, Journal of the Physical Society of Japan **17**, 1100 (1962).

[19] L. V. Keldysh, “Diagram Technique for Nonequilibrium Processes”, Soviet Physics JETP **20**, 1018 (1965).

[20] A. I. Larkin and Y. N. Ovchinnikov, “Nonlinear conductivity of superconductors in the mixed state”, Soviet Physics JETP **41**, 960 (1975).

[21] G. Baym and L. P. Kadanoff, “Conservation Laws and Correlation Functions”, Physical Review **124**, 287 (1961).

[22] P. W. Anderson, “More is different”, Science **177**, 393 (1972).

[23] J. G. Bednorz and K. A. Müller, “Possible high Tc superconductivity in the Ba-La-Cu-O system”, Zeitschrift für Physik B Condensed Matter **64**, 189 (1986).

[24] M. K. Wu, J. R. Ashburn, C. J. Torng, P. H. Hor, R. L. Meng, L. Gao, Z. J. Huang, Y. Q. Wang, and C. W. Chu, “Superconductivity at 93 K in a new mixed-phase Yb-Ba-Cu-O compound system at ambient pressure”, Physical Review Letters **58**, 908 (1987).

[25] F. Steglich, J. Aarts, C. D. Bredl, W. Lieke, D. Meschede, W. Franz, and H. Schäfer, “Superconductivity in the presence of strong pauli paramagnetism: $CeCu_2Si_2$”, Physical Review Letters **43**, 1892 (1979).

[26] K. Andres, J. E. Graebner, and H. R. Ott, “$4f$-virtual-bound-state formation in $CeAl_3$ at low temperatures”, Physical Review Letters **35**, 1779 (1975).

[27] Y. Cao, V. Fatemi, S. Fang, K. Watanabe, T. Taniguchi, E. Kaxiras, and P. Jarillo-Herrero, “Unconventional superconductivity in magic-angle graphene superlattices”, Nature **556**, 43 (2018).

[28] R. A. D. Groot, F. M. Mueller, P. G. Engen, and K. H. Buschow, “New class of materials: Half-metallic ferromagnets”, Physical Review Letters **50**, 2024 (1983).

[29] F. D. Haldane, “’Luttinger liquid theory’ of one-dimensional quantum fluids. I. Properties of the Luttinger model and their extension to the general 1D interacting spinless fermi gas”, Journal of physics C: Solid State Physics **14**, 2585 (1981).

[30] D. L. Cox, “Quadrupolar Kondo effect in uranium heavy-electron materials?”, Physical Review Letters **59**, 1240 (1987).

[31] C. Kittel, *Introduction to Solid State Physics*, 8th (John Wiley & Sons, 2005).

[32] W. Meissner and B. Voigt, “Messungen mit Hilfe von flüssigem Helium XI Widerstand der reinen Metalle in tiefen Temperaturen”, Annalen der Physik **399**, 761 (1930).

[33] J. Kondo, “Theory of Dilute Magnetic Alloys”, Solid State Physics - Advances in Research and Applications **23**, 183 (1970).

[34] W. J. D. Haas and G. J. V. D. Berg, “The electrical resistance of gold and silver at low temperatures”, Physica **3**, 440 (1936).

[35] J. Kondo, “Resistance Minimum in Dilute Magnetic Alloys”, Progress of Theoretical Physics **32**, 37 (1964).

[36] J. Kondo, “The Fermi surface effects”, Japanese Journal of Applied Physics **26**, 1777 (1987).

[37] P. W. Anderson, “A poor man’s derivation of scaling laws for the Kondo problem”, Journal of Physics C: Solid State Physics **3**, 2436 (1970).

[38] P. Nozières, “A ”fermi-liquid” description of the Kondo problem at low temperatures”, Journal of Low Temperature Physics **17**, 31 (1974).

[39] K. G. Wilson, “The renormalization group: Critical phenomena and the Kondo problem”, Reviews of Modern Physics **47**, 773 (1975).

[40] P. W. Anderson, “Localized Magnetic States in Metals”, Physical Review **124**, 41 (1961).

[41] J. R. Schrieffer and P. A. Wolff, “Relation between the Anderson and Kondo Hamiltonians”, Physical Review **149**, 491 (1966).

[42] P. Coleman, “New approach to the mixed-valence problem”, Physical Review B **29**, 3035 (1984).

[43] S. E. Barnes, “New method for the Anderson model”, Journal of Physics F: Metal Physics **6**, 1375 (1976).

[44] S. E. Barnes, “New method for the Anderson model. II. The U=0 limit”, Journal of Physics F: Metal Physics **7**, 2637 (1977).

[45] S. Elitzur, “Impossibility of spontaneously breaking local symmetries”, Physical Review D **12**, 3978 (1975).

[46] N. Read and D. M. Newns, “A new functional integral formalism for the degenerate anderson model”, Journal of Physics C: Solid State Physics **16**, L1055 (1983).

[47] P. Coleman, *Introduction to Many-Body Physics* (Cambridge University Press, 2015).

[48] N. S. Wingreen and Y. Meir, “Anderson model out of equilibrium: Noncrossing-approximation approach to transport through a quantum dot”, Physical Review B **49**, 11040 (1994).

[49] J. Kroha and P. Wölfle, “Fermi and non-fermi liquid behavior in quantum impurity systems: Conserving slave boson theory”, in (Springer Berlin Heidelberg, 1998).

[50] M. Lenk, “Dynamical Effects in Heavy-Fermion Systems”, PhD thesis (Rheinische Friedrich-Wilhelms-Universität Bonn, 2025).

[51] T. A. Costi, J. Kroha, and P. Wölfle, “Spectral properties of the Anderson impurity model: Comparison of numerical-renormalization-group and noncrossing-approximation results”, Physical Review B **53**, 1850 (1996).

[52] D. C. Langreth, “Friedel Sum Rule for Anderson’s Model of Localized Impurity States”, Physical Review **150**, 516 (1966).

[53] D. L. Cox and A. Zawadowski, “Exotic Kondo Effects in Metals: Magnetic Ions in a Crystalline Electric Field and Tunneling Centers”, `https://arxiv.org/abs/cond-mat/9704103`, 1997.

[54] A. J. Millis and P. A. Lee, “Large-orbital-degeneracy expansion for the lattice Anderson model”, Physical Review B **35**, 3394 (1987).

[55] X. Y. Zhang, M. J. Rozenberg, and G. Kotliar, “Mott transition in the $d = \infty$ Hubbard model at zero temperature”, Physical Review Letters **70**, 1666 (1993).

[56] M. Jarrell, “Symmetric periodic Anderson model in infinite dimensions”, Physical Review B **51**, 7429 (1995).

[57] V. I. Anisimov, A. I. Poteryaev, M. A. Korotin, A. O. Anokhin, and G. Kotliar, “First-principles calculations of the electronic structure and spectra of strongly correlated systems: Dynamical mean-field theory”, Journal of Physics Condensed Matter **9**, 7359 (1997).

[58] A. Georges, G. Kotliar, W. Krauth, and M. J. Rozenberg, “Dynamical mean-field theory of strongly correlated fermion systems and the limit of infinite dimensions”, Reviews of Modern Physics **68**, 13 (1996).

[59] N. E. Bickers, D. L. Cox, and J. W. Wilkins, “Self-consistent large-N expansion for normal-state properties of dilute magnetic alloys”, Physical Review B **36**, 2036 (1987).

[60] M. S. Rudner and N. H. Lindner, “Band structure engineering and non-equilibrium dynamics in Floquet topological insulators”, Nature Reviews Physics 2020 2:5 **2**, 229 (2020).

[61] T. Oka and S. Kitamura, “Floquet engineering of quantum materials”, Annual Review of Condensed Matter Physics **10**, 387 (2019).

[62] G. Jotzu, M. Messer, R. Desbuquois, M. Lebrat, T. Uehlinger, D. Greif, and T. Esslinger, “Experimental realization of the topological Haldane model with ultracold fermions”, Nature 2014 515:7526 **515**, 237 (2014).

[63] M. S. Rudner, N. H. Lindner, E. Berg, and M. Levin, “Anomalous edge states and the bulk-edge correspondence for periodically driven two-dimensional systems”, Physical Review X **3**, 031005 (2013).

[64] Y. Murakami, M. Eckstein, and P. Werner, “High-Harmonic Generation in Mott Insulators”, Physical Review Letters **121**, 057405 (2018).

[65] D. M. Kennes, M. Claassen, M. A. Sentef, and C. Karrasch, “Light-induced *d*-wave superconductivity through Floquet-engineered Fermi surfaces in cuprates”, Physical Review B **100**, 075115 (2019).

[66] S. Kitamura and H. Aoki, “Floquet topological superconductivity induced by chiral many-body interaction”, Communications Physics **5**, 174 (2022).

[67] F. Peronaci, M. Schiró, and O. Parcollet, “Resonant Thermalization of Periodically Driven Strongly Correlated Electrons”, Physical Review Letters **120**, 197601 (2018).

[68] C. Wetli, S. Pal, J. Kroha, K. Kliemt, C. Krellner, O. Stockert, H. v. Löhneysen, and M. Fiebig, “Time-resolved collapse and revival of the Kondo state near a quantum phase transition”, Nature Phys **14**, 1103 (2018).

[69] H. Chu, M. J. Kim, K. Katsumi, S. Kovalev, R. D. Dawson, L. Schwarz, N. Yoshikawa, G. Kim, D. Putzky, Z. Z. Li, H. Raffy, S. Germanskiy, J. C. Deinert, N. Awari, I. Ilyakov, B. Green, M. Chen, M. Bawatna, G. Cristiani, G. Logvenov, Y. Gallais, A. V. Boris, B. Keimer, A. P. Schnyder, D. Manske, M. Gensch, Z. Wang, R. Shimano, and S. Kaiser, “Phase-resolved Higgs response in superconducting cuprates”, Nature Communications **11**, 1793 (2020).

[70] A. Eckardt, “Colloquium: Atomic quantum gases in periodically driven optical lattices”, Reviews of Modern Physics **89**, 011004 (2017).

[71] N. Tsuji, T. Oka, and H. Aoki, “Correlated electron systems periodically driven out of equilibrium: Floquet+DMFT formalism”, Physical Review B **78**, 235124 (2008).

[72] M. Eckstein and P. Werner, "Nonequilibrium dynamical mean-field calculations based on the noncrossing approximation and its generalizations", Physical Review B **82**, 115115 (2010).

[73] P. Hartman, *Ordinary Differential Equations* (Society for Industrial and Applied Mathematics, 2002).

[74] J. H. Shirley, "Solution of the Schrödinger Equation with a Hamiltonian Periodic in Time", Physical Review **138**, B979 (1965).

[75] M. Grifoni and P. Hänggi, "Driven quantum tunneling", Physics Report **304**, 229 (1998).

[76] F. Bloch, "Über die Quantenmechanik der Elektronen in Kristallgittern", Zeitschrift für Physik **52**, 555 (1929).

[77] G. Floquet, "Sur les équations différentielles linéaires à coefficients périodiques", Annales scientifiques de l'École Normale Supérieure **12**, 47 (1883).

[78] P. Schmidt and H. Monien, "Nonequilibrium dynamical mean-field theory of a strongly correlated system", `https://arxiv.org/abs/cond-mat/0202046`, 2002.

[79] T. Mikami, S. Kitamura, K. Yasuda, N. Tsuji, T. Oka, and H. Aoki, "Brillouin-Wigner theory for high-frequency expansion in periodically driven systems: Application to Floquet topological insulators", Physical Review B **93**, 144307 (2016).

[80] K. Takasan, M. Nakagawa, and N. Kawakami, "Laser-irradiated Kondo insulators: Controlling the Kondo effect and topological phases", Physical Review B **96**, 115120 (2017).

[81] O. Dmytruk and M. Schiró, "Gauge fixing for strongly correlated electrons coupled to quantum light", Physical Review B **103**, 075131 (2021).

[82] J. Li, D. Golez, G. Mazza, A. J. Millis, A. Georges, and M. Eckstein, "Electromagnetic coupling in tight-binding models for strongly correlated light and matter", Physical Review B **101**, 205140 (2020).

[83] B. H. Wu and J. C. Cao, "Noise of quantum dots in the ac Kondo regime: Slave-boson mean-field method and Floquet theorem", Physical Review B **77**, 233307 (2008).

[84] B. H. Wu and J. C. Cao, "Noise of Kondo dot with ac gate: Floquet–Green's function and noncrossing approximation approach", Physical Review B **81**, 085327 (2010).

[85] H. Qiu, "Periodically driven topological non-interacting and interacting quantum lattice systems", PhD thesis (Rheinische Friedrich-Wilhelms-Universität Bonn, 2022).

[86] F. Harper, R. Roy, M. S. Rudner, and S. Sondhi, "Topology and Broken Symmetry in Floquet Systems", Annual Review of Condensed Matter Physics **11**, 345 (2020).

[87] R. Moessner and S. L. Sondhi, "Equilibration and order in quantum Floquet matter", Nature Physics **13**, 424 (2017).

[88] H. Dehghani, T. Oka, and A. Mitra, "Dissipative Floquet topological systems", Physical Review B **90**, 195429 (2014).

[89] F. Meirinhos, M. Kajan, J. Kroha, and T. Bode, "Adaptive numerical solution of Kadanoff-Baym equations", SciPost Physics Core **5**, 030 (2022).

[90] G. R. Stewart, Z. Fisk, and M. S. Wire, "New Ce heavy-fermion system: $CeCu_6$", Physical Review B **30**, 482 (1984).

[91] Y. Onuki and T. Komatsubara, "Heavy fermion state in $CeCu_6$", Journal of Magnetism and Magnetic Materials **63-64**, 281 (1987).

[92] H. v. Löhneysen, T. Pietrus, G. Portisch, H. G. Schlager, A. Schröder, M. Sieck, and T. Trappmann, “Non-Fermi-liquid behavior in a heavy-fermion alloy at a magnetic instability”, Physical Review Letters **72**, 3262 (1994).

[93] S. Mock, C. Paschke, A. Schröder, J. Sereni, M. Sieck, and H. v. Löhneysen, “Magnetic and thermodynamic properties $\mathrm{CeCu}_{6-x}\mathrm{Au}_x$ for $0 \le x \le 2$”, Physica B **199-200**, 39 (1994).

[94] A. Rosch, “Interplay of disorder and spin fluctuations in the resistivity near a quantum critical point”, Physical Review Letters **82**, 4280 (1999).

[95] P. Coleman, C. Pépin, Q. Si, and R. Ramazashvili, “How do Fermi liquids get heavy and die?”, Journal of Physics: Condensed Matter **13**, R723 (2001).

[96] H. v. Löhneysen, A. Rosch, M. Vojta, and P. Wölfle, “Fermi-liquid instabilities at magnetic quantum phase transitions”, Reviews of Modern Physics **79**, 1015 (2007).

[97] T. Moriya and T. Takimoto, “Anomalous Properties around Magnetic Instability in Heavy Electron Systems”, Journal of the Physical Society of Japan **64**, 960 (1995).

[98] O. Stockert and F. Steglich, “Unconventional Quantum Criticality in Heavy-Fermion Compounds”, Annual Review of Condensed Matter Physics **2**, 79 (2011).

[99] S. Paschen, S. Friedemann, S. Wirth, F. Steglich, S. Kirchner, and Q. Si, “Kondo destruction in heavy fermion quantum criticality and the photoemission spectrum of $\mathrm{YbRh_2Si_2}$”, Journal of Magnetism and Magnetic Materials **400**, 17 (2016).

[100] J. Li, D. Priyadarshi, C.-J. Yang, U. Pohl, O. Stockert, H. von Löhneysen, S. Pal, M. Fiebig, and J. Kroha, “Missing spectral weight in a heavy-fermion system far above the Néel temperature”, Physical Review B **111**, 035117 (2025).

[101] U. Pohl, J. Kroha, et al., “Heavy Fermion Systems with RKKY-Induced Phase Transitions”, In preparation, 2025.

[102] F. C. Meirinhos, “Kondo Collapse and Revival by Pulsed Light”, PhD thesis (Rheinische Friedrich-Wilhelms-Universität Bonn, 2024).

[103] F. Meirinhos, M. Turaev, M. Kajan, T. Bode, and J. Kroha, “Kondo echo dynamics of terahertz-pumped heavy fermions”, `https://arxiv.org/abs/2509.07117`, 2025.

[104] M. G. Benedict, A. M. Ermolaev, V. A. Malyshev, I. V. Sokolov, and E. D. Trifonov, *Super-radiance: multiatomic coherent emission* (CRC Press LLC, 2018).

[105] C.-J. Yang, K. Kliemt, C. Krellner, J. Kroha, M. Fiebig, and S. Pal, “Critical slowing down near a magnetic quantum phase transition with fermionic breakdown”, Nature Physics **19**, 1605 (2023).

[106] E. Beaurepaire, J. C. Merle, A. Daunois, and J. Y. Bigot, “Ultrafast Spin Dynamics in Ferromagnetic Nickel”, Physical Review Letters **76**, 4250 (1996).

[107] A. Kiss, L. Szolnoki, and F. Simon, “The Elliott-Yafet theory of spin relaxation generalized for large spin-orbit coupling”, Scientific Reports **6**, 22706 (2016).

[108] B. Koopmans, G. Malinowski, F. D. Longa, D. Steiauf, M. Fähnle, T. Roth, M. Cinchetti, and M. Aeschlimann, “Explaining the paradoxical diversity of ultrafast laser-induced demagnetization”, Nature Materials **9**, 259 (2010).

[109] G. P. Zhang and W. Hübner, “Laser-induced ultrafast demagnetization in ferromagnetic metals”, Physical Review Letters **85**, 3025 (2000).

[110] P. Maldonado, K. Carva, M. Flammer, and P. M. Oppeneer, “Theory of out-of-equilibrium ultrafast relaxation dynamics in metals”, Physical Review B **96**, 174439 (2017).

[111] J. Hohlfeld, E. Matthias, R. Knorren, and K. H. Bennemann, “Nonequilibrium Magnetization Dynamics of Nickel”, Physical Review Letters **78**, 4861 (1997).

[112] A. Melnikov, H. Prima-Garcia, M. Lisowski, T. Gießel, R. Weber, R. Schmidt, C. Gahl, N. M. Bulgakova, U. Bovensiepen, and M. Weinelt, “Nonequilibrium Magnetization Dynamics of Gadolinium Studied by Magnetic Linear Dichroism in Time-Resolved $4f$ Core-Level Photoemission”, Physical Review Letters **100**, 107202 (2008).

[113] X. Chen, R. Adam, D. E. Bürgler, F. Wang, Z. Lu, L. Pan, S. Heidtfeld, C. Greb, M. Liu, Q. Liu, J. Wang, C. M. Schneider, and D. Cao, “Ultrafast demagnetization in ferromagnetic materials: Origins and progress”, Physics Reports **1102**, 1 (2025).

[114] M. Matsubara, A. Schroer, A. Schmehl, A. Melville, C. Becher, M. Trujillo-Martinez, D. G. Schlom, J. Mannhart, J. Kroha, and M. Fiebig, “Ultrafast optical tuning of ferromagnetism via the carrier density”, Nature Communications **6**, 6724 (2015).

[115] W. D. Heiss, “The physics of exceptional points”, Journal of Physics A: Mathematical and Theoretical **45**, 444016 (2012).

[116] D. J. Luitz and F. Piazza, “Exceptional points and the topology of quantum many-body spectra”, Physical Review Research **1**, 033051 (2019).

[117] C. M. Bender and S. Boettcher, “Real spectra in non-hermitian hamiltonians having PT symmetry”, Physical Review Letters **80**, 5243 (1998).

[118] C. M. Bender, S. Boettcher, and P. N. Meisinger, “PT-symmetric quantum mechanics”, Journal of Mathematical Physics **40**, 2201 (1999).

[119] T. Kato, *Perturbation Theory for Linear Operators*, Vol. 132 (Springer Berlin Heidelberg, 1995).

[120] S. H. Strogatz, *Nonlinear Dynamics and Chaos* (CRC Press, 2018).

[121] Y. Wu, W. Liu, J. Geng, X. Song, X. Ye, C. K. Duan, X. Rong, and J. Du, “Observation of parity-time symmetry breaking in a single-spin system”, Science **364**, 878 (2019).

[122] A. Li, H. Wei, M. Cotrufo, W. Chen, S. Mann, X. Ni, B. Xu, J. Chen, J. Wang, S. Fan, C. W. Qiu, A. Alù, and L. Chen, “Exceptional points and non-Hermitian photonics at the nanoscale”, Nature Nanotechnology **18**, 706 (2023).

[123] L. Pan, S. Chen, and X. Cui, “High-order exceptional points in ultracold Bose gases”, Physical Review A **99**, 011601 (2019).

[124] A. Scholl, L. Baumgarten, R. Jacquemin, and W. Eberhardt, “Ultrafast Spin Dynamics of Ferromagnetic Thin Films Observed by fs Spin-Resolved Two-Photon Photoemission”, Physical Review Letters **79**, 5146 (1997).

[125] M. Matsubara, “Ultrafast Optical Control of Magnetic Interactions in Carrier-Density-Controlled Ferromagnetic Semiconductors”, Applied Sciences **9**, 948 (2019).

[126] B. T. Matthias, R. M. Bozorth, and J. H. V. Vleck, “Ferromagnetic Interaction in EuO”, Physical Review Letters **7**, 160 (1961).

[127] M. R. Oliver, J. A. Kafalas, J. O. Dimmock, and T. B. Reed, “Pressure dependence of the electrical resistivity of EuO”, Physical Review Letters **24**, 1064 (1970).

[128] H. Ott, S. J. Heise, R. Sutarto, Z. Hu, C. F. Chang, H. H. Hsieh, H. J. Lin, C. T. Chen, and L. H. Tjeng, “Soft x-ray magnetic circular dichroism study on Gd-doped EuO thin films”, Physical Review B **73**, 094407 (2006).

[129] A. Schmehl, V. Vaithyanathan, A. Herrnberger, S. Thiel, C. Richter, M. Liberati, T. Heeg, M. Röckerath, L. F. Kourkoutis, S. Mühlbauer, P. Böni, D. A. Muller, Y. Barash, J. Schubert, Y. Idzerda, J. Mannhart, and D. G. Schlom, "Epitaxial integration of the highly spin-polarized ferromagnetic semiconductor EuO with silicon and GaN", Nature Materials **6**, 882 (2007).

[130] T. Stollenwerk and J. Kroha, "Theory of Curie temperature enhancement in electron-doped EuO", Physical Review B **92**, 205119 (2015).

[131] A. Mauger and C. Godart, "The magnetic, optical, and transport properties of representatives of a class of magnetic semiconductors: The europium chalcogenides", Physics Reports **141**, 51 (1986).

[132] Y. Shapira, S. Foner, and T. B. Reed, "EuO. I. Resistivity and Hall Effect in Fields up to 150 kOe", Physical Review B **8**, 2299 (1973).

[133] T. Penney, M. W. Shafer, and J. B. Torrance, "Insulator-Metal Transition and Long-Range Magnetic Order in EuO", Physical Review B **5**, 3669 (1972).

[134] T. Kasuya, "s f exchange interactions and magnetic semiconductors", C R C Critical Reviews in Solid State Sciences **3**, 131 (1972).

[135] P. G. Steeneken, L. H. Tjeng, I. Elfimov, G. A. Sawatzky, G. Ghiringhelli, N. B. Brookes, and D.-J. Huang, "Exchange Splitting and Charge Carrier Spin Polarization in EuO", Physical Review Letters **88**, 047201 (2002).

[136] M. R. Oliver, J. O. Dimmock, A. L. McWhorter, and T. B. Reed, "Conductivity studies in europium oxide", Physical Review B **5**, 1078 (1972).

[137] K. Y. Ahn and M. W. Shafer, "Relationship between stoichiometry and properties of EuO films", Journal of Applied Physics **41**, 1260 (1970).

[138] T. Mairoser, A. Schmehl, A. Melville, T. Heeg, L. Canella, P. Böni, W. Zander, J. Schubert, D. E. Shai, E. J. Monkman, K. M. Shen, D. G. Schlom, and J. Mannhart, "Is there an intrinsic limit to the charge-carrier-induced increase of the curie temperature of EuO?", Physical Review Letters **105**, 257206 (2010).

[139] M. Arnold and J. Kroha, "Simultaneous ferromagnetic metal-semiconductor transition in electron-doped EuO", Physical Review Letters **100**, 046404 (2008).

[140] M. Arnold, "Ferromagnetic Semiconductor-Metal Transition in Europium Monoxide", PhD thesis (Rheinische Friedrich-Wilhelms-Universität Bonn, 2007).

[141] M. Fiebig, N. P. Duong, T. Satoh, B. B. Van Aken, K. Miyano, Y. Tomioka, and Y. Tokura, "Ultrafast magnetization dynamics of antiferromagnetic compounds", Journal of Physics D: Applied Physics **41**, 164005 (2008).

[142] R. W. Boyd, *Nonlinear Optics* (Elsevier, 2020).

[143] I. Mandal and E. J. Bergholtz, "Symmetry and Higher-Order Exceptional Points", Physical Review Letters **127**, 186601 (2021).

[144] H. Hodaei, A. U. Hassan, S. Wittek, H. Garcia-Gracia, R. El-Ganainy, D. N. Christodoulides, and M. Khajavikhan, "Enhanced sensitivity at higher-order exceptional points", Nature **548**, 187 (2017).

[145] F. Sun, Q. Wu, Y. L. Wu, H. Zhao, C. J. Yi, Y. C. Tian, H. W. Liu, Y. G. Shi, H. Ding, X. Dai, P. Richard, and J. Zhao, "Coherent helix vacancy phonon and its ultrafast dynamics waning in topological Dirac semimetal Cd_3As_2", Physical Review B **95**, 235108 (2017).

[146] D. B. But, M. Mittendorff, C. Consejo, F. Teppe, N. N. Mikhailov, S. A. Dvoretskii, C. Faugeras, S. Winnerl, M. Helm, W. Knap, M. Potemski, and M. Orlita, "Suppressed Auger scattering and tunable light emission of Landau-quantized massless Kane electrons", Nature Photonics **13**, 783 (2019).

[147] M. Mittendorff, F. Wendler, E. Malic, A. Knorr, M. Orlita, M. Potemski, C. Berger, W. A. D. Heer, H. Schneider, M. Helm, and S. Winnerl, "Carrier dynamics in Landau-quantized graphene featuring strong Auger scattering", Nature Physics **11**, 75 (2015).

[148] V. Goian, R. Held, E. Bousquet, Y. Yuan, A. Melville, H. Zhou, V. Gopalan, P. Ghosez, N. A. Spaldin, D. G. Schlom, and S. Kamba, "Making EuO multiferroic by epitaxial strain engineering", Communications Materials **1**, 74 (2020).

[149] J. Li, "Optical signatures of phase transitions in quantum materials", PhD thesis (ETH Zurich, 2024).

[150] T. Mitani and T. Koda, "Wannier excitons in the ferromagnetic semiconductors EuO and EuS", Physical Review B **12**, 2311 (1975).

[151] A. Mauger, "Indirect exchange in europium chalcogenides", Physica Status Solidi (b) **84**, 761 (1977).

[152] C. P. Zelle, R. Daviet, A. Rosch, and S. Diehl, "Universal Phenomenology at Critical Exceptional Points of Nonequilibrium O(N) Models", Physical Review X **14**, 021052 (2024).

[153] M. H. Anderson, J. R. Ensher, M. R. Matthews, C. E. Wieman, and E. A. Cornell, "Observation of Bose-Einstein Condensation in a Dilute Atomic Vapor", Science **269**, 198 (1995).

[154] K. B. Davis, M. O. Mewes, M. R. Andrews, N. J. V. Druten, D. S. Durfee, D. M. Kurn, and W. Ketterle, "Bose-Einstein condensation in a gas of sodium atoms", Physical Review Letters **75**, 3969 (1995).

[155] R. Balili, V. Hartwell, D. Snoke, L. Pfeiffer, and K. West, "Bose-Einstein condensation of microcavity polaritons in a trap", Science **316**, 1007 (2007).

[156] L. V. Butov, "Condensation and pattern formation in cold exciton gases in coupled quantum wells", Journal of Physics: Condensed Matter **16**, R1577 (2004).

[157] S. O. Demokritov, V. E. Demidov, O. Dzyapko, G. A. Melkov, A. A. Serga, B. Hillebrands, and A. N. Slavin, "Bose-Einstein condensation of quasi-equilibrium magnons at room temperature under pumping", Nature **443**, 430 (2006).

[158] R. Hanai, A. Edelman, Y. Ohashi, and P. B. Littlewood, "Non-Hermitian Phase Transition from a Polariton Bose-Einstein Condensate to a Photon Laser", Physical Review Letters **122**, 185301 (2019).

[159] J. Klaers, J. Schmitt, F. Vewinger, and M. Weitz, "Bose-Einstein condensation of photons in an optical microcavity", Nature **468**, 545 (2010).

[160] F. E. Öztürk, T. Lappe, G. Hellmann, J. Schmitt, J. Klaers, F. Vewinger, J. Kroha, and M. Weitz, "Observation of a non-hermitian phase transition in an optical quantum gas", Science **372**, 6537 (2021).

[161] P. Kirton and J. Keeling, "Nonequilibrium Model of Photon Condensation", Physical Review Letters **111**, 100404 (2013).

[162] M. Radonjić, W. Kopylov, A. Balaž, and A. Pelster, "Interplay of coherent and dissipative dynamics in condensates of light", New Journal of Physics **20**, 055014 (2018).

[163] T. Lappe, “Non-Markovian Dynamics of Open Bose-Einstein Condensates”, PhD thesis (Rheinische Friedrich-Wilhelms-Universität Bonn, 2021).

[164] P. Kirton and J. Keeling, “Thermalization and breakdown of thermalization in photon condensates”, Physical Review A **91**, 033826 (2015).

[165] A. Loirette-Pelous and J. J. Greffet, “Photon Bose–Einstein Condensation and Lasing in Semiconductor Cavities”, Laser and Photonics Reviews **17**, 2300366 (2023).

[166] M. Pieczarka, M. Gębski, A. N. Piasecka, J. A. Lott, A. Pelster, M. Wasiak, and T. Czyszanowski, “Bose–Einstein condensation of photons in a vertical-cavity surface-emitting laser”, Nature Photonics **18**, 1090 (2024).

[167] J. Marelic, L. F. Zajiczek, H. J. Hesten, K. H. Leung, E. Y. X. Ong, F. Mintert, and R. A. Nyman, “Spatiotemporal coherence of non-equilibrium multimode photon condensates”, New Journal of Physics **18**, 103012 (2016).

[168] J. Schmitt, T. Damm, D. Dung, C. Wahl, F. Vewinger, J. Klaers, and M. Weitz, “Spontaneous Symmetry Breaking and Phase Coherence of a Photon Bose-Einstein Condensate Coupled to a Reservoir”, Physical Review Letters **116**, 033604 (2016).

[169] J. Schmitt, T. Damm, D. Dung, F. Vewinger, J. Klaers, and M. Weitz, “Thermalization kinetics of light: From laser dynamics to equilibrium condensation of photons”, Physical Review A **92**, 011602 (2015).

[170] A. J. Moilanen, K. B. Arnardóttir, J. Keeling, and P. Törmä, “Mode switching dynamics in organic polariton lasing”, Physical Review B **106**, 195403 (2022).

[171] H. Deng, H. Haug, and Y. Yamamoto, “Exciton-polariton Bose-Einstein condensation”, Reviews of Modern Physics **82**, 1489 (2010).

[172] T. Bode, M. Kajan, F. Meirinhos, and J. Kroha, “Non-Markovian dynamics of open quantum systems via auxiliary particles with exact operator constraint”, Physical Review Research **6**, 013220 (2024).